8-2012

On Compressible Gaseous Motions in Swirl Dominated Combustors

Brian A. Maicke
bmaicke@utk.edu

To the Graduate Council:

I am submitting herewith a dissertation written by Brian A. Maicke entitled "On Compressible Gaseous Motions in Swirl Dominated Combustors." I have examined the final electronic copy of this dissertation for form and content and recommend that it be accepted in partial fulfillment of the requirements for the degree of Doctor of Philosophy, with a major in Aerospace Engineering.

Joseph Majdalani, Major Professor

We have read this dissertation and recommend its acceptance:

Trevor Moeller, Christian Parigger, Kenneth Kimble

Accepted for the Council:
Dixie L. Thompson

Vice Provost and Dean of the Graduate School

(Original signatures are on file with official student records.)

On Compressible Gaseous Motions in Swirl Dominated Combustors

A Dissertation

Presented for the

Doctor of Philosophy

Degree

The University of Tennessee, Knoxville

Brian A. Maicke

August 2012

This work is dedicated to my wife, Tiffany, and my parents, Robert and Linda.

Without your love and support, I would not be where I am today.

Acknowledgements

I would like to thank my advisor, Dr. Majdalani, for his support throughout my graduate career at UTSI. I have had the good fortune to work on a number of different projects, spanning a wide range of topics. It is largely through the opportunities I have had while working under Dr. Majdalani that I feel truly prepared to continue my work in academia.

I also wish to thank my committee members for taking the time to shepherd me through the dissertation process. Dr. Kimble, Dr. Moeller, and Dr. Parigger have all provided their expertise and guidance to help make this project a reality.

During my time at UTSI I have been lucky to work with an outstanding group of researchers. The graduate researchers in our group have been top-notch and this work is better for their discussions and suggestions. Specifically I would like to thank Tony Saad and Tim Barber for their discussions both on fluid mechanics and vortex flows. Discussions with Josh Batterson and Michel Akiki have provided a road-map for future work in the numerical analysis of the compressible vortex. I would also like to thank all of the students, faculty, and staff at UTSI for making this campus such a pleasant and intellectually-challenging place to work.

I am particularly grateful to my wife, Tiffany, and my parents, Robert and Linda. My parents instilled in me a life-long love of learning that started me on the path that lead me to the doctoral program at UTSI. Without the patience and support of my wife, I may not have ever returned to school to pursue my doctorate and my dream of teaching engineering at the university level.

Finally, I wish to acknowledge the support I have received while at the University of Tennessee Space Institute. The graduate research assistant funding provided by the university allowed me to begin my studies earlier than I thought possible. I would also like to thank the Air Force Office of Scientific Research, the National Science Foundation, and the Lloyd W. Crawford fellowship program that has provided support for me at various times during my graduate career. Without these sources of funding, I would not have been able to devote the time and energy needed to bring this work to fruition.

It is not the critic who counts; not the man who points out how the strong man stumbles, or where the doer of deeds could have done them better. The credit belongs to the man who is actually in the arena, whose face is marred by dust and sweat and blood; who strives valiantly; who errs, who comes short again and again, because there is no effort without error and shortcoming; but who does actually strive to do the deeds; who knows great enthusiasms, the great devotions; who spends himself in a worthy cause; who at best knows in the end the triumph of high achievement, and who at worst, if he fails, at least fails while daring greatly, so that his place shall never be with those cold and timid souls who neither know victory nor defeat.

Theodore Roosevelt

Abstract

In this dissertation, a number of models are derived to describe swirling flows. Both generalized compressible Bragg-Hawthorne and vorticity-stream function frameworks are determined and left in a generic form suitable for describing a number of different scenarios. These systems are solved for the bidirectional vortex flowfield by means of a Rayleigh-Janzen perturbation, which expands the governing equations in terms of the Mach number squared. The resulting equations are solved to provide a semi-analytical solution after the evaluation of a handful of numerical integrals. These solutions further the understanding of compressible flow in swirl-combustors, as previous compressible studies are primarily experimental or numerical in nature. Additionally, an alternative swirl velocity model is discussed which uses the balancing of pressure and shear forces to arrive at a piecewise velocity model. The model is compared to experimental data using a method that enables the adjustment of laminar models to account for the effects of turbulence. A modified least-squares approach is developed to handle the movable boundary in the piecewise velocity formulation.

Contents

List of Tables

List of Figures

Nomenclature

Roman

A	Area
a	Chamber radius
b	Open radius
c_0	Speed of sound at the reference location
D^2	Combined derivative operator
f	Separation function in r
g	Separation function in z
H	Stagnation enthalpy
h	Unstable stratification height
$\mathcal{I}$	Integral function
L	Aspect ratio, L_0/a
L_0	Chamber length
M	Mach number
O	Landau order symbol

p	Pressure
r	Radial coordinate
Re	Reynolds number
S	Suction strength
T	Temperature
t	Time
U	Tangential reference velocity
u	Radial velocity
$\boldsymbol{U}$	Velocity vector
U_w	Wall injection velocity
V	Vortex Reynolds number, $\frac{\rho U A_i}{\mu L}$
v	Tangential velocity
$v_{\max}$	Peak tangential velocity
w	Axial velocity
X	Matching point for the constant shear stress model
z	Axial coordinate

Subscripts

0	Reference condition
∞	Far-field condition
i	Inlet condition

θ	Tangential spatial direction
o	Outlet condition
r	Radial spatial direction
z	Axial spatial direction

Superscripts

$'$	Ordinary differentiation
$\bar{}$	Dimensional variable
$\hat{}$	Unit vector
^{i}	Inner solution

Symbols

∇	Gradient operator
α	Cyclone half-angle
β	Open radius fraction, b/a
δ_c	Core distance
ϵ	Viscous parameter, $1/Re$
Φ	Parameter in Bloor-Ingham model, $\tan(\phi/2)$
Γ	Circulation
γ	Ratio of specific heats
κ	Off-swirl parameter
ν	Kinematic viscosity

ρ	Density
σ	Dimensionless swirl parameter
τ	Shear stress
θ	Tangential coordinate
$\mathbf{\Omega}$	Vorticity
ψ	Stream function

Abbreviations

CBH	Compressible Bragg-Hawthorne
CFD	Computational Fluid Dynamics
CL	Complex-lamellar
CSS	Constant Shear Stress
CVS	Compressible vorticity-stream function
GSFC	Goddard Space Flight Center
LDV	Laser Doppler velocimetry
NASA	National Aeronautics and Space Administration
NOAA	National Oceanic and Atmospheric Administration
NO_x	Nitrogen Oxides
PDE	Partial differential equation
PIV	Particle Image Velocimetry
SRM	Solid rocket motor
VCCWC	Vortex Combustion Cold-Wall Chamber

Chapter 1

Introduction

Fluid mechanics has a rich tradition of theoretical analysis. Leonardo da Vinci, in addition to being an excellent experimentalist, also derived a one-dimensional, steady form of the conservation of mass equation. Newton's laws of motion form the basis of modern fluid mechanics; his law of viscosity provides us with the moniker of Newtonian for fluids behaving with a linear viscosity. Euler continued the tradition with developments in both differential and integral forms of the equations of motion, but perhaps his largest contribution was in codifying the notation that became the standard in theoretical fluid mechanics.

These theoretical advancements did not exist in a vacuum. Indeed, many of the early researchers in fluid mechanics were also accomplished experimentalists. From Archimedes' apocryphal ''Eureka!'' moment, explaining the principle of buoyancy and the grand engineering marvel of Roman aqueducts, to the Wright brothers experiment in heavier-than-air flight, experiment and theory have gone hand in hand to further our understanding of fluids in the world around us.

Today, computational fluid mechanics have advanced to the point where it is a viable addition to the researcher's arsenal, rounding out the triumvirate of tools available to engineers. This has been accomplished both through improvements in algorithms and in available computing power. Codes that would have taken months to

run only a few years ago can now be run on more inexpensive hardware in a fraction of the time. Many of the advancements in this field are aimed at increasing the accuracy and effective range of solutions, with the goal of reducing development costs for new products through the reduction, or even elimination, of experiment.

In an ideal world, there would be a balance between these three tools. Theoretical advancements would lead to new experiments and computations. A startling experimental or computational result would entice theoreticians to try to formulate a theory to explain such unexpected behavior. All three areas, synergistically growing and aiding each other.

Unfortunately, this is not the case for current fluid mechanics research. Increasingly, funding for theoretical work has been dwindling in recent years. Opportunities for grants in many areas are now focused on computational efforts, with some supplementing experimental research. In many cases, theoretical work is neglected altogether.

The foremost reason for this decline is that the low-hanging fruit has been picked from the tree. Many of the fundamental problems already have a sound theoretical footing. Even more advanced problems, hypersonic aerodynamics for example, have a library of theory to accompany experiment.

Secondly, the reduction in funding for theoretical research has led to fewer researchers with the requisite tools to make contributions in what is admittedly a challenging field. Not only is an understanding of fluid dynamics required, but often advanced mathematical techniques are required to find solutions to modern problems. The result is that many current theoretical studies are conducted by applied mathematicians. This can cause a number of problems for engineers, as applied mathematicians are often more concerned with the mathematical intricacies rather than the solution itself. Additionally, articles in mathematical journals are often not as accessible to engineers as differences in technical jargon and notation can often raise the barrier to understanding.

The intent of this dissertation is to make some small effort at evening the advancements of theoretical fluid mechanics with those of numerical and experimental results, specifically in the area of confined vortex dynamics.

1.1 Compressible Methods

Compressible flow analysis bridges the gap between aerodynamics and internal ballistics. In aerodynamic flows, accurate prediction of velocities in the subsonic regime are critical in predicting the performance of an airfoil. For internal flows, stability analysis often uses an incompressible mean flow as the foundation of the analysis. Incorporating compressibility effects into such research can provide new insights into stability modeling along with more accurate results. Compressible analysis also benefits CFD algorithm development directly as increasingly elaborate frameworks allow developers to validate their codes with models incorporating similar underlying assumptions, rather than relying on out of date equations that may neglect key parameters. These analytical studies are also valuable in their own right, as they advance the state of the art knowledge in fluid mechanics and provide insight into practical applications of compressible flow.

1.1.1 One-Dimensional Models

Some of the first classical compressible studies are one-dimensional in nature. By reducing the complexity in this manner, analytical closure to the flow field becomes more manageable. One of the first works of this type is from Taylor (1910), in which he solves an integral for a closed form solution for adiabatic flow. Later, von Mises (1950) extends the solution to include heat conduction.

A number of popular compressible flow models fall under the category of one-dimensional analysis. Rayleigh and Fanno flows for one-dimensional channel motions are among the first subjects taught to students of compressible fluid mechanics

(Liepmann and Roshko, 2001). These models are often accurate for simple channel flows, but for propulsive applications a more elaborate analysis is often required. In the case of solid rocket motors, a one-dimensional analysis does not adequately capture the injection process occurring at the wall. In liquid motors, two and three-dimensional structures often play important roles in mixing and film cooling. For more advanced motor concepts, such as swirl combustors, the multi-dimensionality is a feature of the motor design and cannot be treated one-dimensionally.

1.1.2 Multi-Dimensional Techniques

One accepted approach in multi-dimensional flow fields is the small-perturbation theory. Often associated with aerodynamics, this technique assumes that the changes introduced by a slender body are relatively minor. The equations of interest are perturbed using the small correction to the flow field as a perturbation parameter. The archetypal example is still Ackeret's flow over a wavy wall. While this is ideal for slender bodies, it is not well-suited for the bidirectional vortex engine as there are no small-disturbances, either in the flow or in the geometry, to exploit for linearization.

Along the same lines as small-perturbation theory, the Prandtl-Glauert expansion method uses variances in the geometry as a perturbation parameter (Shapiro, 1953). The segregated equations are then solved with traditional techniques to find the overall solution. Kaplan (1943, 1944, 1946) successfully applies the procedure to a number of external flows. For internal flows, Balakrishnan et al. (1991, 1992) utilize Prandtl-Glauert in the context of rectangular and cylindrical solid rocket motors. The method is ideal for the long, slender motor configurations considered in these studies, as the aspect ratio makes a convenient perturbation parameter. The framework in Balakrishnan et al. (1991, 1992) must be solved numerically, which limits the viability in seeking an analytical closure, as the vortical equivalent would also likely resort to numerics. Additionally, the length of a typical bidirectional vortex engine is not

sufficient to produce the requisite perturbation parameter. The combination of these factors renders the Prandtl-Glauert method unsuitable for the present study.

In the hodograph method, a transform of the variables is introduced so that the velocities behave as independent variables rather than the geometric coordinates. This modification linearizes the stream function with respect to the velocities which facilitates analytical closure. Tsien (1939) and von Kármán (1941) use the hodograph plane to solve a number of external compressible flow problems. The popularity of the technique has fallen since its height in the 40's and 50's, especially with the advent of computational fluid mechanics, though it still has some proponents in airfoil design (Cohen, 1984).

The transformation and solution in the hodograph plane can be a difficult proposition. Even with the transformed solution in hand, reverting back to the laboratory coordinates is even more challenging than the initial transformation. For the internal flow in a swirl combustor, the combination of transformation issues as well as adapting what is primarily a technique for external flows, reduces the attractiveness of the hodograph technique for the present study.

The final method under consideration is the Rayleigh-Janzen perturbation method. The procedure was developed independently by Janzen (1913) and Rayleigh (1916) to solve subsonic compressible flows. Using an expansion in the Mach number squared, the perturbed relations may be segregated into equations of the same order and then solved sequentially to produce a compressible model. The leading order recovers the incompressible solution, while subsequent higher-order terms capture the compressible corrections.

The original study by Rayleigh (1916) examined the potential flow around a right-circular cylinder. Also in the external flow category, Heaslet (1944) solves the compressible motion about a cylinder with circulation. Barsony-Nagy et al. (1987) uses the Rayleigh-Janzen expansion to study plane, steady flows containing potential point vortices interacting with obstacles. In extending the method to rotational flows, the studies by Moore and Pullin (1991, 1998) and Meiron et al. (2000) showcase the

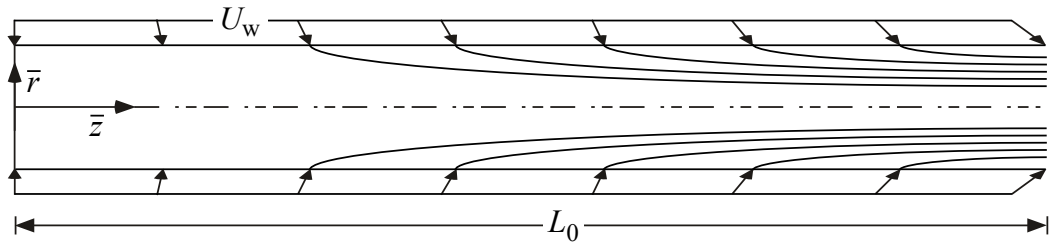

(a) Hart-McClure profile

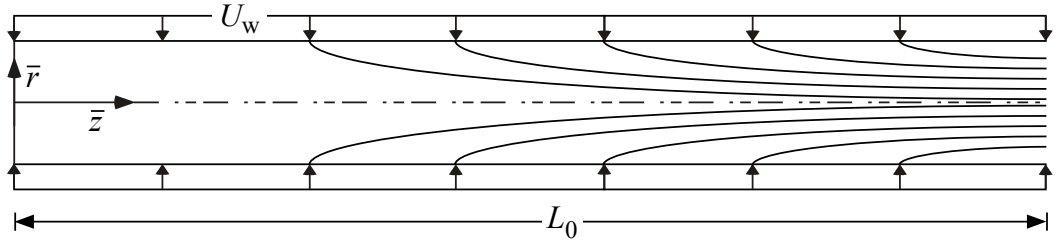

(b) Culick profile

Figure 1.1: The (a) Hart-McClure and (b) Culick streamline profiles.

flexibility of the method in calculating the compressible analogs to vortex pairs, as well as Hill's and Stuart's vortexes, respectively.

The Rayleigh-Janzen method is not limited to aerodynamic flows. Majdalani (2007a) employs the expansion to calculate the flow field in a cylindrical tube and Maicke and Majdalani (2008b) perform the same for a Cartesian channel flow. The approach has even been extended to include potential channel flow by Maicke et al. (2010) and later generalized by Saad et al. (2011) (see Figure 1.1). The ability of this perturbation technique to accommodate a wide range of geometric configurations, coupled with the subsonic speeds encountered in most propulsive applications all point to the Rayleigh-Janzen technique as an effective means of describing the compressible flow in a tangentially-driven combustor.

1.2 Experimental Correlation

Another challenge in developing analytical frameworks for engineering applications lies in reconciling with experiment. Specifically, most analytical studies are developed for

laminar conditions, whereas experiments frequently range into the turbulent regime. In order to make useful predictions, additional effort is required to adjust the model to match experimental conditions.

Empirically correlated relations are often employed in this capacity. In some cases, data is simply fit to the best available function, without any rigorous mathematical foundation. In other cases, certain key values in a derived framework are left undetermined and are subsequently used to match the experimental configuration. This type of algorithm is common in tornado and hurricane modeling where parameters such as the peak wind velocity, or circulation of a storm cell, are required to fully determine a solution. The drawback to this approach is that it is difficult to make predictions, as there is no valid solution without experimental inputs.

The other accepted practice is to determine the framework from first principles and then designate an experimental correction to one of the included laminar parameters. This has the advantage of producing a fully-functional model for laminar conditions while extending the range of validity to more physically realistic regimes after sufficient data is collected. The experimental correction approach has been used successfully in a number of vortex related studies, most notably by Rietema (1961) and by Kuo (1966). A variation of this method will be used in Chapter 7 to correlate swirl velocities to available experimental data.

1.3 Motivation

The motivation of this work is to provide an improved model for swirl-based combustors. One of the target applications is the bidirectional vortex liquid rocket engine developed by Orbital Technologies, depicted in Figure 1.2. The methodology detailed here may also be applied to swirl-based gas turbines or hybrid rocket motors with uni-directional or multi-directional axial velocities. To achieve this aim a framework is developed using the compressible analog of the Bragg-Hawthorne equations. A second framework is also developed using the vorticity-stream function approach (Majdalani, 2007a; Maicke and

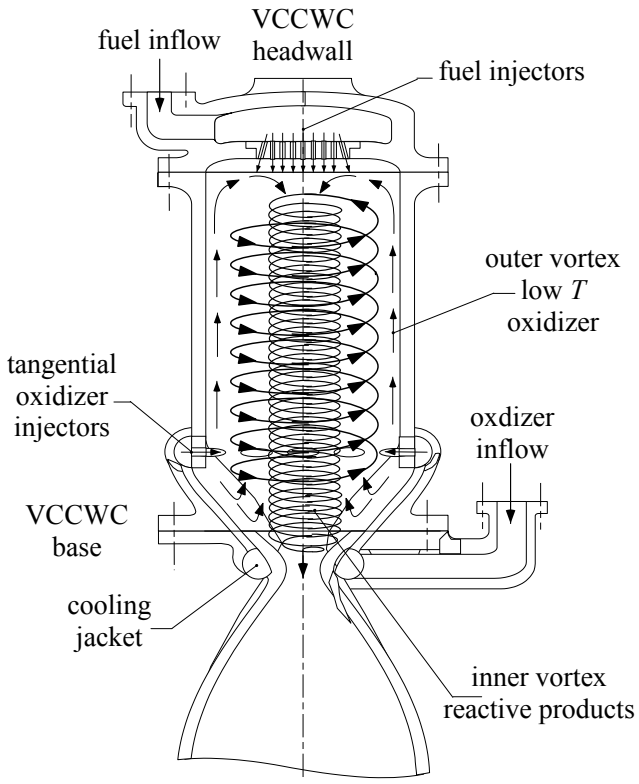

Figure 1.2: Concept sketch of the Vortex Combustion Cold-Wall Chamber (VCCWC) by Chiaverini et al.

Majdalani, 2008b) that remains popular in propulsion circles. The resulting equations are then solved with a semi-analytical approach to produce a closed form solution containing a number of special functions evaluated through numerical integration. In this dissertation, an alternate swirl velocity is developed through the balancing of the pressure and shear stress terms near the core of the vortex. The results are subsequently compared to both existing models and experimental data.

The remainder of this dissertation is structured as follows. Chapter 2 provides background on vortex-related research and introduces several classical vortex models. The derivations of the compressible framework and the constant shear stress swirl model are presented in Chapter 3. In Chapter 4, the Rayleigh-Janzen perturbation expansion is introduced along with the segregated compressible equations. Chapters 5 and 6 present the solutions to the compressible models and the alternate swirl velocity

model, respectively. The results are presented in Chapter 7 and the closing remarks are contained in Chapter 8.

Chapter 2

Vortex Models

In this chapter a review of existing vortex models is conducted. First potential applications are presented in both unbounded and confined domains, as well as the experimental methods used to acquire data in these contexts. Next, a survey of the classical analytical models is conducted, covering both uni- and multi-directional classifications. The salient features of these models are discussed and some will be incorporated into the models derived in Chapter 3.

2.1 Unbounded Vortex Studies

The first studies in swirling flows center on unbounded vortexes. As naturally occurring flows are not likely to be confined, most of the research in this classification focuses on weather-related phenomena. In a historical review, Vatistas (2009) investigates Homer's description of the tidal whirlpool, finding the description qualitatively accurate. In this context, an inviscid model is often sufficient to capture the flow behavior as the length scales are large enough for viscous effects to play a minor role.

Tornadoes, and to a lesser extent waterspouts, dust devils and fire whirls, constitute one of the largest fields of study on unbounded swirl-driven flows (see Figure 2.1). Accurately modeling these phenomena is a challenging endeavor as tornadoes form quickly and unpredictably, so it is often difficult to acquire experimental data for

(a) Tornado **(b)** Waterspout

Figure 2.1: Photographs of a (a) tornado and a (b) waterspout. Credit: National Oceanic and Atmospheric Administration.

these violent storms. Generally speaking, a tornado consists of an inward radial and an upward axial velocity coupled with strong swirl. In some cases, tornadoes may also have a considerable downdraft near the centerline (Lewellen, 1993). As a consequence of scarce experimental data during the formative stages of a tornado study, a number of analytical frameworks have been appropriated to tornadoes including those by Rankine (1858), Burgers (1948), Rott (1958), and Sullivan (1959). The details of these classical studies will be presented in Section 2.3.

While there is significant interest in describing the tornado structure for its own sake, these analytical studies are often used in compound models to predict damage caused by these storms. For example, Holland et al. (2006) and Bech et al. (2009) both use a Rankine vortex in their forest damage prediction models. In a similar manner, Beck and Dotzek (2010) approach the inverse problem in categorizing tornado velocities based on forest damage analysis. It stands to reason that improving the baseline predictions will invariably lead to improvements in the composite frameworks as well.

After tornadoes, hurricanes comprise the remainder of the bulk of naturally occurring vortex research. Unlike tornadoes, which are difficult to predict and extremely localized, hurricanes have a prolonged development time and are larger in scale (see Figure 2.2). Despite these differences, a modified Rankine vortex stands

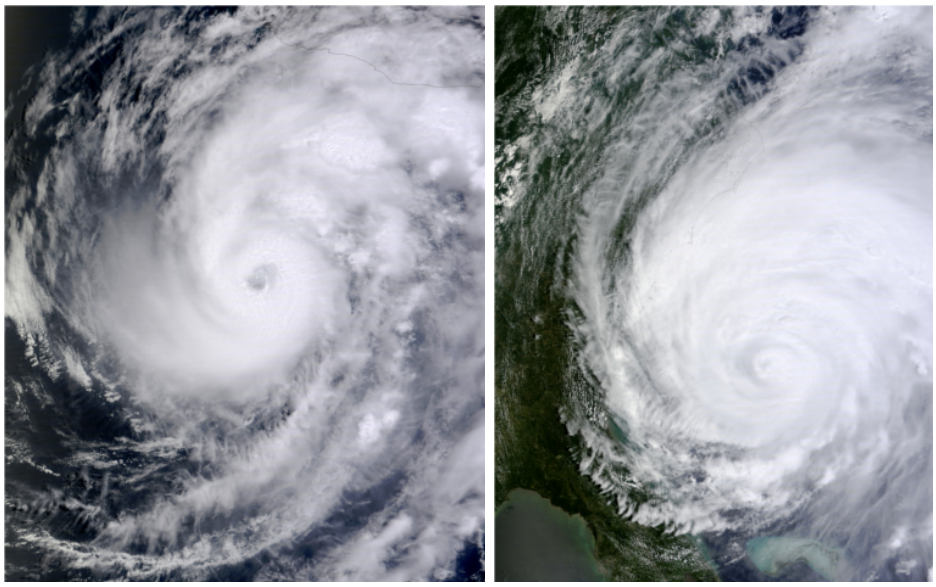

(a) Hurricane Bud **(b)** Hurricane Irene

Figure 2.2: Satellite images of (a) Hurricane Bud and (b) Hurricane Irene. Credit: NASA/GSFC/Jeff Schmaltz/MODIS Land Rapid Response Team.

as one of the first approximations for a hurricane description (Depperman, 1947). Subsequent investigations have developed new relations including those by Holland (1980) and Emanuel (1995). These models have an analytical basis, but require empirically correlated parameters to achieve closure.

Most current research on hurricanes focuses less on the velocity profile and more on the interactions with the environment. For example, Lindemer et al. (2010) conduct a numerical simulation on the changes experienced by a barrier island from erosion caused by the hurricane storm surge. There are a number of simulations of historical hurricanes, which are used to validate existing computations (Moscatello et al., 2008; Hogsett and Zhang, 2009).

Although tornadoes and hurricanes encompass a considerable percentage of active research in unbounded vortexes, there are a number of other avenues for the exploration of unbounded swirl-driven flows. In astronomy, Bruce (1961), and more recently Königl (1986), examine stellar jets by means of vortex mechanics. Vortex models can describe the features of distant galaxies, as the study by Afanas'ev and Fridman

(1993) likens the galaxy Mrk 1040 with a vortex rotating in shallow water. Klein et al. (2000) examine the role of vortex dynamics on the interaction of supernova remnants with interstellar clouds through a lab-scale experiment and numerical simulation of the nonlinear stability interactions.

Of primary interest in aerospace engineering, the vortexes shed by airfoils occupies an important line of inquiry. The research in this area is primarily experimental, as investigators examine the development, structure, and interactions of these vortexes. In a series of papers, (Devenport et al., 1996, 1997) first examine the vortex shed by a NACA 0012 half-wing and then the interaction between two such air-foils placed tip to tip. There are a number of possible applications for such research including aircraft spacing (Gerz et al., 2005), flow-separation control (Lin, 2002), and air-frame noise reduction (Makiya et al., 2010).

2.2 Confined Vortex Studies

A wealth of literature exists on swirl-driven flows in confined spaces. Unlike their unbounded brethren, the length scales in the confined vortex are necessarily smaller and the interactions with the walls may require additional treatment. Much of the early industrial vortex research is of the cyclone separator variety. For example, cyclone separator efficiency drives the investigation by ter Linden (1949). Bloor and Ingham (1987) have also introduced an incompressible formulation for a conical separator in spherical coordinates. In addition to these practical applications, the confined vortex possesses important academic value. As far as stability is concerned, Rusak et al. (1998) describe the evolution of a perturbed vortex in a pipe in an attempt to characterize axisymmetric breakdown. This work is further extended by Rusak and Lee (2004) to include compressible vortices. The intention of these studies is to not only characterize breakdown, but to also extend the mechanisms entailed in confined vortex breakdown to a more general stability model.

While only few analytical models have been proposed for describing the various swirl-dominated solutions of a confined vortex, there exists a significant body of literature devoted to experimental investigations. These studies can be roughly separated depending on the methods employed in their data collection: probes, Laser Doppler Velocimetry (LDV), and Particle Image Velocimetry (PIV).

Within the context of cyclone separators, the experimental study by Smith (1962b) employs a glass tube filled with smoke particles to capture the general structure of a confined swirling flow. Smith also utilizes a special slender probe stretched across the chamber diameter to determine the magnitude and direction of the velocity in the cyclone. This setup allows for the measurement of both the axial and tangential components. In this case, the radial velocity is assumed small enough that it can be inferred from continuity. In a companion paper, Smith (1962a) combines analytical methods with experimental measurements to characterize the dynamics and possible instabilities that occur in a separator.

In a later investigation into the behavior of cyclone chambers, Vatistas et al. (1986) conduct a similar experiment in which a prismatic pitot tube captures the velocity and pressure maps within a cyclonic chamber. These researchers compare their findings to an experimentally correlated inviscid description, finding essentially favorable agreement. Their study highlights a key realization in confined vortex modeling, namely, that swirl variations in the axial direction are so small that they may be ignored (see Reydon and Gauvin, 1981; Ogawa, 1984, among others). This simplification is commonly employed in the analytical studies of vortices.

Furthermore, these studies provide early insights into the conditions arising in a confined vortex; however, some deficiencies must be noted. Even with proper calibration, the minimally intrusive probes can introduce disturbances into the flow, and these, in turn, can lead to potentially misleading results. This is especially important when investigating dynamic effects such as instability.

Improvements in technology give rise to increasingly sophisticated experimental techniques that help to provide valuable information regarding confined swirl velocities

without the intrusion invariably present with even the smallest probes. For instance, LDV minimizes flow disruptions by seeding the fluid domain with particles followed by using a focused laser to scatter light off those particles. The interference patterns are then correlated to velocity measurements obtained in localized regions. Subsequently, the corresponding sub-volumes are summed together to reconstruct the overall profile of a given flow pattern.

Hoekstra et al. (1999) take an increasingly common approach of pairing a CFD solution with LDV measurements to validate their proposed turbulence models. Their experimental setup uses a back-scatter LDV to collect the axial and tangential profiles in small volumes. These volumes are then combined and correlated to provide an overall velocity profile. In this effort, however, the turbulent cross-correlation is found to be problematic owing to the finite chamber wall thickness which, in itself, can cause refraction and dissimilar distortion levels based on the spatial location within the chamber. Without proper accounting for these optical disparities, a perfect correlation between the acquired signal and the flow profile will be difficult to realize. The seeding quality in the core region also proves to be an issue, as the natural motion in the cyclone tends to separate particles from the flow.

Hu et al. (2005) conduct a similar study for industrial-size cyclone separators. Whereas Hoekstra et al. (1999) focus on the separation section of the cyclone, Hu et al. (2005) consider the full separator geometry including the inlet, hoppers, and other supporting hardware. Moreover, their experimental investigation is accompanied by a turbulent computational solution. In addition to verifying turbulent models, their study aims at improving the prediction of cyclone efficiency.

Along similar lines, an investigation into the turbulent kinetic energy of a confined vortex is reported in a forward scatter LDV study by Yan et al. (2000). In this work, data collected at a wide range of Reynolds numbers is used to validate their empirically derived solutions. These particular models rely on scaling laws to reduce the problem's dependence in each case to one or two key parameters, and these tend to involve some combination of the inlet flow rate and the contraction ratio.

PIV is another minimally intrusive technique that will be discussed in the remainder of this chapter. Much like LDV, PIV employs particle seeding to collect velocity measurements. The primary difference between the two techniques stands in the data acquisition. Whereas LDV relies on two focused beams to generate interference patterns, PIV uses optics to create a laser sheet that illuminates a plane in the chamber. High-speed cameras are then utilized to capture images of the illuminated particles at two closely spaced intervals such that a net profile may be deduced from the cross-correlation of these images.

By way of comparison, both PIV and LDV methods are used by Sousa (2008) to determine the velocity field that accompanies vortex breakdown in a closed container. Sousa finds that accurate measurements may be acquired using either method; he also reports several challenges associated with PIV techniques. The fully three-dimensional nature of the flow field can lead to a decrease in correlation accuracy as seed particles move normal to the light sheet. Sousa accounts for this factor by shortening the duration between laser pulses and by slightly thickening the laser sheet to increase the chances that the particles of interest will remain in the area of investigation.

In the spirit of improvement, Zhang and Hugo (2006) use a stereoscopic PIV setup to investigate the vortex motion in a pipe. Stereoscopic PIV captures the fully three-dimensional flow field; however, it requires an additional high speed camera with more elaborate calibration to ensure that both cameras will target the same area. This obviously leads to an increase in post-experimental processing as the images from two cameras have to be analyzed for each exposure, effectively doubling the amount of data acquired. Finally, Zhang and Hugo (2006) implement an improved calibration technique to reduce the optical distortion caused by refraction through the fluid and the curved chamber wall.

Cyclonic motions are also of interest in propulsive applications. For example, in hybrid rocket motors, this flow field is of interest primarily for increasing the oxidizer residence time as a means to improve the combustion performance. The benefits to this

type of motion have been applied by Knuth et al. (1996) in the context of a standard, cylindrical grain, while Rice et al. (2001) examine an end-burning configuration.

Liquid fueled combustors may also benefit from a swirl based design. In a unidirectional configuration, Anacleto et al. (2003) demonstrate a reduction in NO_x emissions when a lean mixture is used. Vortex flows may also used to stabilize flames in small-scale combustors (Wu et al., 2007). The motivation for this dissertation follows from a bidirectional variant of the swirl combustor, namely the VCCWC developed by Chiaverini et al. (2002).

2.3 Classical Vortex Models

When classifying analytical vortexes, the models may be split into unidirectional and multi-directional categories. Unidirectional models have an axial velocity in a single direction. Multi-directional vortexes have a reversing axial character. Tornadoes and cyclone separators are the most common physical manifestations of this latter type of behavior.

2.3.1 Unidirectional Models

Many of the first analytical models fall under the realm of unidirectional vortexes. One of the first efforts to capture such a flow analytically come from Rankine (1858), who developed a piecewise solution with a radial dependence. His normalized solution may be written as

$$\frac{\bar{v}}{\bar{v}_{\max}} = \begin{cases} \dfrac{\bar{r}}{\delta_c} & \bar{r} \leq \delta_c \\ \dfrac{\delta_c}{\bar{r}} & r > \delta_c \end{cases} \quad \text{or} \quad v = \begin{cases} r & r \leq 1 \\ r^{-1} & r > 1 \end{cases} \tag{2.1}$$

Here the over-bars denote a dimensional variable. The δ_c term represents the core distance, in this case, the distance from the centerline to the peak velocity. The core

distance is also sometimes referred to as the vortex strength, as a larger core radius will result in a higher peak for the Rankine profile. The inner domain consists of a forced core, behaving as a solid-body rotation, while the outer vortex varies with the inverse of the radius. Rankine focuses only on the tangential motion, neglecting the axial and radial components, though other velocities may be superimposed to form a complete model. In practice, the core distance and the maximum value must be known a priori and cannot be derived from first principles. This usually manifests in fitting to empirical data, either from experiment or simulation.

Owing to its simplicity, Rankine's model is often used as a first approximation or baseline during new development (see Bertato et al., 2003; Mallen et al., 2005). The simplicity is not without a cost, as the model is not differentiable at the matching point (see Figure 2.3), which may be undesirable during further calculations.

The Lamb-Oseen relation incorporates a time-dependent decay of the vortex motion (Wendt, 2001). This makes the model, derived from the axisymmetric, incompressible Navier-Stokes equations, particularly suitable for capturing the behavior of wing-tip vortices. The dimensional representation of its swirl velocity may be expressed as

$$\bar{v}(\bar{r},\bar{t}) = \frac{\Gamma}{2\pi\bar{r}}\left[1-\exp\left(-\frac{\bar{r}^2}{\delta^2}\right)\right] \tag{2.2}$$

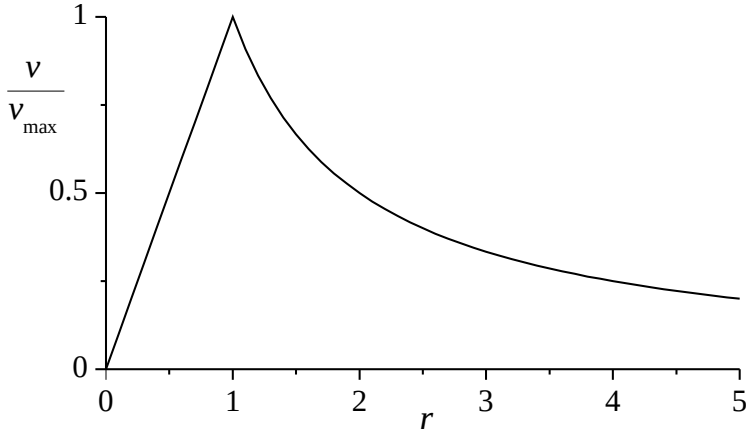

Figure 2.3: Normalized Rankine swirl velocity.

Here Γ refers to the circulation and $\delta = 2\sqrt{\nu \bar{t}}$, to the characteristic radius which is dependent on time, $\bar{t}$, and the kinematic viscosity, ν. Equation (2.2) begins as a potential vortex, behaving as $1/\bar{r}$ away from the centerline before smoothly switching to a linear dependence on $\bar{r}$ in the forced core evolving around $\bar{r} = 0$. As time elapses, the vortex decays exponentially. The swirl profile of the Lamb-Oseen equation is highlighted in Figure 2.4.

The Burgers-Rott vortex (Burgers, 1948; Rott, 1958) is similar in form to the Lamb-Oseen profile with two notable exceptions. First, rather than a time-dependent decay, the exponential function here is governed by the suction strength, S, which is either determined empirically or through the boundary conditions, depending on the study. Secondly, Burgers-Rott possesses well-defined relations for the axial and radial velocities. It can be written as

$$\begin{aligned} \bar{v}(\bar{r}) &= \frac{\Gamma}{2\pi\bar{r}}\left[1 - \exp\left(-\frac{\bar{r}^2}{\delta^2}\right)\right] \\ \bar{u}(\bar{r}) &= -S\bar{r}; \qquad \bar{w}(\bar{z}) = 2S\bar{z} \end{aligned} \tag{2.3}$$

where $\delta = \sqrt{2\nu/S}$. The presence of an axial velocity and a suction parameter has proven useful in applications related to the modeling of thunderstorms. The Burgers-Rott and Lamb-Oseen descriptions feature the inner, forced core which smoothly

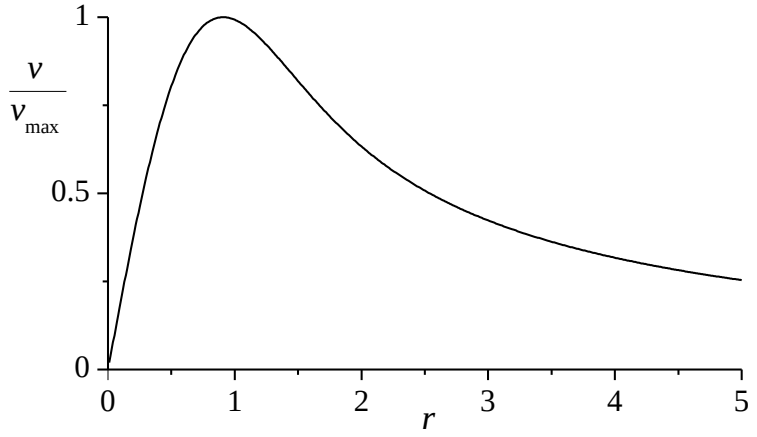

Figure 2.4: Lamb-Oseen swirl velocity.

transitions to the $1/r$ outer, free vortex. The primary difference between Burgers-Rott and Lamb-Oseen lies in the transition shape between these two features. The Lamb-Oseen vortex has a wider transition whereas the Burgers-Rott profile narrows for similar input values (see Figure 2.5).

While the swirl velocity exhibits a similar composition to the Lamb-Oseen vortex, the Burgers-Rott is the first description with off-swirl velocities. To fully characterize this field, the streamlines are plotted in Figure 2.6. In the first figure, the $r - \theta$ plane captures the coupling between the swirl and radial velocities. The flow field has an inwardly spiraling character along with an axial velocity that increases with z.

2.3.2 Bidirectional Solutions

In what concerns bidirectional behavior, Sullivan (1959) provides an unbounded bipolar solution to the Navier–Stokes equations. For an essentially two-celled vortex, Sullivan's inner region exhibits a descending axial velocity coupled with an outward radial motion. Conversely, the outer cell flows inwardly and up. The model itself can

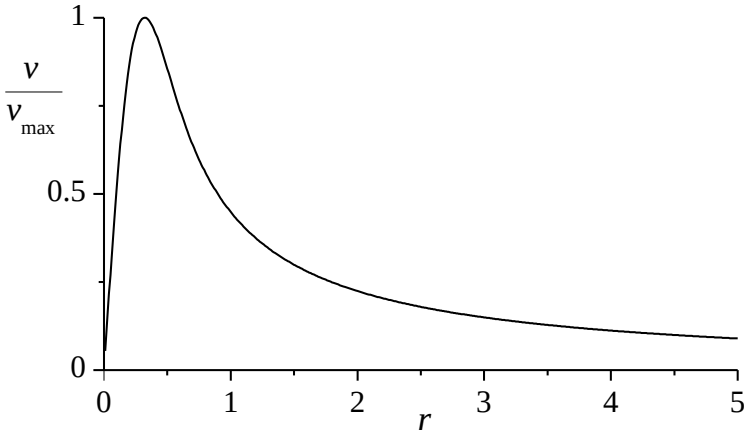

Figure 2.5: Burgers-Rott swirl velocity.

(a) Polar Streamlines

(b) Axial Streamlines

Figure 2.6: The (a) polar and (b) axial streamlines for the Burgers-Rott vortex.

be written in an integral representation using

$$\begin{cases} \bar{v}(\bar{r}) = \dfrac{\Gamma}{2\pi\bar{r}} \dfrac{1}{H(\infty)} H\left(\dfrac{\bar{r}^2}{\delta^2}\right); \quad \delta = \sqrt{2\nu/S} \\ H(x) = \displaystyle\int_0^x e^{f(t)} \mathrm{d}t; \quad f(t) = -t + 3\int_0^t \left(1 - e^{-y}\right) \dfrac{\mathrm{d}y}{y} \end{cases} \tag{2.4}$$

As before, S denotes the suction strength and ν, the kinematic viscosity. The corresponding axial and radial components may be expressed as

$$\bar{w}(\bar{r}, \bar{z}) = 2S\bar{z}\left[1 - 3\exp\left(-\frac{\bar{r}^2}{\delta^2}\right)\right]; \quad \bar{u}(\bar{r}) = -S\bar{r} + \frac{6\nu}{\bar{r}}\left[1 - \exp\left(-\frac{\bar{r}^2}{\delta^2}\right)\right] \tag{2.5}$$

It is the combination of axial and radial velocities that makes Sullivan a suitable candidate for tornadoes (Wu, 1986) and hurricanes (Nolan and Farrell, 1999). Figure 2.7 shows the two-cell structure described by the Sullivan model. The inner region consists of a downward moving, outwardly spiraling cell. The outer portion moves axially upwards while spiraling towards the vortex center. In these cases, the Sullivan model tends to over-predict the maximum swirl; like the Rankine vortex, an empirical correlation often modifies the Sullivan profile.

Instead of developing a general model for vortex motions, as in the previous examples, Kuo (1966) formulates a two-celled framework for the express purpose of characterizing tornadoes. His model couples a doubly perturbed expansion with a similarity solution which accounts for temperature differentials in the tornado. In creating the framework, Kuo assumes an unstable stratification layer of height, h, determined by the atmospheric conditions, and a reference swirl velocity of U. In keeping with the earlier studies, Majdalani (2012) presents a normalized form which may be written as

$$v = \frac{\delta_c}{\bar{r}} \frac{K(4.42\bar{r}^2/\delta_c^2)}{K(4.42)} \tag{2.6}$$

(a) Polar Streamlines

(b) Axial Streamlines

Figure 2.7: The (a) polar and (b) axial streamlines for the two-celled Sullivan (1959) vortex.

Here $\delta_c = 4.21\sqrt{\nu h/U}$ and K may be defined as

$$K(x) = \int_0^x e^{f(t)}\mathrm{d}t;\ f(t) = -t + 2\int_0^t (1 - e^{-y})\frac{\mathrm{d}y}{y} \tag{2.7}$$

The off-swirl velocity components are

$$u = 6.65\kappa_\infty \left\{ -2.21r + \frac{1}{r}\left[1 - \exp\left(-4.42r^2\right)\right] \right\} \tag{2.8}$$

$$v = 29.41\kappa_\infty z\left[1 - 2\exp\left(-4.42r^2\right)\right] \tag{2.9}$$

where $\kappa_\infty = \nu/\Gamma_\infty$, which behaves as an off-swirl parameter with the kinematic viscosity divided by the far-field circulation. The streamline plots for Kuo are featured in Figure 2.8. The structure is reminiscent of the two-celled Sullivan vortex with an inner downdraft and an outer updraft. The radial profile also follows a similar trend with a positive radial velocity in the core region that switches polarity to a negative value in the outer cell.

A comparison of the above-mentioned swirl velocities is presented in Figure 2.9. In all cases, the equations are normalized such that their peak velocities occur at a dimensionless radius of one. This is accomplished by dividing the radius by δ_c, which is the distance from the axis of rotation to the point where the maximum swirl occurs. Traditionally, a diameter of $2\delta_c$ may be used to define the forced viscous core thickness. While all of the models capture similar trends, there remains a significant amount of variability in the profiles. The Rankine solution displays an abrupt change in behavior at the peak. The remaining profiles exhibit smooth contours, with the Sullivan profile concentrating the swirl velocity to a narrower region than that of Burgers-Rott. Although not depicted, the Lamb-Oseen profile becomes identical to that of Burgers-Rott when neglecting time dependence.

In work related to cyclone separators, a study by Bloor and Ingham (1987) leads to one of the most frequently cited models. The resulting inviscid solution arises in the context of a conical cyclone. Bloor and Ingham solve the Bragg-Hawthorne equation

(a) Polar Streamlines

(b) Axial Streamlines

Figure 2.8: The (a) polar and (b) axial streamlines for the Kuo (1966) vortex.

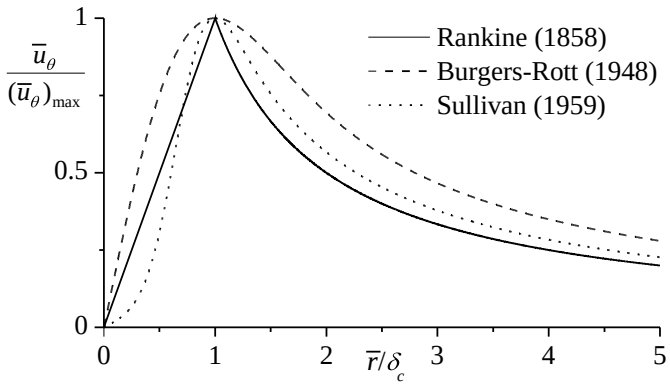

Figure 2.9: A comparison of selected swirl velocity models, normalized so that the peak velocity occurs at $r = 1$.

in spherical coordinates to the extent of producing a stream function of the form

$$\psi = \frac{\sigma r^2}{2}(\lambda - \ln\Phi - \Phi\csc\phi) \tag{2.10}$$

Here $\Phi \equiv \tan(\phi/2)$ and $\lambda \equiv \ln[\tan(\alpha/2)]$. Equation (2.10) translates into the following components

$$u_R = \pi\sigma[(\lambda - \ln\Phi)\cos\phi - 1] \tag{2.11}$$

$$u_\phi = -\pi\sigma[(\lambda - \ln\Phi)\sin\phi - \Phi] \tag{2.12}$$

$$u_\theta = (1/r)\sqrt{1 + \pi^2\sigma^2 r^2(\lambda - \ln\Phi - \Phi\csc\phi)} \tag{2.13}$$

Here U and W stand for the average swirl and axial velocities at the entrance (see Figure 2.10), α represents the cyclone taper angle, and σ refers to the dimensionless swirl parameter described by

$$\sigma = \frac{\pi U}{W} \tag{2.14}$$

Equations (2.10)–(2.14) constitute an improvement on previous work (Bloor and Ingham, 1973), where use of the Polhausen technique leads to a solution insensitive to injection conditions. It should also be noted that (2.10)–(2.14) represent a corrected form of the Bloor–Ingham solution according to Barber and Majdalani (2009).

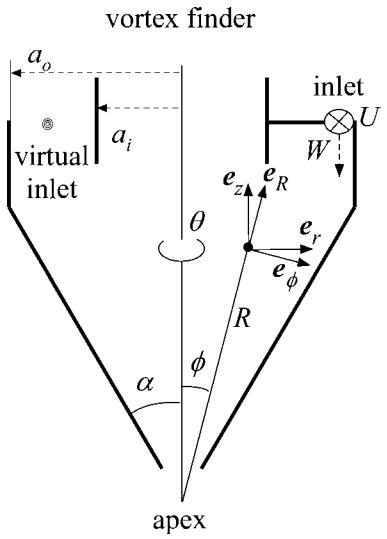

Figure 2.10: Bloor-Ingham solution domain and geometry.

Moving beyond the Bloor–Ingham approximation, Vyas and Majdalani (2006) introduce a bidirectional model with a reversing axial character. Their complex-lamellar solution, which constitutes the basis for the upcoming analysis, seeks to describe the bulk gaseous motion in the Vortex Combustion Cold-Wall Chamber (VCCWC) developed by Chiaverini et al. (2002). In this swirl-driven engine, the tangential motion of the oxidizer insulates the sidewalls against thermal loading, thus leading to a substantial reduction in engine weight. The swirling motion also has a mitigating impact on pressure oscillations in the chamber as shown by Batterson and Majdalani (2011a,b). The mathematical character of this application is described in the following chapter.

Chapter 3

Framework Derivations

In this chapter, the confined vortex frameworks are derived. The first model uses the vorticity-stream function approach, a mainstay of the propulsion community as evidenced by the work of Culick (1966), Vyas and Majdalani (2006), and Maicke and Majdalani (2008b). Second, the compressible Bragg-Hawthorne equations are derived. These relations are not as popular in the propulsion community, but have been successfully employed in the modeling of cyclone separators (see Bloor and Ingham, 1987). The Bragg-Hawthorne relations may be considered a super-set of the vorticity-stream function approach, as with careful consideration, one may recover a form similar to the vorticity-stream function framework. Finally, the constant shear stress model is briefly introduced. These equations provide the groundwork for the remainder of the study.

3.1 Bidirectional Vortex Model

The bidirectional vortex engine may be represented as a right circular cylinder with radius a and length L_0 as shown in Figure 3.1. The coordinate system is fixed at the center of the inert headwall, and the chamber is partially open at the base with a radius of b. The radial and axial coordinates are denoted by $\bar{r}$ and $\bar{z}$. Fluid is injected with tangential velocity U at the aft end. The injectant develops an axial velocity

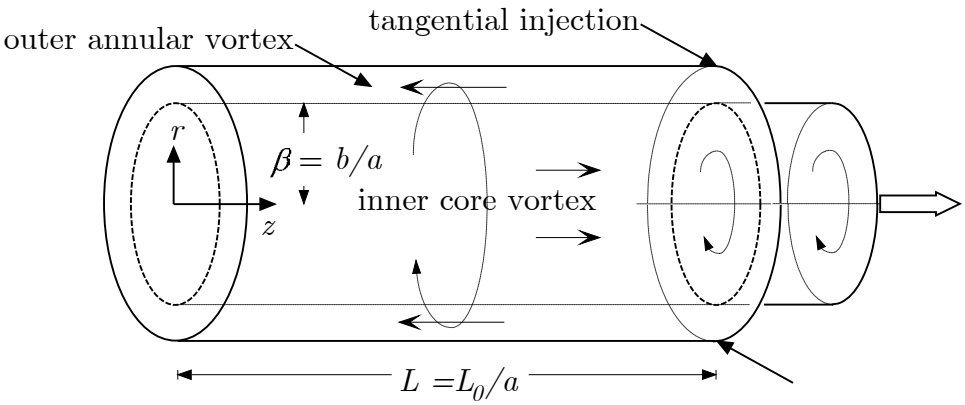

Figure 3.1: Schematic of the idealized bidirectional vortex chamber

and spirals up towards the headwall. When the flow reaches the headwall, it reverses axial direction and spirals back down the center of the chamber until it exits out the partially open base. The geometric parameters of interest are the aspect ratio $L = L_0/a$ and the open radius fraction $\beta = b/a$. In designing a experiment, β is often set to the location of the mantle which is defined as the location of zero axial velocity. By accounting for this key flow field feature, recirculation regions in the exit plane are minimized as the flow passing through the open fraction remains unidirectional. The bidirectional vortex flow field differs from traditional industrial cyclones in that it only has one outlet for the fluid to exit the chamber, rather than the two (one at the head end and one at the bottom) common in cyclone separators.

Physically, the flow field originates with tangential fluid injection at the base. Due to practical constraints, the entering fluid is not purely tangential, but will inevitably have some axial and radial components. As the chamber begins to fill, particle collisions with the side and endwalls promote the axial and radial velocity components. A portion of the fluid will exit through the open fraction at the base, while the remainder will continue to spiral up towards the headwall. In the vicinity of the headwall, collisions will again influence the axial velocity such that the direction of the flow is reversed. At this point the flow begins is decent in the inner region of the chamber, until finally exiting through the open fraction at the base.

Mathematically, the bidirectional vortex may be modeled with the ensuing boundary conditions

$$\bar{r} = a,\ \bar{z} = L_0,\ \bar{v} = U \qquad \text{Tangential injection at base} \tag{3.1}$$

$$\bar{r} = 0,\ \forall \bar{z},\ \bar{v} = 0 \qquad \text{Forced vortex core} \tag{3.2}$$

$$\bar{z} = 0,\ \forall \bar{r},\ \bar{w} = 0 \qquad \text{Impervious headwall} \tag{3.3}$$

$$\bar{r} = 0,\ \forall \bar{z},\ \bar{u} = 0 \qquad \text{No flow across centerline} \tag{3.4}$$

$$\bar{r} = a,\ \forall \bar{z},\ \bar{u} = 0 \qquad \text{Impervious sidewall} \tag{3.5}$$

$$\int_0^b 2\pi\rho\bar{w}(\bar{r}, L_0)\bar{r}\mathrm{d}\bar{r} = \bar{\dot{m}}_i \qquad \text{Axial outflow matching tangential source} \tag{3.6}$$

3.2 Normalization

Before introducing the frameworks, it is beneficial to convert the governing equations to non-dimensional form. The normalization relations are

$$z = \frac{\bar{z}}{a};\ r = \frac{\bar{r}}{a};\ \nabla = a\bar{\nabla};\ \beta = \frac{b}{a} \tag{3.7}$$

$$u = \frac{\bar{u}}{U};\ v = \frac{\bar{v}}{U};\ w = \frac{\bar{w}}{U};\ \mathbf{\Omega} = \frac{a\bar{\mathbf{\Omega}}}{U};\ \psi = \frac{\bar{\psi}}{\rho_0 U a^2};\ H = \frac{\bar{H}}{U^2} \tag{3.8}$$

$$p = \frac{\bar{p}}{p_0};\ \rho = \frac{\bar{\rho}}{\rho_0};\ Q = \frac{\bar{Q}}{Ua^2} = \frac{A_i}{a^2};\ \dot{m} = \frac{\bar{\dot{m}}}{\rho_0 U a^2} \tag{3.9}$$

where (z, r) represent the two primary spatial coordinates and b, the chamber exit radius. In (3.8), (u, v, w) denote the radial, azimuthal, and axial velocities, whereas $\mathbf{\Omega}$, ψ, and H are the vorticity, stream function and stagnation enthalpy, respectively. As usual, (p, ρ) are the standard thermodynamic properties; and Q represents the mass flow rate. In (3.7), all spatial coordinates are normalized by the chamber radius, a. Similarly, the wall-tangential injection velocity, U, normalizes the velocity variables, and the thermodynamic variables are divided by their respective reference value.

The vorticity-stream function and the Bragg-Hawthorne approaches both originate from the fundamental equations of fluid mechanics. For this reason, the conservation equations are first normalized and then used to derive the respective frameworks.

3.2.1 Conservation of Mass and Energy

The conservation of mass for steady, compressible flow is

$$\bar{\nabla} \cdot \left(\bar{\rho}\bar{\boldsymbol{U}}\right) = 0 \tag{3.10}$$

Substituting the values from (3.7)–(3.9) gives

$$\frac{\rho_0 U}{a} \nabla \cdot (\rho \boldsymbol{U}) = 0 \tag{3.11}$$

Dividing by the constants turns (3.11) into

$$\nabla \cdot (\rho \boldsymbol{U}) = 0 \tag{3.12}$$

Normalizing the energy equation follows the same procedure. Beginning with the expression

$$\nabla \cdot \left(\bar{\rho}\bar{H}\bar{\boldsymbol{U}}\right) = 0 \tag{3.13}$$

Substituting the normalized variables produces a collection of constants $(\rho_0 U^3/a)$ which can simply be divided out, as the right-hand side is zero.

3.2.2 Conservation of Momentum and Stagnation Enthalpy

The conservation of momentum for steady, compressible flow is

$$\bar{\boldsymbol{U}} \cdot \nabla \bar{\boldsymbol{U}} = -\frac{\nabla \bar{p}}{\bar{\rho}} \tag{3.14}$$

Introducing the non-dimensional forms of the variables produces

$$\frac{U^2}{a}\boldsymbol{U}\cdot\nabla\boldsymbol{U} = \frac{p_0}{\rho_0 a}\left(-\frac{\nabla\bar{p}}{\bar{\rho}}\right) \tag{3.15}$$

This is further simplified by introducing the speed of sound via $p_0/\rho_0 = c_0^2/\gamma$, which yields

$$\boldsymbol{U}\cdot\nabla\boldsymbol{U} = \frac{c_0^2}{\gamma U^2}\left(-\frac{\nabla\bar{p}}{\bar{\rho}}\right) \tag{3.16}$$

or, more appropriately

$$\boldsymbol{U}\cdot\nabla\boldsymbol{U} = -\frac{\nabla p}{\gamma M^2\rho} \tag{3.17}$$

Where M is the reference Mach number later used in the perturbation analysis.

The stagnation enthalpy is normalized in a similar manner to the momentum relation as it has analogous units, so it is not fully reproduced here. The dimensional form for the stagnation enthalpy for an ideal gas is

$$\bar{H} = \frac{1}{2}(\bar{\boldsymbol{U}}\cdot\bar{\boldsymbol{U}}) + \frac{\gamma}{\gamma-1}\frac{\bar{p}}{\bar{\rho}} \tag{3.18}$$

Dividing the velocity constants through and introducing the speed of sound where the pressure/density ratio appears results in a $1/(\gamma M^2)$ multiplying the thermodynamic terms as in (3.17).

The normalized equations facilitate comparisons across multiple trials and isolate control parameters, such as the Mach number or Reynolds number, which may guide experimental investigations. For the rest of this dissertation, the equations provided are in non-dimensional form unless explicitly stated.

3.2.3 Boundary Conditions

Before developing the dimensionless compressible systems, it is advantageous to recast the boundary conditions from (3.1)–(3.6) to the same non-dimensional format. Using

the same relations from (3.7)–(3.9), the boundary conditions are restructured to

$$v(1, L) = U \qquad \text{Tangential injection at base} \tag{3.19}$$

$$v(0, z) = 0 \qquad \text{Forced vortex core} \tag{3.20}$$

$$w(r, 0) = 0 \qquad \text{Impervious headwall} \tag{3.21}$$

$$u(0, z) = 0 \qquad \text{No flow across centerline} \tag{3.22}$$

$$u(1, z) = 0 \qquad \text{Impervious sidewall} \tag{3.23}$$

$$\dot{m}_i = 2\pi \int_0^{\beta} \rho w(r, L) r \mathrm{d}r \qquad \text{Axial outflow matching tangential source} \tag{3.24}$$

3.3 Vorticity-Stream Function Framework

The vorticity-stream function framework is a simplification of the Navier-Stokes equations that exploits symmetry in a reduction to a two-dimensional form via the stream function. The name originates from the relationship between the vorticity and the stream function that makes this possible. The incompressible version of this framework has been successfully employed in modeling solid rocket motors as depicted in Figure 3.2 (see Culick, 1966). The equations have also been used by Vyas and Majdalani (2006) to describe the bidirectional vortex rocket engine. The framework is extended to compressible conditions through coupling with the definition for the compressible stream function. This has been successfully done by Majdalani (2007a)

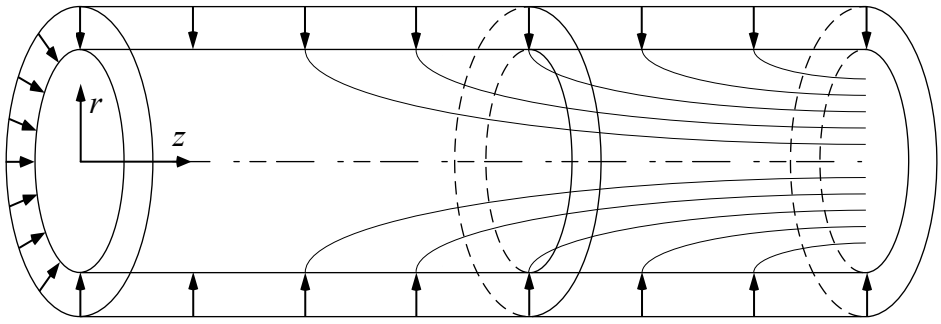

Figure 3.2: Schematic of a cylindrical rocket motor with streamlines.

for the cylindrical solid rocket motor and by Maicke and Majdalani (2008b) for the Cartesian geometry.

In this section, the compressible vorticity-stream function (CVS) framework is presented. The derivation differs slightly from previous studies in that it retains both the compressible flow terms and the azimuthal velocity that is vital to the modeling of confined vortex flows. Previous studies include one extension or the other, but not both together.

3.3.1 Vorticity Equation

The derivation of the primary equation stems from the vorticity definition. Recalling that for cylindrical coordinates the vorticity is

$$\boldsymbol{\Omega} = \nabla \times \boldsymbol{U} = \frac{1}{r}\left[\frac{\partial w}{\partial \theta} - \frac{\partial (rv)}{\partial z}\right]\hat{e}_r - \left(\frac{\partial w}{\partial r} - \frac{\partial u}{\partial z}\right)\hat{e}_\theta + \frac{1}{r}\left[\frac{\partial (rv)}{\partial r} - \frac{\partial u}{\partial \theta}\right]\hat{e}_z \quad (3.25)$$

Even though the bidirectional vortex has a swirl velocity, it remains axisymmetric in nature; thus the azimuthal derivatives are eliminated. Furthermore, it is common in confined vortex flows to remove any axial dependence from the swirl velocity. These axioms reduce (3.25) to

$$\boldsymbol{\Omega} = -\left(\frac{\partial w}{\partial r} - \frac{\partial u}{\partial z}\right)\hat{e}_\theta + \frac{1}{r}\left[\frac{\partial (rv)}{\partial r}\right]\hat{e}_z \quad (3.26)$$

Equation (3.26) yields two separate, non-coupled vector components. The equation in the azimuthal direction forms the basis for the stream function relation, whereas the axial element reflects the swirl velocity decoupling from the axial and radial velocities.

Before returning to the azimuthal vorticity, the compressible stream function definitions are required, namely,

$$u = -\frac{1}{\rho r}\frac{\partial \psi}{\partial z}; \quad w = \frac{1}{\rho r}\frac{\partial \psi}{\partial r} \quad (3.27)$$

Substituting (3.27) back into the azimuthal vorticity expression gives

$$\Omega_\theta = -\frac{\partial}{\partial r}\left(\frac{1}{\rho r}\frac{\partial \psi}{\partial r}\right) - \frac{\partial}{\partial z}\left(\frac{1}{\rho r}\frac{\partial \psi}{\partial z}\right) \tag{3.28}$$

Expanding the derivatives yields

$$\Omega_\theta = \frac{1}{r\rho^2}\frac{\partial \rho}{\partial z}\frac{\partial \psi}{\partial z} - \frac{1}{\rho z}\frac{\partial^2 \psi}{\partial z^2} - \frac{1}{\rho r}\frac{\partial^2 \psi}{\partial r^2} + \frac{1}{\rho r^2}\frac{\partial \psi}{\partial r} + \frac{1}{\rho^2 r}\frac{\partial \rho}{\partial r}\frac{\partial \psi}{\partial r} \tag{3.29}$$

Multiplying through by $r\rho^2$ and collecting terms provides

$$\rho D^2\psi + r\rho^2\Omega_\theta = \frac{\partial \rho}{\partial z}\frac{\partial \psi}{\partial z} + \frac{\partial \rho}{\partial r}\frac{\partial \psi}{\partial r} \tag{3.30}$$

where

$$D^2 \equiv \frac{\partial^2}{\partial r^2} - \frac{1}{r}\frac{\partial}{\partial r} + \frac{\partial^2}{\partial z^2} \tag{3.31}$$

The right-hand side of (3.30) can be further simplified through the use of vector notation, viz.

$$\rho D^2\psi + r\rho^2\Omega_\theta = \nabla\rho \cdot \nabla\psi \tag{3.32}$$

Equation (3.32) is the final form of the vorticity-stream function equation.

3.3.2 Vorticity Transport Equation

To solve (3.32), an additional closure relation is required to connect the vorticity to the stream function, thus eliminating the Ω_θ term on the left hand side. To that end, the momentum definition from (3.17) is expanded for cylindrical coordinates. The equation becomes

$$\frac{\nabla(\boldsymbol{U}\cdot\boldsymbol{U})}{2} - \boldsymbol{U}\times\nabla\times\boldsymbol{U} = -\frac{\nabla p}{\gamma M^2\rho} \tag{3.33}$$

Using the vorticity definition and taking the cross product of (3.33) gives

$$\nabla\times(\boldsymbol{U}\times\boldsymbol{\Omega}) = \frac{1}{\gamma M^2\rho^2}\nabla\rho\cdot\nabla p \tag{3.34}$$

Equation (3.34) provides the required closure by relating the vorticity to the stream function by way of the velocity terms.

3.3.3 Momentum Equation

To close the vorticity-stream function model, the pressure and density are required at each order. The pressure is calculated from the momentum, while the density is extracted from the isentropic relations. Starting with the compressible momentum, (3.17), and expanding the equation into its vector constituents, the radial momentum equation becomes

$$u\frac{\partial u}{\partial r} - \frac{v^2}{r} + w\frac{\partial u}{\partial z} = -\frac{1}{\gamma M^2 \rho}\frac{\partial p}{\partial r} \tag{3.35}$$

and the axial pressure may be found from

$$w\frac{\partial w}{\partial z} + u\frac{\partial w}{\partial r} = -\frac{1}{\gamma M^2 \rho}\frac{\partial p}{\partial z} \tag{3.36}$$

The remaining thermodynamic variables may be determined from the isentropic relations. For the density and the pressure, these are

$$\rho = p^{1/\gamma} \tag{3.37}$$

$$T = p^{1-1/\gamma} \tag{3.38}$$

3.4 Compressible Bragg-Hawthorne Framework

The original model developed by Bragg and Hawthorne (1950) is used to analyze incompressible vortex flows. Bloor and Ingham (1987) employ a variation of this technique in spherical coordinates to analyze the flow in an industrial cyclone (see Figure 3.3). Their framework employs a set of simplifications to reduce the Navier-Stokes equations to a stream function form. The result is a set of relations dependent on the stream function, stagnation enthalpy, and circulation. An investigator may

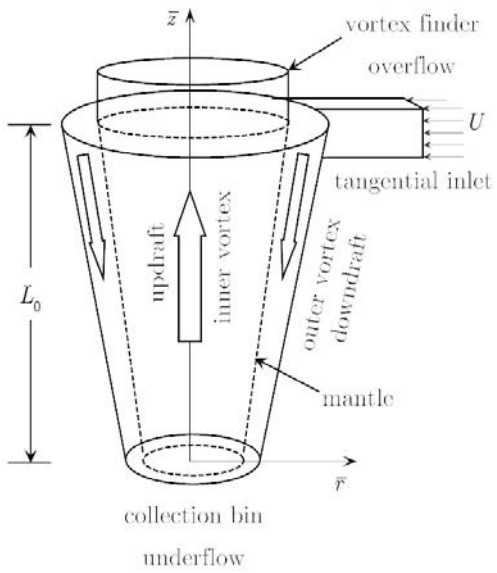

Figure 3.3: Schematic of an industrial cyclone.

specify the latter two to values appropriate to the problem. In this section, the traditional Bragg-Hawthorne approach is extended to account for compressibility.

3.4.1 Bragg-Hawthorne Stream Function Equation

The definition of the stagnation enthalpy for a perfect gas is

$$H = \frac{1}{2}\left(\boldsymbol{u}\cdot\boldsymbol{u}\right) + \frac{1}{M^2\left(\gamma-1\right)}\frac{p}{\rho} \tag{3.39}$$

Before deriving the compressible Bragg-Hawthorne (CBH) equation, the stagnation enthalpy and circulation must be written in terms of the stream function. The general form of the energy equation may be expressed as

$$\nabla\cdot\left(\rho H\boldsymbol{U}\right) = 0 \tag{3.40}$$

One may expand the dot product to produce

$$\nabla\left(\rho H\right)\cdot\boldsymbol{U} + \rho H\left(\nabla\cdot\boldsymbol{U}\right) = 0 \tag{3.41}$$

The conservation of mass is expanded in a similar manner to provide

$$\nabla \cdot \boldsymbol{U} = -\frac{\nabla \rho \cdot \boldsymbol{U}}{\rho} \tag{3.42}$$

Substituting (3.42) back into (3.41) gives

$$\nabla \left(\rho H\right) \cdot \boldsymbol{U} - H \left(\nabla \rho \cdot \boldsymbol{U}\right) = 0 \tag{3.43}$$

Expanding the first term leads to

$$\rho \left(\nabla H \cdot \boldsymbol{U}\right) + H \left(\nabla \rho \cdot \boldsymbol{U}\right) - H \left(\nabla \rho \cdot \boldsymbol{U}\right) = 0 \tag{3.44}$$

The last two terms are equal in magnitude but opposite in sign. This leaves

$$\nabla H \cdot \boldsymbol{U} = 0 \tag{3.45}$$

Equation (3.45) proves that H only varies perpendicularly to the velocity; thus, H may be written in terms of the stream function,

$$H = H(\psi) \tag{3.46}$$

With the stagnation enthalpy in hand, the expanded azimuthal component of (3.33) may be revisited. Invoking axisymmetry reduces the θ-momentum equation to

$$u\frac{\partial v}{\partial r} + w\frac{\partial v}{\partial z} + \frac{uv}{r} = 0 \tag{3.47}$$

Multiplying (3.47) by r reproduces the material derivative of $\mathrm{B} \equiv rv$ such that

$$ru\frac{\partial v}{\partial r} + rw\frac{\partial v}{\partial z} + uv = \frac{\mathrm{D}(rv)}{\mathrm{D}t} = \frac{\mathrm{DB}}{\mathrm{D}t} = 0 \tag{3.48}$$

A vanishing material derivative confirms that B must remain invariant along streamlines, and so $\mathrm{B} = \mathrm{B}(\psi)$.

With H and Γ in stream function form, they prove useful in simplifying the momentum equation. This is facilitated by the isentropic relation, namely,

$$p = K\rho^{\gamma} \tag{3.49}$$

where K denotes a general constant. At this juncture, one may recognize that matching the momentum given by (3.33) requires a pressure gradient divided by the density. To that end, (3.49) is manipulated to provide

$$\nabla\left(\frac{p}{\rho}\right) = K\nabla\rho^{\gamma-1} \tag{3.50}$$

To separate ∇p from the other terms, the following relation is introduced

$$\rho_t = \rho^{\gamma} \tag{3.51}$$

Equation (3.50) becomes

$$\nabla\left(\frac{p}{\rho}\right) = K\nabla\rho_t^{\,1-\frac{1}{\gamma}} \tag{3.52}$$

Further chain rule differentiation isolates ρ_t to give

$$\nabla\left(\frac{p}{\rho}\right) = K\left(1-\frac{1}{\gamma}\right)\rho_t^{\,-\frac{1}{\gamma}}\nabla\rho_t \tag{3.53}$$

Reverting back to the original density renders

$$\nabla\left(\frac{p}{\rho}\right) = K\left(\frac{\gamma-1}{\gamma}\right)\rho^{-1}\nabla\rho^{\gamma} \tag{3.54}$$

Finally, substituting (3.49) back into (3.54) yields

$$\frac{\gamma}{\gamma-1}\nabla\left(\frac{p}{\rho}\right) = \frac{\nabla p}{\rho} \tag{3.55}$$

This expression matches its counterpart on the right-hand side of (3.17).

After substituting (3.55) into the compressible momentum equation (3.17), one may employ the vector identity, $\boldsymbol{U} \cdot \nabla \boldsymbol{U} = \frac{1}{2}\nabla \boldsymbol{U}^2 - \boldsymbol{U} \times \boldsymbol{\Omega}$, to obtain

$$\frac{\nabla(\boldsymbol{U} \cdot \boldsymbol{U})}{2} + \frac{1}{M^2\left(\gamma - 1\right)}\nabla\left(\frac{p}{\rho}\right) - \boldsymbol{U} \times \boldsymbol{\Omega} = 0 \tag{3.56}$$

The first two terms correspond to the gradient of the stagnation enthalpy, or

$$\nabla H = \boldsymbol{U} \times \boldsymbol{\Omega} \tag{3.57}$$

To eliminate the vorticity, the right-hand side of (3.57) may be expanded in terms of the velocity viz.

$$\begin{aligned}\boldsymbol{u} \times \boldsymbol{\Omega} = &\left\{\frac{v}{r}\left[\frac{\partial\left(rv\right)}{\partial r} - \frac{\partial u}{\partial \theta}\right] + w\left(\frac{\partial w}{\partial r} - \frac{\partial u}{\partial z}\right)\right\}\hat{e}_r \\ &- \left\{\frac{u}{r}\left[\frac{\partial\left(rv\right)}{\partial r} - \frac{\partial u}{\partial \theta}\right] - \frac{w}{r}\left[\frac{\partial w}{\partial \theta} - \frac{\partial\left(rv\right)}{\partial z}\right]\right\}\hat{e}_\theta \\ &+ \left\{-u\left(\frac{\partial w}{\partial r} - \frac{\partial u}{\partial z}\right) - \frac{v}{r}\left[\frac{\partial w}{\partial \theta} - \frac{\partial\left(rv\right)}{\partial z}\right]\right\}\hat{e}_z\end{aligned} \tag{3.58}$$

As with the vorticity-stream function, the axial component of (3.57) can be segregated after imposing the axisymmetry condition to produce

$$\frac{\partial H}{\partial z} = -u\left(\frac{\partial w}{\partial r} - \frac{\partial u}{\partial z}\right) + v\frac{\partial v}{\partial z} \tag{3.59}$$

Next, the velocities may be eliminated in favor of the stream function via (3.27) such that

$$\frac{\partial H}{\partial z} = \frac{1}{\rho r}\frac{\partial \psi}{\partial z}\frac{\partial}{\partial z}\left(\frac{1}{\rho r}\frac{\partial \psi}{\partial z}\right) + \frac{1}{\rho r}\frac{\partial \psi}{\partial z}\frac{\partial}{\partial r}\left(\frac{1}{\rho r}\frac{\partial \psi}{\partial r}\right) + v\frac{\partial v}{\partial z} \tag{3.60}$$

At this stage, expanding the derivatives and factoring the angular momentum gives

$$\frac{\partial H}{\partial z} = \frac{1}{\rho^2 r^2}\frac{\partial \psi}{\partial z}\left(\frac{\partial^2 \psi}{\partial z^2} - \frac{1}{\rho}\frac{\partial \psi}{\partial z}\frac{\partial \rho}{\partial z} + \frac{\partial^2 \psi}{\partial r^2} - \frac{1}{\rho}\frac{\partial \psi}{\partial r}\frac{\partial \rho}{\partial r} - \frac{1}{r}\frac{\partial \psi}{\partial r}\right) + \frac{\Gamma}{r^2}\frac{\partial \Gamma}{\partial z} \tag{3.61}$$

Further application of the chain rule to the H and Γ terms generates

$$\frac{\partial H}{\partial \psi}\frac{\partial \psi}{\partial z} = \frac{1}{\rho^2 r^2}\frac{\partial \psi}{\partial z}\left(\frac{\partial^2 \psi}{\partial z^2} - \frac{1}{\rho}\frac{\partial \psi}{\partial z}\frac{\partial \rho}{\partial z} + \frac{\partial^2 \psi}{\partial r^2} - \frac{1}{\rho}\frac{\partial \psi}{\partial r}\frac{\partial \rho}{\partial r} - \frac{1}{r}\frac{\partial \psi}{\partial r}\right) + \frac{\Gamma}{r^2}\frac{\partial \Gamma}{\partial \psi}\frac{\partial \psi}{\partial z} \quad (3.62)$$

which collapses into

$$r^2\frac{\partial H}{\partial \psi} - \Gamma\frac{\partial \Gamma}{\partial \psi} = \frac{1}{\rho^2}\left(\frac{\partial^2 \psi}{\partial z^2} - \frac{1}{\rho}\frac{\partial \psi}{\partial z}\frac{\partial \rho}{\partial z} + \frac{\partial^2 \psi}{\partial r^2} - \frac{1}{\rho}\frac{\partial \psi}{\partial r}\frac{\partial \rho}{\partial r} - \frac{1}{r}\frac{\partial \psi}{\partial r}\right) \quad (3.63)$$

Taking advantage of vector notation and introducing the D^2 operator defined in (3.31), one arrives at the compact form,

$$D^2\psi + \rho^2\left(\Gamma\frac{\partial \Gamma}{\partial \psi} - r^2\frac{\partial H}{\partial \psi}\right) = \frac{1}{\rho}\nabla\rho\cdot\nabla\psi \quad (3.64)$$

It may be instructive to note that only B, H, and their derivatives with respect to ψ appear in (3.64). Therefore, given the general dependence of these quantities on the stream function, some freedom exists in the manner by which suitable forms of H and B may be specified. It is this flexibility that sets the Bragg-Hawthorne technique apart, particularly as a versatile and promising framework that can help to unravel multiple solutions for the same geometry and physical model. More detail on this point will be furnished in Section 4.2.

3.4.2 Compressible Energy Relation

The compressible Bragg-Hawthorne relation requires a density expression for closure. The stagnation enthalpy definition, (3.39), is a likely candidate. Rewriting it to include the stream function definitions from (3.27) yields

$$H - \frac{\Gamma^2}{r^2} = \frac{1}{2\rho^2 r^2}\left[\left(\frac{\partial \psi}{\partial z}\right)^2 + \left(\frac{\partial \psi}{\partial r}\right)^2\right] + \frac{1}{M^2(\gamma-1)}\frac{p}{\rho} \quad (3.65)$$

But $p = \rho^\gamma$, which eliminates the pressure term and provides an equation for the density

$$H - \frac{\Gamma^2}{r^2} = \frac{1}{2\rho^2 r^2}\left[\left(\frac{\partial\psi}{\partial z}\right)^2 + \left(\frac{\partial\psi}{\partial r}\right)^2\right] + \frac{1}{M^2\left(\gamma-1\right)}\rho^{\gamma-1} \tag{3.66}$$

Equation (3.66) and (3.64) are the basis for the solutions in the following chapters.

3.5 Constant Shear Stress Model

The constant shear stress model provides a piecewise swirl velocity solution that may be used to model confined vortex motions. The basis for the model is that a free vortex of the $1/r$ type develops away from the core of the vortex; in contrast, equilibrium is maintained near the core between the shear and pressure terms. This balance leads to a model that remains valid for both laminar and turbulent conditions. It is important to note that this is not a turbulent model as there are no unsteady effects included, but rather a mean velocity model that can be used as a base flow for turbulent regimes.

The justification for this model can be seen mathematically from the conservation of momentum, namely

$$\left(\boldsymbol{U}\cdot\nabla\right)\boldsymbol{U} = -\nabla p + \nabla\cdot\boldsymbol{\tau} \tag{3.67}$$

At the centerline, the azimuthal velocity goes to zero, which leaves the pressure and shear stress terms remaining to balance each other. The flow under consideration for this dissertation has a zero tangential pressure gradient, therefore the shear stress in the tangential direction may be assumed to be constant. The equation for the dominant shear stress can be written as:

$$\tau_{r\theta} = \epsilon\left[\frac{1}{r}\frac{\partial u}{\partial\theta} + r\frac{\partial}{\partial r}\left(\frac{v}{r}\right)\right] \tag{3.68}$$

where ϵ is the viscous parameter $1/\mathrm{Re}$. Since the flow is axisymmetric, the θ derivative is eliminated and the resulting equation becomes

$$\epsilon \left(\frac{\partial v}{\partial r} - \frac{v}{r} \right) = C_1 \tag{3.69}$$

The traditional forced vortex model can be recovered by setting the constant equal to zero, but the model developed here will retain the general constant.

Chapter 4

The Rayleigh-Janzen Perturbation Expansion

In seeking analytical approximations to the two coupled density-stream function relations, the Rayleigh-Janzen expansion may be used to linearize the ensuing system of equations. A similar technique is employed to model the compressible Taylor flow in porous channels driven by wall-normal injection (Maicke and Majdalani, 2008b). As done before, the principal variables of interest may be expanded in terms of the Mach number squared using:

$$
\begin{aligned}
u &= u_0 + M_0^2 u_1 + O(M_0^4) & \psi &= \psi_0 + M_0^2 \psi_1 + O(M_0^4) \\
v &= v_0 + M_0^2 v_1 + O(M_0^4) & B &= B_0 + M_0^2 B_1 + O(M_0^4) \\
w &= w_0 + M_0^2 w_1 + O(M_0^4) & H &= H_0 + M_0^2 H_1 + O(M_0^4) \\
\Omega_\theta &= \Omega_0 + M_0^2 \Omega_1 + O(M_0^4) & \rho &= 1 + M_0^2 \rho_1 + M_0^4 \rho_2 + O(M_0^6) \\
p &= 1 + M_0^2 p_1 + M_0^4 p_2 + O(M_0^6) & T &= 1 + M_0^2 T_1 + M_0^4 T_2 + O(M_0^6)
\end{aligned}
\tag{4.1}
$$

These expanded variables may be substituted back into the stream function and density expressions to produce a set of relations that may be solved sequentially.

As both the Bragg-Hawthorne and the vorticity-stream function approaches rely on the stream function substitution, it is beneficial to expand the velocity-stream function definition. Expanding (3.27) produces

$$(u_0 + M_0^2 u_1) = -\frac{1}{(1 + M_0^2\rho_1 + M_0^4\rho_2)r}\frac{\partial(\psi_0 + M_0^2\psi_1)}{\partial z} \tag{4.2}$$

$$(w_0 + M_0^2 w_1) = \frac{1}{(1 + M_0^2\rho_1 + M_0^4\rho_2)r}\frac{\partial(\psi_0 + M_0^2\psi_1)}{\partial r} \tag{4.3}$$

After collecting terms of $O(1)$ and $O(M_0^2)$ and simplifying, the radial velocity may be written as

$$O(1) : u_0 = -\frac{1}{r}\frac{\partial\psi_0}{\partial z} \tag{4.4}$$

$$O(M_0^2) : u_1 = \frac{\rho_1}{r}\frac{\partial\psi_0}{\partial z} - \frac{1}{r}\frac{\partial\psi_1}{\partial z} \tag{4.5}$$

Likewise, the axial velocity may be expressed as

$$O(1) : w_0 = \frac{1}{r}\frac{\partial\psi_0}{\partial r} \tag{4.6}$$

$$O(M_0^2) : w_1 = \frac{1}{r}\frac{\partial\psi_1}{\partial r} - \frac{\rho_1}{r}\frac{\partial\psi_0}{\partial r} \tag{4.7}$$

With these expanded velocity definitions, it is possible to rewrite the boundary conditions to accommodate the system of equations at each order. To be consistent with perturbation theory, the boundary conditions at the leading order must provide a complete solution to the system. The boundary conditions at subsequent orders revert to null values, so that they do not unduly influence the boundaries. For example, the impervious headwall condition may be systematically perturbed to generate

$$O(1) : w_0(r, 0) = \frac{1}{r}\frac{\partial\psi_0}{\partial r} = 0 \tag{4.8}$$

$$O(M_0^2) : w_1(r, 0) = \frac{1}{r}\frac{\partial\psi_1}{\partial r} - \frac{\rho_1}{r}\frac{\partial\psi_0}{\partial r} = 0 \tag{4.9}$$

Likewise, the radial centerline condition correlates to

$$O(1) : u_0(0,z) = -\frac{1}{r}\frac{\psi_0}{\partial z} = 0 \tag{4.10}$$

$$O(M_0^2) : u_1(0,z) = \frac{\rho_1}{r}\frac{\partial \psi_0}{\partial z} - \frac{1}{r}\frac{\partial \psi_1}{\partial z} = 0 \tag{4.11}$$

When separated, the impervious sidewall condition yields

$$O(1) : u_0(1,z) = -\frac{1}{r}\frac{\psi_0}{\partial z} = 0 \tag{4.12}$$

$$O(M_0^2) : u_1(1,z) = \frac{\rho_1}{r}\frac{\partial \psi_0}{\partial z} - \frac{1}{r}\frac{\partial \psi_1}{\partial z} = 0 \tag{4.13}$$

Finally, the mass conservation condition in segregated form leads to

$$\dot{Q}_i = 2\pi \int_0^\beta \frac{\partial \psi_0}{\partial r}(r,L)\mathrm{d}r \text{ or } \psi_0(\beta,L) - \psi_0(0,L) = \dot{Q}_i \tag{4.14}$$

$$0 = 2\pi \int_0^\beta \frac{\partial \psi_1}{\partial r}(r,L)\mathrm{d}r \text{ or } \psi_1(\beta,L) - \psi_1(0,L) = 0 \tag{4.15}$$

4.1 Expanded Bragg-Hawthorne Equations

A Rayleigh-Janzen series expansion of the compressible Bragg-Hawthorne equation renders

$$\begin{aligned}(1 + M_0^2\rho_1 + M_0^4\rho_2)D^2(\psi_0 + M_0^2\psi_1 + M_0^4\psi_2) + (1 + M_0^2\rho_1 + M_0^4\rho_2)^3 \\ \times \Bigg[(B_0 + M_0^2B_1 + M_0^4B_2)\frac{\mathrm{d}}{\mathrm{d}\psi}(B_0 + M_0^2B_1 + M_0^4B_2) \\ -r^2\frac{\mathrm{d}}{\mathrm{d}\psi}(H_0 + M_0^2H_1 + M_0^4H_2)\Bigg] \\ = \nabla(1 + M_0^2\rho_1 + M_0^4\rho_2)\cdot\nabla(\psi_0 + M_0^2\psi_1 + M_0^4\psi_2)\end{aligned} \tag{4.16}$$

Collecting leading and first-order quantities in M_0^2 enables us to identify:

$$O(1) : D^2\psi_0 + B_0\frac{\mathrm{d}B_0}{\mathrm{d}\psi} - r^2\frac{\mathrm{d}H_0}{\mathrm{d}\psi} = 0 \tag{4.17}$$

$$O(M_0^2) : D^2\psi_1 + B_1\frac{\mathrm{d}B_1}{\mathrm{d}\psi} - r^2\frac{\mathrm{d}H_1}{\mathrm{d}\psi} = \frac{\partial\rho_1}{\partial z}\frac{\partial\psi_0}{\partial z} + \frac{\partial\rho_1}{\partial r}\frac{\partial\psi_0}{\partial r} - \rho_1\left[D^2\psi_0 + 3\left(B_0\frac{\mathrm{d}B_0}{\mathrm{d}\psi} - r^2\frac{\mathrm{d}H_0}{\mathrm{d}\psi}\right)\right] \tag{4.18}$$

Consistent with conventional perturbation theory, the leading order reduces to the traditional incompressible Bragg-Hawthorne equation. The first-order correction, however, contains the $O(M_0^2)$ compressible contribution. At first order, its left-hand side mirrors the leading-order operator while the terms on the right-hand side give rise to a non-homogeneous partial differential equation (PDE).

The same procedure may be straightforwardly applied to the stagnation enthalpy in (3.66). We find

$$(1 + M_0^2\rho_1 + M_0^4\rho_2)^2\left[(H_0 + M_0^2H_1 + M_0^4H_2) - \frac{(B_0 + M_0^2B_1 + M_0^4B_2)^2}{2r^2}\right] = \frac{1}{2r^2}\left\{\left[\frac{\partial(\psi_0 + M_0^2\psi_1 + M_0^4\psi_2)}{\partial z}\right]^2 + \left[\frac{\partial(\psi_0 + M_0^2\psi_1 + M_0^4\psi_2)}{\partial r}\right]^2\right\} + \frac{1}{M_0^2\,(\gamma-1)}(1 + M_0^2\rho_1 + M_0^4\rho_2)^{\gamma+1} \tag{4.19}$$

As usual, by segregating terms of the same order, one recovers

$$O(1) : H_0 - \frac{B_0^2}{2r^2} = \frac{1}{2r^2}\left[\left(\frac{\partial\psi_0}{\partial r}\right)^2 + \left(\frac{\partial\psi_0}{\partial z}\right)^2\right] + \frac{\gamma+1}{\gamma-1}\rho_1 \tag{4.20}$$

$$O(M_0^2) : 2\rho_1\left(H_0 - \frac{B_0}{2r^2}\right) + H_1 - \frac{B_0B_1}{2r^2} = \frac{1}{2r^2}\left[\frac{\partial\psi_0}{\partial r}\frac{\partial\psi_1}{\partial r} + \frac{\partial\psi_0}{\partial z}\frac{\partial\psi_1}{\partial z}\right] + \frac{\gamma+1}{\gamma-1}\left(\rho_2 + \gamma\rho_1^2\right) \tag{4.21}$$

When (4.17) is used to solve for ψ_0, substitution into (4.20) directly unravels the density correction, ρ_1. With the density in hand, the right-hand side of (4.18) is

fully determined and the resulting non-homogeneous PDE may be solved for the first compressible stream function correction. In principle, this sequence may be repeated until a satisfactory truncation error is reached. In practice, the procedure will enable us to extract closed-form expressions for the leading and first-order corrections. However, it should be remarked that the solution complexity grows rapidly to the extent that a compressible approximation at the second order or beyond may require considerable effort. Nonetheless, in view of the typical size of M_0^2, the first-order compressible correction will be sufficiently accurate to convey the bulk compressibility effects. This is especially true for swirl-dominated flows such as those arising in the context of a bidirectional vortex engine in which the reference Mach number remains smaller than unity.

4.2 Selecting B and H

Modeling the bidirectional vortex, or any other motion for that matter, begins with the selection of suitable forms for B and H. To facilitate analytical closure, several test functions may be considered, specifically

$$B\frac{\mathrm{d}B}{\mathrm{d}\psi} = \text{constant} \qquad B = \sqrt{B_0\psi + B_1} \tag{4.22}$$

$$B\frac{\mathrm{d}B}{\mathrm{d}\psi} = \psi \qquad B = \sqrt{B_0\psi^2 + B_1} \tag{4.23}$$

$$\frac{\mathrm{d}H}{\mathrm{d}\psi} = \text{constant} \qquad H = H_0\psi + H_1 \tag{4.24}$$

$$\frac{\mathrm{d}H}{\mathrm{d}\psi} = \psi \qquad H = H_0\psi^2 + H_1 \tag{4.25}$$

Although the number of candidate functions may be limitless, the selections above lead to linear relations that increase the likelihood of producing explicit analytical formulations. Higher-order polynomial relations may require a numerical treatment of the density-stream function equations. For example, the (original) incompressible model of the bidirectional vortex by Vyas and Majdalani (2006) may be recovered

by setting $B = 1$ and $\mathrm{d}H/\mathrm{d}\psi = -C_n^2\psi$, where C_n is a constant. To make further headway in illustrating this procedure, one may attempt to follow Bloor and Ingham (1987) or Majdalani (2009) by specifying B and H such that

$$\frac{\mathrm{d}H}{\mathrm{d}\psi} = 0; \quad B = \sqrt{B_0^2\psi^2 + B_1^2}; \quad \frac{\mathrm{d}B}{\mathrm{d}\psi} = \frac{2B_0^2\psi}{2\sqrt{B_0^2\psi^2 + B_1^2}} \tag{4.26}$$

Interestingly, it turns out that, in the compressible case, these declarations prove insufficient to reproduce a congruent first-order system. The source of this disparity may be traced back to the right-hand side of (4.18) where third-order multiples of the stream function emerge. As per (4.20), the density correction contains ψ_0^2 terms, and these are multiplied by another ψ_0 during final book-keeping. To compensate for these additional powers of ψ during the application of the boundary conditions, a modification of (4.26) is warranted. This may be accomplished by taking

$$\begin{aligned} \frac{\mathrm{d}H}{\mathrm{d}\psi} = 0; \quad B &= \sqrt{B_0^2\psi^2 + B_1^2 + M_0^2\left(B_2^2\psi^2 + \tfrac{1}{2}B_3^2\psi^4\right)}; \\ \frac{\mathrm{d}B}{\mathrm{d}\psi} &= \frac{B_0^2\psi + M_0^2\left(B_2^2\psi + B_3^2\psi^3\right)}{\sqrt{B_0^2\psi^2 + B_1^2 + M_0^2\left(B_2^2\psi^2 + \tfrac{1}{2}B_3^2\psi^4\right)}} \end{aligned} \tag{4.27}$$

It may be instructive to remark that the reference Mach number, M_0, remains invariant under steady-state flow conditions. At the outset, its inclusion in the fundamental definition of B does not violate in any way the stream function constraint. Furthermore, realizing that B and $\mathrm{d}B/\mathrm{d}\psi$ appear only as a product, their combined contribution may be expanded as:

$$B\frac{\mathrm{d}B}{\mathrm{d}\psi} = B_0^2\psi + M_0^2\left(B_2^2\psi + B_3^2\psi^3\right) \tag{4.28}$$

From an asymptotic standpoint, (4.28) does not entail a loss of generality. It is obtained by expanding the angular momentum and its derivative to the appropriate truncation order before substituting the outcome into the stream function relation.

The next step is to insert the perturbed form of ψ and write:

$$B\frac{\mathrm{d}B}{\mathrm{d}\psi} = B_0^2\left(\psi_0 + M_0^2\psi_1 + M_0^4\psi^2\right) + M_0^2\left[B_2^2\left(\psi_0 + M_0^2\psi_1 + M_0^4\psi^2\right) + B_3^2\left(\psi_0 + M_0^2\psi_1 + M_0^4\psi^2\right)^3\right] \quad (4.29)$$

4.3 Bragg-Hawthorne Framework

By gathering $O(M_0^2)$ in $B\,\mathrm{d}B/\mathrm{d}\psi$, one retrieves

$$B\frac{\mathrm{d}B}{\mathrm{d}\psi} = B_0^2\psi_0 + M_0^2\left(B_0^2\psi_1 + B_2^2\psi_0 + B_3^2\psi_0^3\right) + O(M_0^4) \quad (4.30)$$

Inserting these contributions back into (4.17) and (4.18) gives rise to a congruent set of linearized Bragg-Hawthorne equations at the first two successive perturbation orders, namely,

$$O(1) : D^2\psi_0 + B_0^2\psi_0 = 0 \quad (4.31)$$

$$O(M_0^2) : D^2\psi_1 + B_0\psi_1 = \frac{\partial\rho_1}{\partial z}\frac{\partial\psi_0}{\partial z} + \frac{\partial\rho_1}{\partial r}\frac{\partial\psi_0}{\partial r} - \rho_1\left(D^2\psi_0 + 3B_0^2\psi_0\right) - B_2^2\psi_0 - B_3^2\psi_0^3 \quad (4.32)$$

Equation (4.32) can be further simplified by realizing that the left-hand side of (4.31) partially appears on its right-hand side. This permits reducing (4.32) into

$$D^2\psi_1 + B_0\psi_1 = \frac{\partial\rho_1}{\partial z}\frac{\partial\psi_0}{\partial z} + \frac{\partial\rho_1}{\partial r}\frac{\partial\psi_0}{\partial r} - 2\rho_1 B_0^2\psi_0 - B_2^2\psi_0 - B_3^2\psi_0^3 \quad (4.33)$$

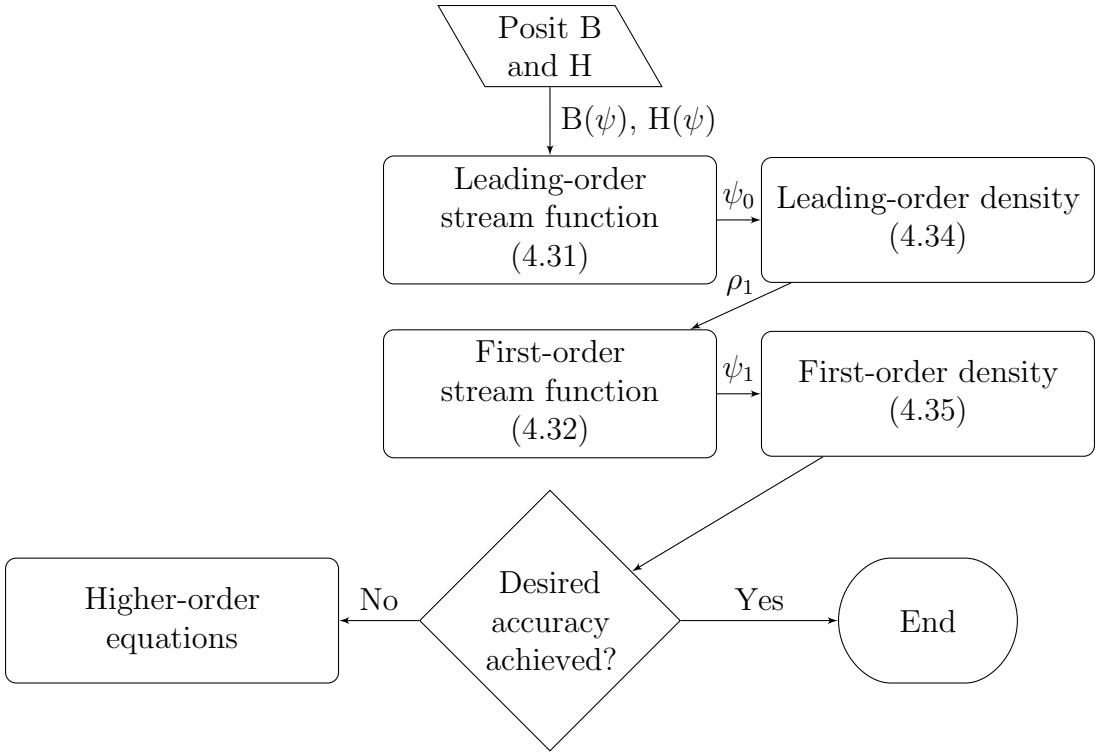

Figure 4.1: Flowchart for the density-stream function formulation needed to obtain a compressible Bragg-Hawthorne solution.

Similar substitutions may be implemented in the density relation to unravel

$$O(1): \frac{\gamma+1}{\gamma-1}\rho_1 = -\frac{1}{2r^2}\left[\left(\frac{\partial\psi_0}{\partial r}\right)^2 + \left(\frac{\partial\psi_0}{\partial z}\right)^2 + B_0^2\psi_0^2\right] \tag{4.34}$$

$$\begin{aligned} O(M_0^2): \frac{\gamma+1}{\gamma-1}\left(\rho_2 + \gamma\rho_1^2\right) &= -\frac{B_0^2\psi_0}{r^2}\left(\psi_0\rho_1 + \psi_1\right) \\ &\quad - \frac{1}{2r^2}\left[\frac{\partial\psi_0}{\partial r}\frac{\partial\psi_1}{\partial r} + \frac{\partial\psi_0}{\partial z}\frac{\partial\psi_1}{\partial z} + B_2^2\psi_0^2 + B_3^2\psi_0^4\right] \end{aligned} \tag{4.35}$$

In seeking a compressible mean flow approximation, the procedure consists of solving (4.31), (4.34), (4.32), and (4.35) in this staggered sequence. A flowchart describing this process is given as Figure 4.1. In Chapter 5, the bidirectional vortex flow field will be used as a test case.

4.4 Expanded VS Equations

The vorticity-stream function model may be expanded in a similar manner to that presented in Section 4.1. Beginning with the vorticity transport equation, one has

$$\nabla \times \left[(\boldsymbol{U}_0 + M_0^2\boldsymbol{U_1}) \times (\boldsymbol{\Omega}_0 + M_0^2\boldsymbol{\Omega}_1)\right] = \frac{1}{\gamma M_0^2(1 + M_0^2\rho_1 + M_0^4\rho_2)^2}\nabla(1 + M_0^2\rho_1 + M_0^4\rho_2) \cdot \nabla(1 + M_0^2 p_1 + M_0^4 p_2) \quad (4.36)$$

After collecting like orders of M_0, (4.36) may be written as the following pair of equations

$$O(1) : \nabla \times (\boldsymbol{U}_0 \times \boldsymbol{\Omega}_0) = 0 \quad (4.37)$$

$$O(M_0^2) : \nabla \times (\boldsymbol{U}_0 \times \boldsymbol{\Omega}_1) + \nabla \times (\boldsymbol{U}_1 \times \boldsymbol{\Omega}_0) = -\frac{\nabla\rho_1 \times \nabla p_1}{\gamma} \quad (4.38)$$

Then the stream function may be expanded as

$$\mathrm{D}^2(\psi_0 + M_0^2\psi_1) + r(1 + M_0^2\rho_1 + M_0^4\rho_2)(\Omega_0 + M_0^2\Omega_1) = \frac{1}{1 + M_0^2\rho_1 + M_0^4\rho_2}\nabla(1 + M_0^2\rho_1 + M_0^4\rho_2) \cdot \nabla(\psi_0 + M_0^2\psi_1) \quad (4.39)$$

As before, (4.39) may be segregated into

$$O(1) : \mathrm{D}^2\psi_0 + r\Omega_0 = 0 \quad (4.40)$$

$$O(M_0^2) : \mathrm{D}^2\psi_1 + r\Omega_1 = \nabla\rho_1 \cdot \nabla\psi_0 - r\Omega_0\rho_1 \quad (4.41)$$

Unlike the Bragg-Hawthorne framework, the vorticity-stream function approach requires expansion of the conservation of momentum, (3.17), which may be manipulated to yield

$$(\boldsymbol{U}_0 + M_0^2\boldsymbol{U_1}) \cdot \nabla(\boldsymbol{U}_0 + M_0^2\boldsymbol{U_1}) = -\frac{\nabla(1 + M_0^2 p_1 + M_0^4 p_2)}{\gamma M^2(1 + M_0^2\rho_1 + M_0^4\rho_2)} \quad (4.42)$$

When separating the leading and first-order equations, it is also beneficial to expand the general vector relations into their scalar components. The segregated radial momentum equation becomes

$$O(M_0^2) : -\frac{1}{\gamma}\frac{\partial p_1}{\partial r} = u_0\frac{\partial u_0}{\partial r} + w_0\frac{\partial u_0}{\partial z} - \frac{v_0^2}{r} \tag{4.43}$$

$$O(M_0^4) : -\frac{1}{\gamma}\frac{\partial p_2}{\partial r} = \rho_1\left(u_0\frac{\partial u_0}{\partial r} + w_0\frac{\partial u_0}{\partial z} - \frac{v_0^2}{r}\right) + \frac{\partial(u_0u_1)}{\partial r} + w_0\frac{\partial u_1}{\partial z} + w_1\frac{\partial u_0}{\partial z} \tag{4.44}$$

The corresponding axial momentum relation may be retrieved as

$$O(M_0^2) : -\frac{1}{\gamma}\frac{\partial p_1}{\partial z} = w_0\frac{\partial w_0}{\partial z} + u_0\frac{\partial w_0}{\partial r} \tag{4.45}$$

$$O(M_0^4) : -\frac{1}{\gamma}\frac{\partial p_2}{\partial z} = \rho_1\left(w_0\frac{\partial w_0}{\partial z} + u_0\frac{\partial w_0}{\partial r}\right) + \frac{\partial(w_0w_1)}{\partial z} + u_0\frac{\partial w_1}{\partial r} + u_1\frac{\partial w_0}{\partial r} \tag{4.46}$$

In order to assess the compressible correction in (4.41) the density must be determined. Because the framework employs an isentropic assumption, the thermodynamic variables may be connected through

$$O(M_0^2) : \rho_1 = \frac{p_1}{\gamma} \tag{4.47}$$

$$O(M_0^4) : \rho_2 = \frac{p_2}{\gamma} + \frac{1-\gamma}{2\gamma^2}p_1^2 \tag{4.48}$$

and

$$O(M_0^2) : T_1 = \frac{\gamma-1}{\gamma}p_1 \tag{4.49}$$

$$O(M_0^4) : T_2 = \frac{\gamma-1}{\gamma}p_2 + \frac{\gamma-1}{2\gamma^2}p_1^2 \tag{4.50}$$

The solution algorithm for this system varies from the one outlined in Figure 4.1. For the vorticity-stream function approach, the vorticity transport equation is first solved to connect the vorticity to the stream function. This definition is then substituted into the stream function to provide a solvable relation. After the stream

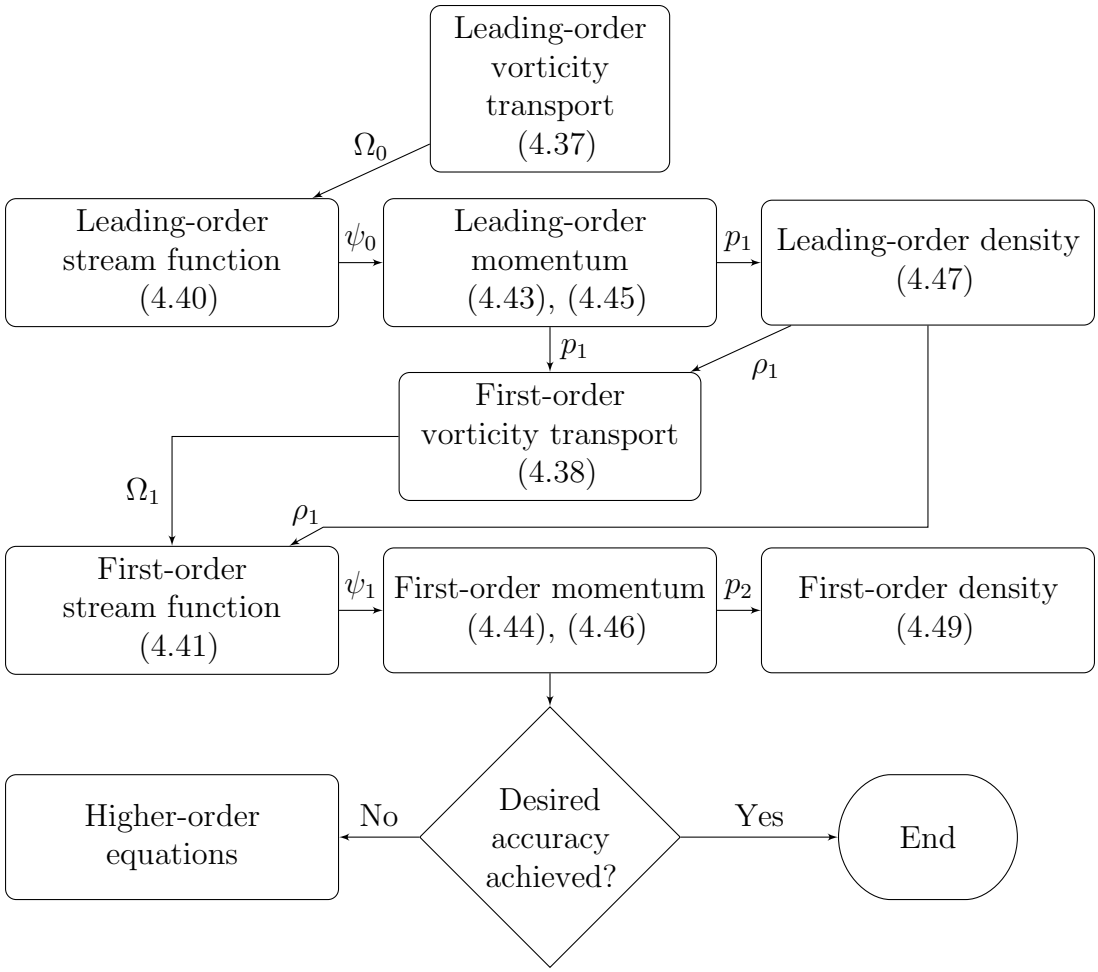

Figure 4.2: Flowchart for the methodology needed to obtain a compressible vorticity-stream function solution.

function is known, the axial and radial momentum relations are solved to determine the pressure distribution at that order. The isentropic equations are then used to deduce the remaining thermodynamic variables. If the solution requires additional accuracy, then the process is repeated at the next highest order. The method is depicted graphically in Figure 4.2.

Chapter 5

Perturbation Solution

In this chapter, the perturbation solutions for the Bragg-Hawthorne and vorticity-stream function frameworks are presented. The solutions are solved via the methodology introduced in Figures 4.1 and 4.2, respectively. In both cases, the leading-order is known as they reproduce the incompressible studies. For the sake of completeness the leading-order for each model is presented in its entirety. Compressibility effects are introduced at the first order, and as such it is sometimes referred to as the compressible correction. For values relevant to propulsive applications, a single correction will invariably capture the bulk of the high speed effects; as such, higher order corrections are rarely needed.

5.1 Perturbed Bragg-Hawthorne Solution

5.1.1 Leading-Order CBH General Solution

The leading-order stream function must be consistent with the incompressible solution for the same problem. In this spirit, (4.31) may be treated with separation of variables (Majdalani, 2009). Assuming $\psi_0 = f(r)g(z)$, (4.31) becomes

$$-\frac{g''}{g} = \frac{1}{f}\left(f'' - \frac{1}{r}f' + B_0^2 f\right) = \nu^2 \tag{5.1}$$

where ν^2 can be positive, negative or zero. Depending on the value chosen for ν^2, three possibilities may be conceived, namely,

$$\psi_0 = \begin{cases} r\left(C_1 z + C_2\right)\left[C_3 J_1(B_0 r) + C_4 Y_1(B_0 r)\right]; & \nu^2 = 0 \\ r\left[C_1 \sin(\nu z) + C_2 \cos(\nu z)\right] & \\ \qquad \times \left[C_3 J_1(r\sqrt{B_0^2 - \nu^2}) + C_4 Y_1(r\sqrt{B_0^2 - \nu^2})\right]; & B_0^2 > \nu^2 \\ r\left[C_1 \sinh(\nu z) + C_2 \cosh(\nu z)\right] & \\ \qquad \times \left[C_3 J_1(r\sqrt{B_0^2 + \nu^2}) + C_4 Y_1(r\sqrt{B_0^2 + \nu^2})\right]; & B_0^2 < \nu^2 \end{cases} \tag{5.2}$$

In reality, the last two variations prove to be equivalent as one can be reproduced from the other by simply replacing ν with $\pm i\nu$. When accounting for the imaginary part, the hyperbolic functions reduce to their regular trigonometric counterparts and the Bessel function arguments become identical as the imaginary ν^2 switches its sign. For brevity, the axially linear case is provided as a vehicle for developing a compressible approximation.

5.1.2 Leading-Order CBH Boundary Conditions

To satisfy the centerline boundary conditions for all values of z, one sets $C_4 = 0$ everywhere. Furthermore, applying (4.8) leads to

$$\frac{\partial \psi_0(r,0)}{\partial r} = C_2 B_0 C_3 J_0(B_0 r) = 0 \tag{5.3}$$

Since equating either C_3 or B_0 to zero leads to a trivial outcome, one must take $C_2 = 0$. Substituting the resultant stream function back into the sidewall boundary condition produces

$$\frac{\partial \psi_0(1,z)}{\partial z} = C_3 J_1(B_0) \times \begin{cases} C_1; & \nu^2 = 0 \\ C_1 \nu \cos(\nu z); & \nu^2 \neq 0 \end{cases} \tag{5.4}$$

For (5.4) to be true $\forall z$, B_0 must be a root of the Bessel function of the first kind, or

$$B_0 = \lambda_n; n = 1, 2, \ldots \tag{5.5}$$

Increments in n will effectively trigger an increasing number of axial reversals in the flow, specifically n reversals. In practice, only an odd number of reversals will be applicable and so, to recover the standard bidirectional vortex model (Majdalani, 2009), the analysis is restricted to the $n = 1$ case.

At this juncture, the only remaining term is the lumped constant C_1C_3 that must be determined by matching the inflow and outflow mass fluxes. At the leading order, this may be written as

$$2\pi \int_0^\beta \boldsymbol{u} \cdot \boldsymbol{n}\, r\, \mathrm{d}r = 2\pi \int_0^\beta w(r, L)\, r\, \mathrm{d}r = Q_i \tag{5.6}$$

From the mass balance in (5.6) one deduces

$$C_1C_3 \equiv \kappa = \frac{Q_i}{2\pi\beta L J_1(\lambda_0\beta)} \tag{5.7}$$

The parameter κ is essentially an off-swirl parameter, sometimes called the inflow parameter. Large values of κ imply a weakly swirling flow. For the bidirectional vortex application, values of κ are in the range of 0.1 to 0.001. This leaves the final stream function form as

$$\psi_0 = \kappa r J_1(\lambda_0 r) \times \begin{cases} z; & \nu^2 = 0 \\ \sin(\nu z); & \nu^2 \neq 0 \end{cases} \tag{5.8}$$

As to be expected from a leading-order asymptotic approximation, (5.8) reproduces the incompressible Beltramian solutions obtained by Majdalani (2009) in a right-cylindrical cyclone. With the stream function being fully determined, the density may be retrieved from (4.34) following a straightforward substitution. After some

simplifications, the density may be extracted as:

$$\rho_1 = -\frac{A_0^2(\gamma-1)}{2(\gamma+1)}\left\{J_1^2(r\lambda_0) + z^2\lambda_0^2\left[J_0^2(r\lambda_0) + J_1^2(r\lambda_0)\right]\right\} \tag{5.9}$$

Equation (5.9) is quite illuminating. In fact, it confirms the need for higher powers of ψ within the fundamental definition of B in (4.27). Clearly, Bessel functions that are elevated to the second power appear thrice in the density. These, in turn, multiply a single Bessel function in (4.32), the first-order stream function relation. In seeking appropriate candidate functions for the particular solution, terms that may be expressed in multiples of three Bessel functions must be attempted. This step is prompted by the requirement to write B in terms of ψ at the basis of the Bragg-Hawthorne procedure.

5.1.3 First-Order CBH General Solution

The first-order correction follows a similar roadmap, albeit with increased complexity. Instead of a homogeneous equation, a particular solution must be determined in such a way to accommodate the terms appearing on the right-hand side of (4.32). For the spatially linear case, suitable substitutions of ψ_0 and ρ_1 lead to the first-order, compressible Bragg-Hawthorne equation, namely,

$$\begin{aligned} D^2\psi_1 + B_0^2\psi_1 = \frac{\gamma-1}{\gamma+1}A_0^3\lambda_0 z J_1(r\lambda_0)\big(&J_0(r\lambda_0)J_1(r\lambda_0) - 2\lambda_0 r J_0^2(r\lambda_0) \\ &+z^2\lambda_0^2\left\{J_0(r\lambda_0)J_1(r\lambda_0) + r\lambda_0\left[J_0^2(r\lambda_0) + J_1^2(r\lambda_0)\right]\right\}\big) \\ &- B_2 A_0 r z J_1(r\lambda_0) - B_3 A_0^3 r^3 z^3 J_1^3(r\lambda_0) \end{aligned} \tag{5.10}$$

Rather than a standard separation of variables approach, an ansatz is employed that is guided by the non-homogeneous terms. Recognizing that both z and z^3 appear in (5.10), ψ_1 becomes

$$\psi_1 = zR_a + z^3R_b \tag{5.11}$$

By virtue of (5.11), the single PDE gives rise to two ODEs that may be written as

$$z^3: \; R_b'' - \frac{1}{r}R_b' + \lambda_0^2 R_b = \frac{\gamma-1}{\gamma+1}A_0^3\lambda_0^3 J_1(r\lambda_0)\left\{J_0(r\lambda_0)J_1(r\lambda_0) + r\lambda_0\left[J_0^2(r\lambda_0) + J_1^2(r\lambda_0)\right]\right\} - B_3 A_0^3 r^3 J_1^3(r\lambda_0) \quad (5.12)$$

and

$$z: \; R_a'' - \frac{1}{r}R_a' + \lambda_0^2 R_a + 6R_b = \frac{\gamma-1}{\gamma+1}A_0^3\lambda_0 J_1(r\lambda_0)\left[J_0(r\lambda_0)J_1(r\lambda_0) - 2\lambda_0 r J_1(r\lambda_0)\right] - B_2 A_0 r J_1(r\lambda_0) \quad (5.13)$$

Our next step is to first solve (5.12), being a sole function of R_b. The ensuing solution may be then substituted back into (5.13) to produce R_a, and with it, a complete compressible correction.

The solution to (5.12) is exacerbated by its dependence on J_0^3 and J_1^3 terms. While Bessel function integrals remain straightforward to evaluate in closed form, integrals for multiplicative Bessel functions can be elusive. In lieu of a completely analytical closure, the correction becomes limited to a semi-analytical expression that requires the numerical evaluation of a handful of integrals. To overcome this difficulty, the integrals themselves will be isolated and specified as functions that may be differentiated or integrated at will, so that the boundary conditions can still be determined analytically. In essence, these new integrals may be viewed as special functions that enable us to retain the analytical character of the formulation. After

some effort, the z^3 multiplier is found to be

$$\begin{aligned} R_b = rJ_1(r\lambda_0)\Bigg[\frac{\pi}{2}A_0^3\Bigg(\frac{\gamma-1}{\gamma+1}\lambda_0^3\int_1^r J_1(\lambda_0 r_1)\,Y_1(\lambda_0 r_1) \\ \times\left\{-\lambda_0 r_1\left[J_0^2(\lambda_0 r_1)+J_1^2(\lambda_0 r_1)\right]-J_0(\lambda_0 r_1)\,J_1(\lambda_0 r_1)\right\}\mathrm{d}r_1 \\ +B_3\int_1^r r_1^3 J_1^3(\lambda_0 r_1)\,Y_1(\lambda_0 r_1)\,\mathrm{d}r_1\Bigg)+A_{1a}\Bigg] \\ +rY_1(r\lambda_0)\Bigg[\frac{\pi}{2}A_0^3\Bigg(\frac{\gamma-1}{\gamma+1}\lambda_0^3\int_1^r J_1^2(\lambda_0 r_2) \\ \times\left\{J_0(\lambda_0 r_2)\,J_1(\lambda_0 r_2)+\lambda_0 r_2\left[J_0^2(\lambda_0 r_2)+J_1^2(\lambda_0 r_2)\right]\right\}\mathrm{d}r_2 \\ +B_3\int_1^r -r_2^3 J_1^4(\lambda_0 r_2)\,\mathrm{d}r_2\Bigg)+A_{1b}\Bigg] \end{aligned} \tag{5.14}$$

Here A_{1a} and A_{1b} are integration constants while r_1 and r_2 represent variable substitutions in the radial integrals. In treating the integrals as functions, (5.14) may be re-written as

$$\begin{aligned} R_b = rJ_1(r\lambda_0)\left[\frac{\pi}{2}A_0^3\left(\frac{\gamma-1}{\gamma+1}\lambda_0^3\mathcal{I}_1+B_3\mathcal{I}_2\right)+A_{1a}\right] \\ +rY_1(r\lambda_0)\left[\frac{\pi}{2}A_0^3\left(\frac{\gamma-1}{\gamma+1}\lambda_0^3\mathcal{I}_3+B_3\mathcal{I}_4\right)+A_{1b}\right] \end{aligned} \tag{5.15}$$

where $\mathcal{I}_n$ represents the n$^{\text{th}}$ integral in the first-order relation. For the reader's convenience, these are defined in Appendix A.

The z multiplier may be obtained along similar lines. Inserting (5.15) into (5.13) yields

$$\begin{aligned} R_a = rJ_1(r\lambda_0)\Bigg[\frac{\pi}{2}A_0\Bigg(\frac{\gamma-1}{\gamma+1}A_0^2\lambda_0\int_1^r J_1(\lambda_0 r_1)\,Y_1(\lambda_0 r_1) \\ \times\left\{2\lambda_0 r_1 J_0^2(\lambda_0 r_1) - J_0(\lambda_0 r_1)\,J_1(\lambda_0 r_1)\right\}\mathrm{d}r_1 \\ +B_2\int_1^r r_1 J_1(\lambda_0 r_1)\,Y_1(\lambda_0 r_1)\,\mathrm{d}r_1\Bigg) + 3\pi\int_1^r Y_1(\lambda_0 r_1)\,R_b(r_1)\mathrm{d}r_1 + A_{1c}\Bigg] \\ + rY_1(r\lambda_0)\Bigg[\frac{\pi}{2}A_0\Bigg(\frac{\gamma-1}{\gamma+1}A_0^2\lambda_0\int_1^r J_1^2(\lambda_0 r_2) \\ \times\left\{J_0(\lambda_0 r_2)\,J_1(\lambda_0 r_2) - 2\lambda_0 r_2 J_0^2(\lambda_0 r_2)\right\}\mathrm{d}r_2 + B_2\int_1^r -r_2 J_1^2(\lambda_0 r_2)\,\mathrm{d}r_2\Bigg) \\ -3\pi\int_1^r J_1(\lambda_0 r_2)\,R_b(r_2)\mathrm{d}r_2 + A_{1d}\Bigg] \end{aligned} \tag{5.16}$$

Here too, the same notation for the special integrals may be used to turn (5.16) into

$$\begin{aligned} R_a = rJ_1(r\lambda_0)\left[\frac{\pi}{2}A_0\left(\frac{\gamma-1}{\gamma+1}A_0^2\lambda_0\mathcal{I}_5 + B_2\mathcal{I}_6\right) + 3\pi\mathcal{I}_7 + A_{1c}\right] \\ + rY_1(r\lambda_0)\left[\frac{\pi}{2}A_0\left(\frac{\gamma-1}{\gamma+1}A_0^2\lambda_0\mathcal{I}_8 + B_2\mathcal{I}_9\right) - 3\pi\mathcal{I}_{10} + A_{1d}\right] \end{aligned} \tag{5.17}$$

By substituting (5.15) and (5.17) back into (5.11), one arrives at the general compressible correction. What remains to be established is a coherent set of boundary conditions and this aspect will be discussed next.

5.1.4 First-Order CBH Boundary Conditions

Compared to the leading order, the boundary conditions at the first order change slightly. In fact, ensuring that the compressible correction does not unduly influence the solution warrants homogeneous constraints. Because the boundary conditions are written in terms of the velocity, it is useful to revisit the expanded velocity-stream

function relationship. At the first order, the velocities can be written as

$$u_1 = \frac{\rho_1}{r}\frac{\partial \psi_0}{\partial z} - \frac{1}{r}\frac{\partial \psi_1}{\partial z} \tag{5.18}$$

$$w_1 = \frac{1}{r}\frac{\partial \psi_1}{\partial r} - \frac{\rho_1}{r}\frac{\partial \psi_0}{\partial r} \tag{5.19}$$

To avoid lengthy stream function expressions, the general expansion of (5.18) and (5.19) are omitted. Instead, each boundary condition is examined individually. For the centerline condition, one has

$$\begin{aligned} u_1(0,z) = -3z^2 Y_1(0)\left\{\frac{\pi}{2}\kappa^3\left[\frac{\gamma-1}{\gamma+1}\lambda_0^3\mathcal{I}_3(0) + B_3\mathcal{I}_4(0)\right] + A_{1b}\right\} \\ + Y_1(0)\left[\frac{\pi}{2}\frac{\gamma-1}{\gamma+1}\kappa^3\lambda_0\mathcal{I}_8(0) + \frac{\pi}{2}\kappa B_2\mathcal{I}_9(0) - 3\pi\mathcal{I}_{10}(0) + A_{1d}\right] = 0 \end{aligned} \tag{5.20}$$

In actuality, (5.20) gives rise to two distinct equalities that are needed to permit the radial velocity to vanish for all values of z. To this end, coefficients multiplying z^2 and those of $O(1)$ must vanish independently. For the z^2 terms, the following is recovered

$$\frac{\pi}{2}A_0^3\left[\frac{\gamma-1}{\gamma+1}\lambda_0^3\mathcal{I}_3(0) + B_3\mathcal{I}_4(0)\right] + A_{1b} = 0 \tag{5.21}$$

and, for the z^0 coefficient,

$$\frac{\pi}{2}\frac{\gamma-1}{\gamma+1}A_0^3\lambda_0\mathcal{I}_8(0) + \frac{\pi}{2}A_0B_2\mathcal{I}_9(0) - 3\pi\mathcal{I}_{10}(0) + A_{1d} = 0 \tag{5.22}$$

The sidewall boundary condition also separates into a pair of constraints. The resulting relation for the z^2 expression becomes

$$\frac{\pi}{2}A_0^3\left[\frac{\gamma-1}{\gamma+1}\lambda_0^3\mathcal{I}_3(1) + B_3\mathcal{I}_4(1)\right] + A_{1b} = 0 \tag{5.23}$$

and, similarly, at $O(1)$ one retrieves

$$\frac{\pi}{2}\frac{\gamma-1}{\gamma+1}A_0^3\lambda_0\mathcal{I}_8(1)+\frac{\pi}{2}A_0B_2\mathcal{I}_9(1)-3\pi\mathcal{I}_{10}(1)+A_{1d}=0 \tag{5.24}$$

Realizing that the integrals $\mathcal{I}_8(1)$, $\mathcal{I}_9(0)$, $\mathcal{I}_3(1)$, and $\mathcal{I}_4(1)$ vanish identically, A_{1b} and A_{1c} may be fully determined from

$$A_{1b}=0;\ A_{1d}=3\pi\mathcal{I}_{10}(0)-\frac{\pi}{2}\frac{\gamma-1}{\gamma+1}\kappa^3\lambda_0\mathcal{I}_8(0) \tag{5.25}$$

With A_{1b} and A_{1d} in hand, the B_2 and B_3 constants may be deduced from (5.21) and (5.22). The resulting constants return

$$B_2=\frac{2\left[3\pi\mathcal{I}_{10}(1)-A_{1d}\right]}{\pi\kappa\mathcal{I}_9(1)} \tag{5.26}$$

$$B_3=-\lambda_0^3\frac{\gamma-1}{\gamma+1}\frac{\mathcal{I}_3(0)}{\mathcal{I}_4(0)} \tag{5.27}$$

Finally, the expanded mass balance condition may be expressed as

$$2\pi\int_0^\beta\left[\rho_1w_0(r,L)+w_1(r,L)\right]\ r\ \mathrm{d}r=0 \tag{5.28}$$

The detailed form of the above expression is prohibitively long and, as such, of minimal interest to the reader. However, the remaining integral may be easily handled using symbolic programming. The evaluation of (5.28) completes the first-order analysis from which all other flow parameters may be derived.

5.2 Perturbed VS Solution

5.2.1 Leading-Order VS Solution

As previously mentioned, the leading-order reproduces the incompressible solution of Vyas and Majdalani (2006) and Majdalani and Chiaverini (2009). The leading-order

vorticity transport equation, (4.37) can be coupled with the stream function definitions in (3.27) to relate the vorticity to the stream function. The expanded equation may be written as

$$-\frac{\partial\psi_0}{\partial z}\frac{\partial}{\partial r}\left(\frac{\Omega_0}{r}\right)+\frac{\partial\psi_0}{\partial r}\frac{\partial}{\partial z}\left(\frac{\Omega_0}{r}\right)=0 \tag{5.29}$$

It may be readily verified that the above will be satisfied if the vorticity is written in the form

$$\Omega_0 = rF[\psi_0(r,z)] \tag{5.30}$$

Here F is an arbitrary function of the stream function. While the potential candidates using this arbitrary definition are infinite, in practice it is difficult to solve the resulting formulations unless a linear behavior is implied. In that vein, the vorticity may be taken as

$$\Omega_0 = C^2 r\psi_0 \tag{5.31}$$

With (5.31) in hand, it is now possible to write (4.40) solely in terms of the stream function. The resulting expression reduces to

$$\mathrm{D}^2\psi_0 + C^2r^2\psi_0 = 0 \tag{5.32}$$

Equation (5.32) may be solved via multiplicative separation of variables. By setting, $\psi_0 = f(r)g(z)$ one retrieves

$$-\frac{1}{g}\frac{\mathrm{d}^2 g}{\mathrm{d}z^2} = \frac{1}{f}\left(\frac{\mathrm{d}^2 f}{\mathrm{d}r^2}-\frac{1}{r}\frac{\mathrm{d}f}{\mathrm{d}r}+C^2r^2 f\right) = \pm\lambda^2 \tag{5.33}$$

As obtained with the Bragg-Hawthorne outcome of Section 5.1.1, the separated equation here produces three solutions corresponding to positive, negative and null separation constants. Unlike the previous framework, only the zero separation constant produces a physically meaningful model. At the leading order, one reaps,

$$\psi_0 = (C_1 z + C_2)\left[C_3\sin\left(\frac{Cr^2}{2}\right)+C_4\cos\left(\frac{Cr^2}{2}\right)\right] \tag{5.34}$$

5.2.2 Leading-Order VS Boundary Conditions

Through the application of the constraints in (4.8), (4.10), (4.12), and (4.14), the general constants may be determined. First, the impervious headwall condition in (4.8) gives

$$w_0(r,0) = C_2 C \left[C_3 \cos\left(\frac{Cr^2}{2}\right) - C_4 \sin\left(\frac{Cr^2}{2}\right) \right] = 0 \tag{5.35}$$

This forces $C_2 = 0$ (setting $C = 0$ is not an option because it removes the radial dependence from the problem, which is not physical). With the first constant determined, the radial centerline condition may be applied viz.

$$u_0(0,z) = -C_1 \left[C_3 \sin(0) + C_4 \cos(0) \right] = 0 \tag{5.36}$$

Since $C_1 = 0$ produces a null solution, the only remaining choice is for $C_4 = 0$. The impervious sidewall condition leaves

$$u_0(1,z) = -C_1 C_3 \sin(\frac{C}{2}) = 0 \tag{5.37}$$

As C_1 or C_3 cannot simultaneously vanish without reducing the expression to a trivial solution, the expression for the separation constant, $C/2$, must contain the zeros of the sine function. The full expression for the separation constant may be expressed as

$$C = 2\pi \tag{5.38}$$

The present description is only concerned with the first zero, $n = 1$, which contains one flow field reversal. In reality, subsequent zeros will increase the number of axial reversals observed in the model. For the bidirectional vortex engine, only odd zeros make practical sense as the flow enters and exits near the base. For even zeros, the flow enters at the base and exits at the head end.

The remaining constants, C_1 and C_3 may be lumped together and then determined from the final boundary condition, the conservation condition on the axial outflow:

$$2\pi C_1 C_3 L \sin(\pi\beta^2) = Q_i \tag{5.39}$$

or

$$\kappa = \frac{Q_i}{2\pi L \sin(\pi\beta^2)} \tag{5.40}$$

The end result is a stream function representation of the bidirectional vortex, namely,

$$\psi_0 = \kappa z \sin(\pi r^2) \tag{5.41}$$

In writing the subsequent expressions, the lumped constant, κ, is retained for the sake of brevity. Using the stream function definitions, the component velocities in the radial and axial directions are

$$u_0 = -\frac{\kappa}{r}\sin(\pi r^2) \tag{5.42}$$

$$w_0 = 2\kappa z \cos(\pi r^2) \tag{5.43}$$

5.2.3 Centerline Swirl Correction

Though the vorticity-stream function model is inviscid, the compressible corrections require a non-singular density near the centerline. To overcome this deficiency, the original work by Vyas and Majdalani (2006) must be augmented by a correction to the swirl velocity. The details of this procedure may be found in Majdalani and Chiaverini (2009), but the relevant correction is reproduced here for the sake of completeness.

When considering the singular behavior of the swirl velocity at the centerline, it is clear that a limiting process must exist to prevent an infinitely large value at $r = 0$. The most physically meaningful phenomenon is to include viscous effects in the core region. To that end, the retention of the viscous terms in the tangential momentum

equation produces

$$u\frac{\partial v}{\partial r}+\frac{uv}{r}=\frac{1}{Re}\frac{\partial}{\partial r}\left[\frac{1}{r}\frac{\partial(rv)}{\partial r}\right] \tag{5.44}$$

This expression assumes an axial independence of the swirl velocity, an observation that has been verified experimentally. For this investigation, values of Re are typically on the order of 10^5, thus the viscous tangential momentum equation can be perturbed in $1/Re$. To simplify (5.44), a change in variable of the form $\xi = rv$ is introduced, simplifying (5.44) to

$$\epsilon\frac{\mathrm{d}}{\mathrm{d}r}\left(\frac{1}{r}\frac{\mathrm{d}\xi}{\mathrm{d}r}\right)-\frac{u}{r}\frac{\mathrm{d}\xi}{\mathrm{d}r}=0 \tag{5.45}$$

A further simplification is possible by introducing $\eta = \pi r^2$ and substituting u from the leading-order stream function such that

$$\frac{\epsilon}{\kappa}\frac{\mathrm{d}^2\xi}{\mathrm{d}\eta}+\frac{\sin\eta}{2\eta}\frac{\mathrm{d}\xi}{\mathrm{d}\eta}=0 \tag{5.46}$$

In keeping with traditional boundary layer theory, a slowly varying scale is introduced as

$$s\equiv\frac{\eta}{\delta(\epsilon)} \tag{5.47}$$

which transforms (5.46) to

$$\frac{\epsilon}{\kappa\delta^2}\frac{\mathrm{d}^2\xi}{\mathrm{d}s}+\frac{\sin(\delta s)}{2\delta^2 s}\frac{\mathrm{d}\xi}{\mathrm{d}s}=0 \tag{5.48}$$

As the boundary layer correction is focused on the near core region, the small angle expansion for the sine term may be employed to further reduce (5.48). Simultaneously, a balance between the convective and diffusive terms is necessary near the core. Such a balance is found when $\delta \sim \epsilon/\kappa$, or,

$$\frac{\mathrm{d}^2\xi^i}{\mathrm{d}s^2}+\frac{1}{2}\frac{\mathrm{d}\xi^i}{\mathrm{d}s}=0 \tag{5.49}$$

where the superscript i denotes the inner solution. At the centerline, the swirl velocity must go to zero and the inner scale must smoothly adapt to the outer, inviscid solution. The resulting one-term approximation to (5.49) takes the form

$$\xi^i = C_0 \exp\left(-\frac{1}{2}s\right) + C_1 \tag{5.50}$$

From the swirl velocity centerline condition, one gets $C_1 = 0$; the remaining constant may be determined from Prandtl's matching principle. After matching and returning to the original laboratory coordinates, the composite solution may be written as

$$v_0 \simeq \frac{1}{r}\left[1 - \exp(-\frac{1}{4}Vr^2)\right] \tag{5.51}$$

Here V is a dimensionless parameter called the vortex Reynolds number. The parameter emerges naturally from the analysis of the core correction and may be defined as

$$V \equiv \frac{1}{\epsilon\sigma l} = \frac{Re}{\sigma}\frac{a}{L} = \frac{\rho U A_i}{\mu L} = \frac{\dot{m}_i}{\mu L} \tag{5.52}$$

Clearly, V behaves much like the traditional Reynolds number with some slight adjustments for the nature of the confined vortex, through the incorporation of the swirl velocity and aspect ratio. This parameter is responsible for the size and shape of the core swirl velocity region. Larger values of V will result in larger swirl velocity maxima, as well as moving the core region closer to the centerline of the chamber. In Section 6.2, V forms the basis of the correlations of the piecewise swirl velocity model with the preceding solution as well as with experiment.

5.2.4 Leading-Order VS Thermodynamics

Before advancing to the first order, the pressure and density must be determined from the momentum and isentropic relations. To this end, the radial and axial momentum equations may be integrated independently and then carefully combined to provide the complete pressure, after removing overlapping parts. For the radial pressure gradient,

one gets

$$\frac{1}{\gamma}\frac{\partial p_1}{\partial r} = \frac{\kappa}{r}\sin(\pi r^2)\left[2\pi\kappa\cos(\pi r^2) - \frac{1}{r^2}\sin(\pi r^2)\right] + \frac{\left[1-\exp(-\frac{1}{4}Vr^2)\right]^2}{r^3} \tag{5.53}$$

Similarly, the axial equation returns

$$-\frac{1}{\gamma}\frac{\partial p_1}{\partial z} = 4\kappa^2 z \tag{5.54}$$

The combined solution to (5.53) and (5.54) may be expressed as

$$\begin{aligned} p_1 = &-2(\pi\kappa z)^2\gamma \\ &+\frac{\gamma}{4}\left\{2 - 2r^{-2}\left[1+\exp\left(-\frac{1}{2}Vr^2\right) - 2\exp\left(\frac{1}{4}Vr^2\right) + \kappa\sin^2(\pi r^2)\right]\right. \\ &\left.+V\left[\mathrm{Ei}\left(-\frac{1}{2}V\right) - \mathrm{Ei}\left(-\frac{1}{4}V\right) + \mathrm{Ei}\left(-\frac{1}{4}Vr^2\right) - \mathrm{Ei}\left(-\frac{1}{2}Vr^2\right)\right]\right\} \end{aligned} \tag{5.55}$$

The density and temperature follow from (5.55). The ensuing expressions are identical in form, but vary only by a multiplicative constant in γ, namely $1/\gamma$ for ρ_1 and $1-1/\gamma$ for T_1.

5.2.5 First-Order VS Vorticity Transport

In order to determine the compressible correction, the first-order vorticity transport equation must be solved to determine the relationship between the vorticity and the stream function. It is not enough to assume the same relationship as the leading order, namely that $\Omega_1 = 4\pi^2 r\psi_1$, as this does not satisfy the vorticity transport equation. Instead, (4.38) is examined to derive the full relation. The right-hand side may be neglected, being the cross-product of co-linear vectors. Expanding the vector operators in the θ-direction for (4.38) gives

$$\frac{\partial}{\partial r}\left(u_0\Omega_1 + u_1\Omega_0\right) + \frac{\partial}{\partial z}\left(w_0\Omega_1 + w_1\Omega_0\right) = 0 \tag{5.56}$$

To relate ψ to Ω, the velocities may be eliminated in favor of the stream function, namely,

$$\frac{\partial}{\partial r}\left[-\frac{1}{r}\frac{\partial\psi_0}{\partial z}\Omega_1+\left(\frac{\rho_1}{r}\frac{\partial\psi_0}{\partial z}-\frac{1}{r}\frac{\partial\psi_1}{\partial z}\right)4\pi^2 r\psi_0\right] + \frac{\partial}{\partial z}\left[\frac{1}{r}\frac{\partial\psi_0}{\partial r}\Omega_1+\left(\frac{1}{r}\frac{\partial\psi_1}{\partial r}-\frac{\rho_1}{r}\frac{\partial\psi_0}{\partial r}\right)4\pi^2 r\psi_0\right]=0 \quad (5.57)$$

In order to solve for Ω_1, (5.57) may be expanded and simplified. One finds

$$\frac{\partial\psi_0}{\partial z}\left(\frac{\Omega_1}{r}-\frac{\partial\Omega_1}{\partial r}\right)+\frac{\partial\psi_0}{\partial r}\frac{\partial\Omega_1}{\partial z}= - 4\pi^2 r\left[\psi_0\left(\frac{\partial\rho_1}{\partial r}\frac{\partial\psi_0}{\partial z}-\frac{\partial\rho_1}{\partial z}\frac{\partial\psi_0}{\partial r}\right)-\frac{\partial\psi_1}{\partial z}\frac{\partial\psi_0}{\partial r}+\frac{\partial\psi_0}{\partial z}\frac{\partial\psi_1}{\partial r}\right] \quad (5.58)$$

While $\Omega_1 = 4\pi^2 r\psi_1$ is not completely correct, it leads to appreciable simplifications. One can then posit the following relation

$$\Omega_1 = 4\pi^2 r\psi_1 + \Omega_{1c} \quad (5.59)$$

where Ω_c is a corrective function that allows Ω_1 to satisfy the first-order vorticity transport equation. Substituting (5.59) back into (5.58) provides

$$\frac{\partial\psi_0}{\partial z}\left(\frac{\partial\Omega_{1c}}{\partial r}-\frac{\Omega_{1c}}{r}\right)-\frac{\partial\psi_0}{\partial r}\frac{\partial\Omega_{1c}}{\partial z}=4\pi^2 r\psi_0\left(\frac{\partial\rho_1}{\partial r}\frac{\partial\psi_0}{\partial z}-\frac{\partial\rho_1}{\partial z}\frac{\partial\psi_0}{\partial r}\right) \quad (5.60)$$

whence

$$\Omega_{1c} = rf(\psi_0)+\frac{\pi^2 z\kappa\sin(\pi r^2)}{r}\left(4\exp\left(-\frac{r^2V}{4}\right)-2\exp\left(-\frac{r^2V}{2}\right) + r^2V\left[\mathrm{Ei}\left(-\frac{r^2V}{4}\right)-\mathrm{Ei}\left(-\frac{r^2V}{2}\right)\right]-2\left\{1+\kappa^2\left[4\pi^2r^2z^2+\sin^2(\pi r^2)\right]\right\}\right) \quad (5.61)$$

where $f(\psi_0)$ is a yet to be determined function that will be used to satisfy the vorticity equation.

5.2.6 First-Order VS Stream Function Solution

Once Ω_1 is fully determined, (4.41) may be solved. To facilitate a solution, the stream function may be rewritten as

$$\psi_1 = z^3 G(r) + zH(r) \tag{5.62}$$

$$f(\psi_0) = A_1 z \sin(\pi r^2) + A_2 z^3 \sin^3(\pi r^2) \tag{5.63}$$

These relationships are deduced from previous experience (Majdalani, 2007a; Maicke and Majdalani, 2008b) and from the structure of the vorticity equation. Using (5.62), the second order partial differential equation in (4.41) is broken down into two second order ODEs. These are

$$G'' - \frac{G'}{r} + 4\pi^2 r^2 G = \frac{3}{4}\mathrm{A}_2 r^2 \sin\left(\pi r^2\right) - \frac{1}{4}\mathrm{A}_2 r^2 \sin\left(3\pi r^2\right) + 16\pi^4\kappa^3 r^2 \sin\left(\pi r^2\right) \tag{5.64}$$

and

$$\begin{aligned} H'' - \frac{H'}{r} + 4\pi^2 r^2 H = {} & \frac{\pi\kappa^3 \cos\left(3\pi r^2\right)}{2r^2} + 2\pi^2\kappa^3 \sin\left(\pi r^2\right) + 2\pi^2\kappa^3 \sin\left(3\pi r^2\right) \\ & - 4\pi^2\kappa \sin\left(\pi r^2\right) - \pi\kappa r^{-2} \cos\left(\pi r^2\right) \left[2 + \tfrac{1}{2}\kappa^2 + 2e^{-\frac{1}{4}r^2 V}\left(e^{-\frac{1}{4}r^2 V} - 2\right)\right] \\ & + 2\pi^2 r^2 \kappa \sin\left(\pi r^2\right) - \pi^2 r^2 \kappa V \sin\left(\pi r^2\right) \left[\mathrm{Ei}\left(-\tfrac{1}{4}V\right) - \mathrm{Ei}\left(-\tfrac{1}{2}V\right)\right. \\ & \left. + 2\mathrm{Ei}\left(-\tfrac{1}{2}r^2 V\right) - 2\mathrm{Ei}\left(-\tfrac{1}{4}r^2 V\right)\right] + 4\pi^2\kappa e^{-\frac{r^2 V}{4}} \sin\left(\pi r^2\right)\left(2 - e^{-\frac{r^2 V}{4}}\right) \\ & + 6G - \mathrm{A}_1 r^2 \sin\left(\pi r^2\right) \end{aligned} \tag{5.65}$$

These two coupled ODEs are then solved in succession to determine the first-order compressible correction to the stream function. The six constants are determined by applying the boundary conditions from (4.11), (4.13), and (4.15). It should be noted that each boundary condition actually supplies two equations. This stems from the requirement that each boundary condition must be satisfied for all values of z. The

procedure mirrors the first-order Bragg-Hawthorne analysis and hence will not be repeated here.

After applying the boundary conditions, the fully determined stream function may be written as

$$\begin{aligned}\psi_1 = &-\frac{1}{3}\pi^2 z^3 \kappa^3 \sin\left(\pi r^2\right)\left[\cos\left(2\pi r^2\right) - 1\right] \\ &+ \frac{1}{8}\pi z\kappa\left(\kappa^2 \sin\left(\pi r^2\right)\left[-2\mathrm{Si}\left(2\pi r^2\right) + \mathrm{Si}\left(4\pi r^2\right) - \mathrm{Si}(2\pi) + 2\mathrm{Si}(\pi)\right]\right. \\ &+ \cos\left(\pi r^2\right)\left\{4e^{-\frac{1}{4}r^2V}\left(2 - e^{-\frac{1}{4}r^2V}\right) - \left(r^2-1\right)\left[\gamma\left(3\kappa^2-4\right) - 4\right]\right. \\ &+ \kappa^2\left\{r^2\left[2\mathrm{Ci}(2\pi) - \mathrm{Ci}(4\pi)\right] + 2\gamma\left(r^2-1\right)\right\} - 2\left(Vr^2+2\right)\mathrm{Ei}\left(-\tfrac{1}{2}r^2V\right) \\ &+ 2(Vr^2+4)\mathrm{Ei}\left(-\tfrac{1}{4}r^2V\right) + \kappa^2\left[8\ln(2)\left(r^2-1\right) - 2\mathrm{Ci}\left(2\pi r^2\right) + \mathrm{Ci}\left(4\pi r^2\right)\right] \\ &\left.\left.+2\left(\kappa^2-4\right)\ln(r) - \left(r^2-1\right)\left[\kappa^2\ln(256\pi) + \ln\left(\frac{4096}{V^4}\right)\right]\right\}\right) \quad (5.66)\end{aligned}$$

Chapter 6

Constant Shear Stress Solution

This chapter departs from the Rayleigh-Janzen approach and instead focuses on modeling the swirl velocity in the core region of the confined vortex. At the outset, using the simple relation in (3.69) from Chapter 3, a solution for the swirl velocity that is valid for both laminar and turbulent regimes will be determined. In the first section, the general solution will be presented, while in the second, the emphasis will be shifted to a matching technique linking the radius to the vortex Reynolds number.

6.1 Constant Shear Stress (CSS) Solution

The constant shear stress solution hinges on the supposition that the pressure and shear stress forces must balance near the core. The mathematical expression of that principle is found in (3.69), reproduced here for the readers convenience

$$\epsilon \left(\frac{\partial v}{\partial r} - \frac{v}{r} \right) = C_1 \tag{6.1}$$

Upon integration, the expression for $v^{(i)}$ becomes

$$v^{(i)} = r \left[\frac{C_1}{\epsilon} \ln(r) + C_2 \right] \tag{6.2}$$

where the superscripted (i) denotes an inner solution, valid near the core of the vortex.

It may be interesting to note that each of the two undetermined constants, C_1 and C_2, has a clear physical meaning: while the first relates to the swirl strength of the velocity component generating the stress, the second corresponds to the swirl strength of a flow undergoing solid-body rotation. The two undetermined constants can be manipulated to match the inner solution with the outer, free vortex expression at their intersection point. This is achieved via equating the velocity and its derivative to the outer vortex at a specific matching radius. Since the matching radius is not known a priori, it must be carefully specified. For the moment, the matching point X is yet to be determined. The equation to match the velocities at X is

$$X\frac{C_1}{\epsilon}\ln(X) + XC_2 = \frac{1}{X} \tag{6.3}$$

Equation (6.3) is simply matching the inner solution from (6.2) to the outer, free vortex solution. The same procedure is used on the derivatives to provide

$$\frac{C_1}{\epsilon}\left[1 + \ln(X)\right] + C_2 = \frac{1}{X^2} \tag{6.4}$$

After solving (6.3) and (6.4) for C_1 and C_2 and substituting back into (6.2), the result may be expressed as

$$v = \begin{cases} \frac{r}{X^2}\left[1 - \ln\left(\frac{r^2}{X^2}\right)\right]; & r \leq X \\ \frac{1}{r}; & r > X \end{cases} \tag{6.5}$$

In what follows, this combined-vortex model is referred to as the constant shear model. The incontrovertible analogy with Rankine's laminar model is evident. Using a unified notation, Rankine's combined vortex may be similarly represented by

$$v = \begin{cases} r/X; & r \leq X \\ X/r; & r > X \end{cases} \tag{6.6}$$

Here $X = U/\bar{v}(aX)$ is the point where the inner vortex line intersects with the sloping tail of the outer vortex. This location also defines Rankine's maximum swirl velocity $v_{\max} = \bar{v}(aX)$. In contrast to the constant shear solution which predicts constant shear throughout the core region, Rankine's model predicts constant vorticity for $r \leq X$.

Given that the inner core velocity is bounded at the centerline, a companion pressure may be obtained that does not exhibit the inviscid singularity of its predecessor (see Vyas and Majdalani, 2006). From the conservation of momentum, the axially and radially integrated pressures become

$$p - p(1,0) = -\int_1^r \left(u_r \frac{\partial u_r}{\partial \bar{r}} + u_z \frac{\partial u_r}{\partial z} - \frac{u_\theta^2}{r} \right) \mathrm{d}r \tag{6.7}$$

and

$$p - p(1,0) = -\int_0^z \left(u_r \frac{\partial u_z}{\partial \bar{r}} + u_z \frac{\partial u_z}{\partial z} \right) \mathrm{d}z \tag{6.8}$$

Integration and combination of these equations provides the pressure distribution

$$\Delta p = \begin{cases} \frac{1}{2\kappa^4 r^2}\left(r^4 \left\{ 5 + \ln\left(\frac{r^4}{X^4}\right)\left[\ln\left(\frac{r}{X}\right) - 2\right]\right\} - \kappa^2 X^4 \sin^2(\pi r^2)\right) & \\ \quad -\kappa^2 \left[4\pi^2 z + \frac{\sin^2(\pi r^2)}{2r^2}\right] + K_1; & r \leq X \\ -\frac{1}{2r^2}\left[1 + \kappa^2 \sin^2(\pi r^2)\right] - \kappa^2 \left[4\pi^2 z + \frac{\sin^2(\pi r^2)}{2r^2}\right] + K_2 & r > X \end{cases} \tag{6.9}$$

where $\Delta p = p - p(1,0)$. The constant K_1 can be determined by setting the piecewise parts equal at $r = X$, while K_2 can be calculated by securing the boundary condition at the outer radius of the headwall:

$$\begin{cases} p(1,0) = -\dfrac{1}{2} + K_2 = 0, \\ p(X,0) = K_1 + 3X^{-2} = K_2, \end{cases} \quad \text{or} \quad \begin{cases} K_1 = \dfrac{1}{2} - 3X^{-2}, \\ K_2 = \dfrac{1}{2}, \end{cases} \tag{6.10}$$

Hence the piecewise pressure distribution can be displayed as

$$\Delta p = \begin{cases} \frac{1}{2\kappa^4 r^2}\left(r^4\left\{5+\ln\left(\frac{r^4}{X^4}\right)\left[\ln\left(\frac{r}{X}\right)-2\right]\right\}-\kappa^2X^4\sin^2(\pi r^2)\right) & \\ \quad +\frac{1}{2}-\frac{3}{X^2}-\kappa^2\left[4\pi^2 z+\frac{\sin^2(\pi r^2)}{2r^2}\right]; & r\le X \\ \frac{1}{2}-\frac{1}{2r^2}\left[1+\kappa^2\sin^2(\pi r^2)\right]-\kappa^2\left[4\pi^2 z+\frac{\sin^2(\pi r^2)}{2r^2}\right]; & r>X \end{cases} \tag{6.11}$$

6.2 Correlation with V

To illustrate the ability of the constant shear solution to embody different patterns, the present model is matched to the laminar core boundary layer model derived by Vyas and Majdalani (2006). For a portable solution, the swirl velocity calculated from the present work must approximate key features connected with the boundary layer model. For a simple demonstration of the matching paradigm, it is possible to implement the notion that swirl velocities from the laminar and constant shear models must exhibit the same maxima. This enables us to compare the principal flow attributes and gain insight into how the matching radius varies with the vortex Reynolds number.

While the inner part of the piecewise velocity yields

$$\left.\frac{\mathrm{d}v}{\mathrm{d}r}\right|_{r=r_{\max}} = 0 \quad \text{or} \quad r_{\max} = \frac{X}{\sqrt{e}} \tag{6.12}$$

the laminar model projects

$$r_{\max} = \sqrt{\frac{2}{V}\left[-1-2\mathrm{pln}\left(-1,-\frac{1}{2}e^{-\frac{1}{2}}\right)\right]} \simeq \frac{2.24}{\sqrt{V}}. \tag{6.13}$$

These positions can be substituted back into their respective equations and then equated identically. One gets

$$\frac{2}{Xe^{1/2}} = 1-e^{\frac{1}{2}+\mathrm{pln}\left(-1,-\frac{1}{2}e^{-\frac{1}{2}}\right)}\sqrt{\frac{-V}{2\left[1+2\mathrm{pln}\left(-1,-\frac{1}{2}e^{-\frac{1}{2}}\right)\right]}} \tag{6.14}$$

Equation (6.14) may be solved for X as a function of V directly from

$$X = \frac{2}{\sqrt{eV}} \frac{\sqrt{-2\left[1 + 2\mathrm{pln}\left(-1, -\frac{1}{2}e^{-\frac{1}{2}}\right)\right]}}{1 - \exp\left[\frac{1}{2} + \mathrm{pln}\left(-1, -\frac{1}{2}e^{-\frac{1}{2}}\right)\right]} \simeq \frac{3.80}{\sqrt{V}} \tag{6.15}$$

This matching radius X permits the piecewise velocity to capture the same peak velocity that the laminar boundary-layer solution projects as a function of V.

A comparison of the different swirl velocity models at three vortex Reynolds numbers is presented in Figure 6.1. While the free vortex is invariant with respect to V, both the present study and the laminar boundary layer model capture the increasing velocity peaks and their translation towards the centerline with successive increases in V. Note that the two models match identically at the point of the highest velocity, owing to the imposed matching treatment. They also behave rather similarly elsewhere in the domain, with the constant shear model decreasing from the peak velocity more slowly, owing to its wider profile. This behavior is consistent with observations of turbulent vortices.

Figure 6.2 compares the pressure distributions of the two models at two vortex Reynolds numbers. The radial pressure gradient is slightly higher in the case of the constant shear model, especially in the core region. This behavior can be accounted for by the slightly increased velocity anticipated from the piecewise model near the centerline. Except for these differences, the piecewise model seems to faithfully capture the general shape of the radial pressure distribution. For the pressure drop, the constant shear pressure starts slightly higher, but then quickly diminishes to match the laminar core approximation. It should be noted that the constant shear solution offers one degree of freedom that can be adjusted to suit a particular application. For example, should accurate prediction of the pressure stand as the most valuable requirement for a specific situation, then the matching radius could be adjusted to best fit the experimental pressure data near the core. A similar paradigm is used in modeling large atmospheric flows where only pressure-related measurements may be

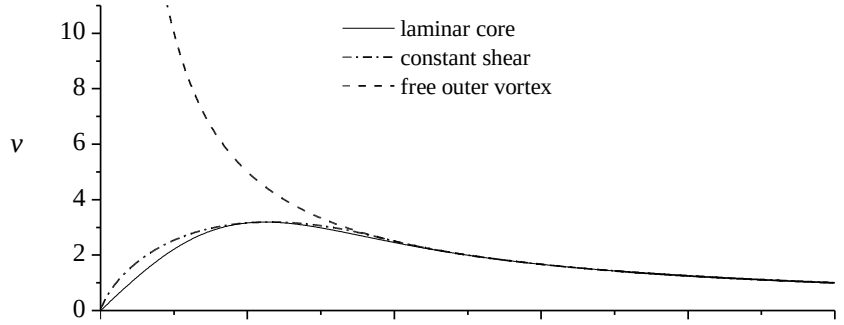

(a) $V = 100$

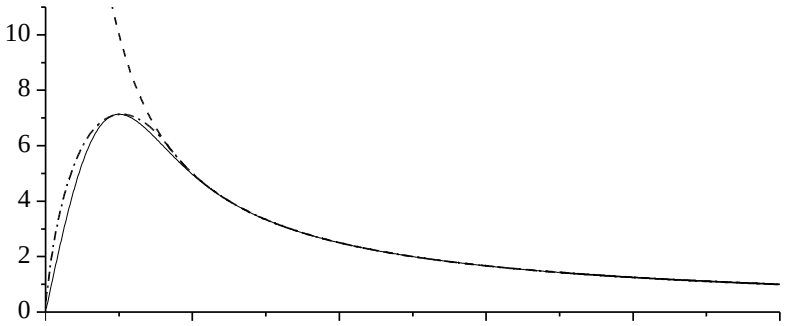

(b) $V = 500$

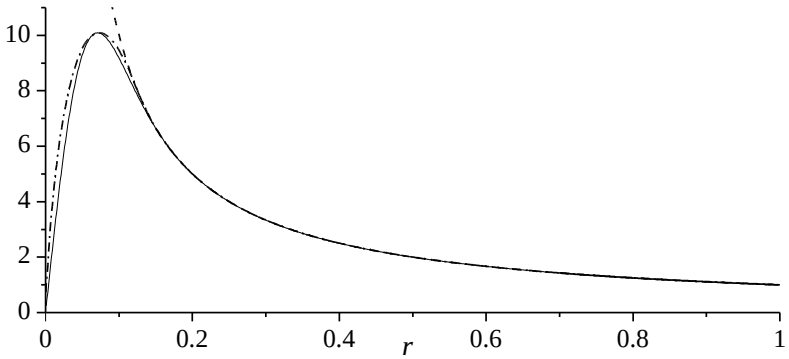

(c) $V = 1000$

Figure 6.1: Peak-matched swirl velocities at (a) $V = 100$, (b) $V = 500$, and (c) $V = 1000$ for the constant shear and laminar core models.

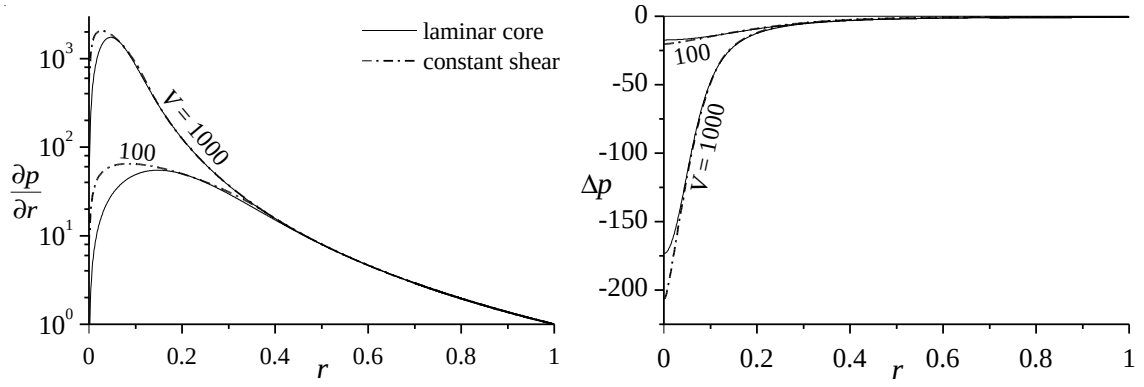

(a) Radial pressure gradient **(b)** Pressure drop

Figure 6.2: The (a) radial pressure gradient and (b) pressure drop for the peak-matched constant shear and laminar core models.

available (Trapp, 2000). As affirmed by Alekseenko et al. (1999), the swirl velocity core may be reconstructed in the absence of vortex breakdown using pressure measurements alone.

Before concluding this comparison, it may be instructive to examine the behavior of shear and vorticity near the axis of rotation. In the view of the shear stress being a quintessential contributor in the derivation of the constant shear approximation, the present result is compared to the laminar core solution by Majdalani and Chiaverini (2009). The latter is given by

$$\tau_{r\theta} = -2\epsilon r^{-2}\left[1 - \left(1 + \frac{Vr^2}{4}\right)e^{-\frac{Vr^2}{4}}\right] \tag{6.16}$$

Since only amendments to the swirl velocity are considered here, the affected member of the shear stress tensor is $\tau_{r\theta}$. Recalling the general form from (3.68) and after substitution, one retrieves

$$\tau_{r\theta} = \epsilon r \frac{\partial}{\partial r}\left(\frac{u_\theta}{r}\right) = \begin{cases} -\frac{2\epsilon}{X^2}; & r \leq X \\ -\frac{2\epsilon}{r^2}; & r > X \end{cases} \tag{6.17}$$

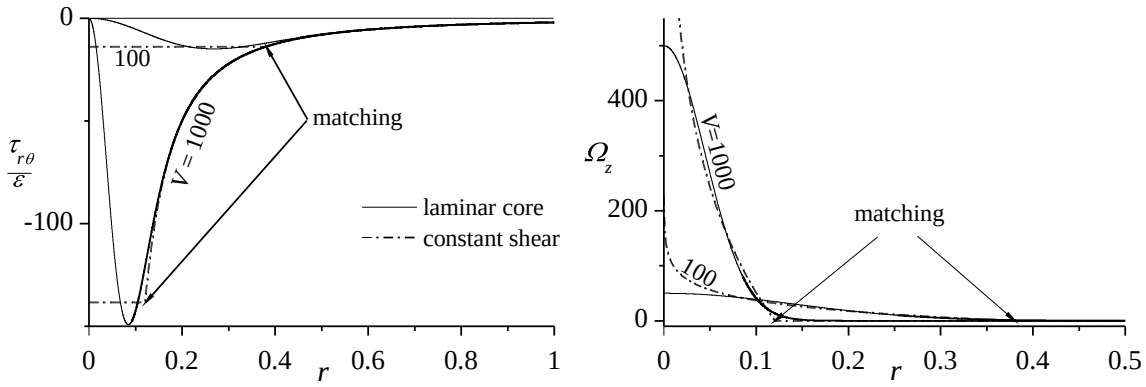

(a) Shear stress **(b)** Vorticity

Figure 6.3: The (a) shear stress and (b) vorticity for the constant shear and laminar core models.

For the vorticity, one finds

$$\Omega_z = \frac{1}{r}\frac{\partial\left(ru_\theta\right)}{\partial r} = \begin{cases} -\frac{4}{X^2}\ln\left(\frac{r}{X}\right) & r \le X \\ 0 & r > X \end{cases} \tag{6.18}$$

The resultant curves are plotted in Figure 6.3 and compared with the results of the laminar core treatment, namely, to $\Omega_z = \frac{1}{2}V\exp(\frac{1}{4}Vr^2)$. In both parts of Figure 6.3, a good agreement between the models is attained in the outer vortex region. Closer to the core, a deviation is manifested as a result of the constant shear stress model becoming uniform. The constant core value of the absolute shear $|\tau_{r\theta}|$ is slightly lower than the maximum laminar core value. Aside from this disparity near the centerline, the constant shear and laminar core curves are concurrent elsewhere in the domain. The vorticity prescribed by the piecewise model is seen to mimic the laminar core curve. However, unlike the laminar model that smoothly tapers off in the vicinity of the core, the constant shear vorticity does not approach a constant as $r \to 0$.

By comparing the combined-vortex representation to the laminar core model, two key observations may be drawn. The first consists of the ability of the shear stress model to mimic the features seen in the laminar core without a viscous perturbation near the centerline. By avoiding such analysis, the swirl velocity no longer depends

on the existence of a first-order radial velocity and small parameter expansions. The outcome is a model that captures the core behavior while requiring less overhead. The second benefit of a laminar core analogy is the development of a relation such as (6.15). This analytical expression linking the vortex Reynolds number to the matching radius X will later prove instrumental for properly interpreting experimental case studies in Chapter 7.

Chapter 7

Results

This chapter begins with a discussion of the compressible frameworks and the results from the analytical study. The velocity, density, and pressure profiles are presented as well as the variation in the mantle location. The sensitivity of the present work to the swirl parameter, κ is discussed as a mitigating factor on compressibility. The chapter closes with a discussion of the constant shear stress model and techniques to ensure that the analytical models presented here can accurately predict experimental results. The CSS and the laminar core approach are correlated with the experimental results found by Rom (2006) and found to accurately capture the velocity profiles for a range of experimental vortex Reynolds numbers.

7.1 Compressible Results

7.1.1 Velocity Profiles

Pursuant to the stream function determination, the compressible motion may be characterized in all three spatial directions. To avoid unnecessary collisions and potential recirculation, the open fraction at the base, β, may be conveniently equated to the dimensionless mantle radius with the effect of allowing the outgoing stream to exit the chamber unobstructed. Following Majdalani (2009), $\kappa = 1$ is used to

provide a magnified view of the variables of interest without suffering the incumbent reduction in accuracy that can accompany substantial increases in the reference Mach number. To facilitate comparisons relative to previous studies (Vyas and Majdalani, 2006; Majdalani, 2009; Majdalani and Chiaverini, 2009; Batterson and Majdalani, 2010a), the aspect ratio is taken to be $l = 4/3$, while typical values of $\gamma = 1.2$ and 1.4 are assigned to the ratio of specific heats. As for the injection Mach number, the analysis is anchored around $M_0 = 0.1$ and 0.2, being two commonly used values in propulsive applications.

Thus motivated by the need to characterize the VCCWC bulk flow field, the axial velocity, w, is considered first as it drives engine performance after expansion. In Figure 7.1a the axial profile is considered at the chamber exit, $z = l$, for reference Mach numbers of 0.1 (blue) and 0.2 (red), and for $\gamma = 1.2$ (dashed), and 1.4 (dotted). At $M_0 = 0.1$, the compressible contribution seems to induce a minor though still visible variation in the profile; however, by increasing the injection speed to $M_0 = 0.2$, a substantially more appreciable effect is realized. These profiles also display a sensitivity to variations in γ. Clearly, increasing γ leads to a flattening in the inner vortex region. Similarly, along with the growth in the injection Mach number, the axial velocity exhibits a steepening effect. When this occurs, the polarity transition that accompanies mantle formation acquires a blunter slope as w crosses the radial axis vertically. This finding is consistent with the axial steepening observed in compressible models of solid rocket motors (SRMs) (see Balakrishnan et al., 1992; Majdalani, 2007a; Maicke and Majdalani, 2008b; Saad and Majdalani, 2010; Akiki and Majdalani, 2012). In contrast to the aforementioned studies, it appears that no net-amplification of the axial velocity may be noted, aside from a reshaping of the profile itself. As the conservation constraint at the exit must be completely satisfied at the leading order, the resulting mass exiting the chamber at the first order must be self-canceling when integrated over the flow cross-section. This requirement compels the contour to morph without affecting the overall mass flux. As for the compressible contribution, w_1, depicted in Figure 7.1b, it is featured for the two representative values of γ. Based

on the CBH framework, the first-order correction will be more pronounced at higher values of γ, $\forall M_0$. Additionally, it can be seen that the compressible contribution will vanish at two distinct points, namely, $r = 0.2$ and 0.75. These sites derive their location from the mass balance relation which, when applied to the compressible correction, will warrant the existence of two polarity switches in the axial velocity to produce a zero net flux.

Finally in Figure 7.1c, the compressible axial profile for the complex-lamellar (CL) is presented. The profile is akin to the Bragg-Hawthorne profile in that it exhibits a similar maximum amplification near the mantle. The mantle location is slightly different, owing to the sinusoidal nature of the CL model versus the Bessel function nature of the CBH. There are three significant departures from Figure 7.1a. First, the amplification of the profile is uniform at the exit; second, the magnitude shift at the exit is less significant; and finally there is no γ dependence. These discrepancies may be attributed to the fundamental differences between the models. For the first two issues, the application of boundary conditions is slightly different for the CL case. The conservation of mass boundary condition, while conceptually the same, is implemented in a different manner owing to the density profiles being different. The result is a mantle location that does not vary as widely when extended to compressible conditions. Furthermore, the resulting axial profile displays rather uniform magnification at the exit. The CL independence from γ stems from the difference between the two approaches considered. Whereas the density is determined directly in the Bragg-Hawthorne approach, it is a two step process in the CL model. First the momentum equation is solved for the pressure, and then the isentropic relation is used to find the density. Because the pressure has only a single γ and the ρ_1 definition divides out that γ, the resulting compressible expression becomes independent of the ratio of specific heats.

By virtue of continuity and momentum balances, elements of the steepening mechanism observed in w are transferred to the radial velocity, u, as shown in Figure 7.2a. For small deviations from the incompressible state where $M_0 = 0$, the solution

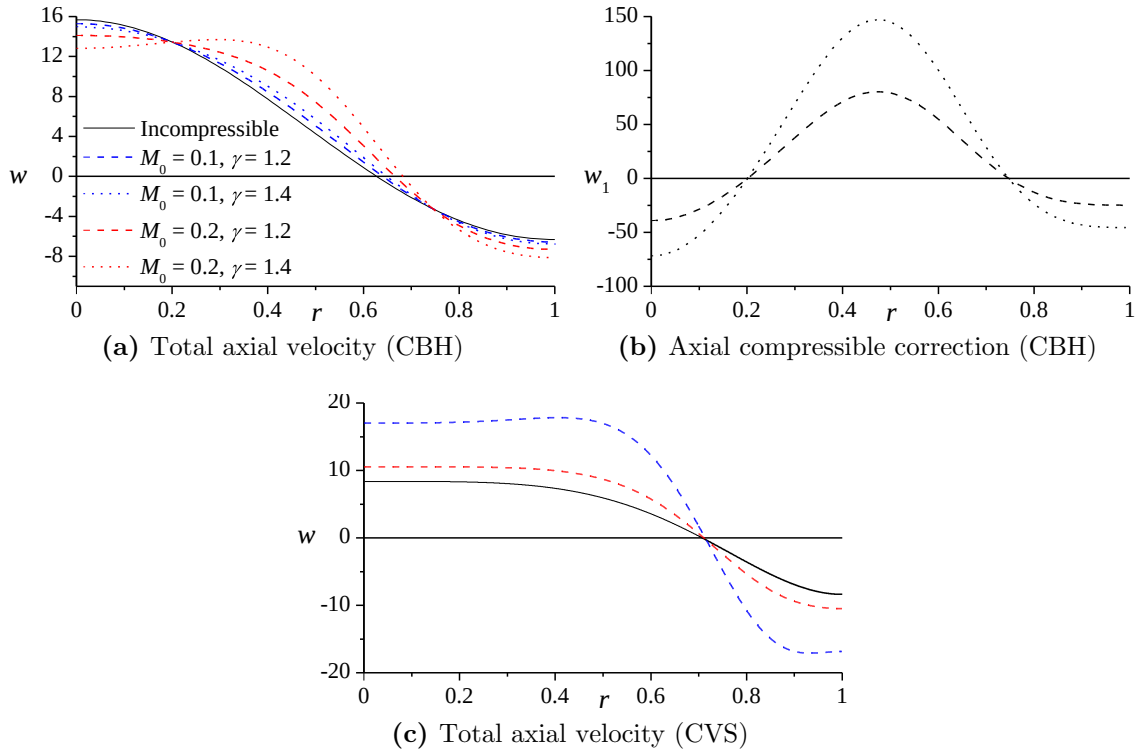

(a) Total axial velocity (CBH)

(b) Axial compressible correction (CBH)

(c) Total axial velocity (CVS)

Figure 7.1: The CBH (a) axial velocity, (b) compressible correction and CVS (c) axial velocity profiles.

seems to be fairly well guided by the unperturbed profile. In this case, the effect of compression causes a spatial shifting of the peak magnitude in u towards $r = 1$. As the Mach number is further increased to $M_0 = 0.2$, the outward shift in peak amplitudes is accompanied by a more visible increase in $u_{\max}$ beyond its incompressible counterpart. This particular amplification of u in the vicinity of the mantle can be so pronounced that it must be offset by an appropriate attenuation in the core region. The corresponding shift in u that is experienced near the centerline causes the radial profile to switch polarity while returning to $r = 0$. Mathematically, because the radial velocity is written as a z derivative of the stream function, it will be strongly influenced by the reversing nature imposed by the conservation principle in the exit plane. Here too, the compressible radial contribution vanishes at $r = 0.55$ as clearly depicted in Figure 7.2b. Even for $\kappa = 1$, the total radial velocity remains significantly smaller than the axial or tangential velocities, and this may be attributed to the sidewalls

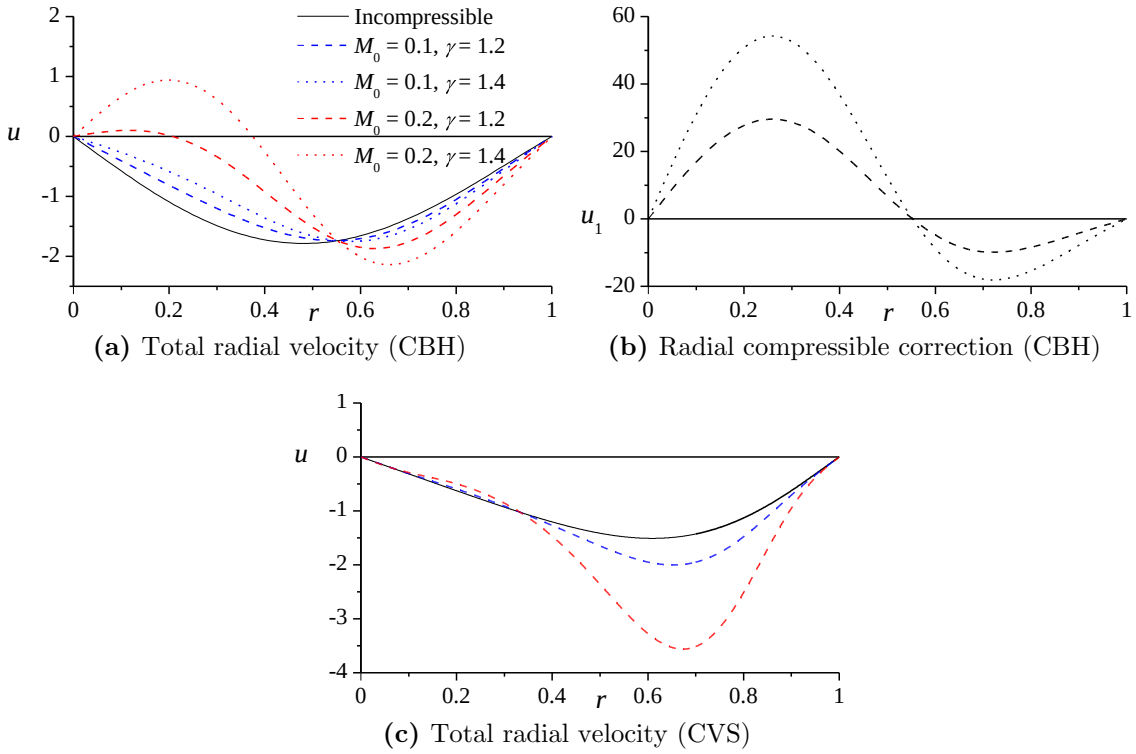

(a) Total radial velocity (CBH)

(b) Radial compressible correction (CBH)

(c) Total radial velocity (CVS)

Figure 7.2: The swirl normalized CBH (a) radial velocity, (b) compressible correction, and CVS (c) radial velocity profiles.

being non-injecting. Nonetheless, the compressible correction itself becomes of the same order in both axial and radial directions, hence leading to a proportionately larger effect on the radial velocity. This behavior will be reversed, however, when κ is reduced in a manner to mitigate the actual compressible contribution. Further discussion of this phenomenon appears in Section 7.1.4.

The behavior of the CL radial velocity in Figure 7.2c exhibits similar trends. The velocity is slightly diminished near the core and augmented near the peak, which also shifts toward the wall. The boost to the peak radial velocity is significantly larger than the CBH, but the fact that the general trends are very similar, despite their fundamental differences, is reassuring. In both cases, the actual increase in the radial velocity is virtually negligible once realistic values of κ are introduced.

The third, and most prominent component of the compressible velocity is illustrated in Figure 7.3a for the same two Mach numbers and ratios of specific heats. In

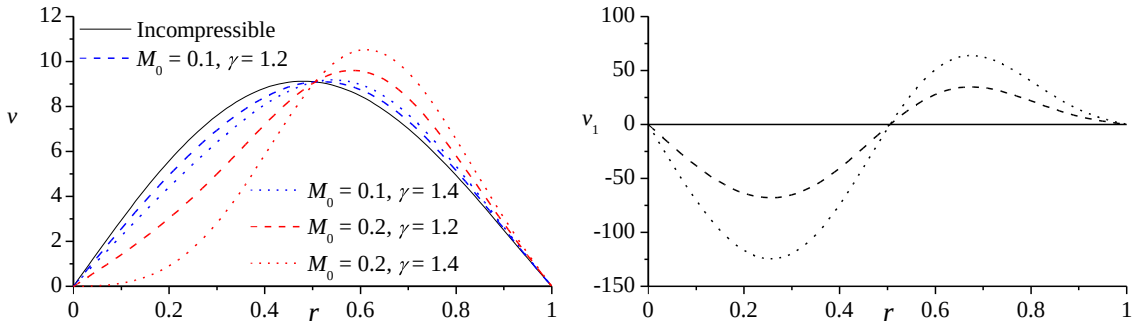

(a) Total swirl velocity (CBH) **(b)** Compressible swirl correction (CBH)

Figure 7.3: The κ normalized CBH (a) swirl velocity, (b) compressible correction, and CVS (c) swirl velocity.

comparison to u and w, the behavior of the swirl velocity v seems to mimic that of its radial counterpart; its profile is pushed closer to the sidewall with each additional growth in M_0 and γ. Here too, the maximum swirling speed is augmented with subsequent increases in the Mach number or the specific heats ratio. In Figure 7.3b, only the compressible correction is featured for $\gamma = 1.2$ and 1.4. In both cases, the compressible correction vanishes at $r = 0.5$. A closer look at v_1 reveals that its shape resembles the radial profile, except for being strictly positive for $0 < r < 1$. Mathematically, differences in magnitudes between u and v may be attributed to the reduced z dependence of the radial velocity. When examining the velocity-stream function definition for u in (3.27), the order of the z terms is reduced by the derivative operator, while v retains the full z dependence through its relation to B in (4.27).

Unlike the axial and radial components, the CL vortex requires an incompressible tangential velocity. This may seem counter-intuitive, but is a direct result of the mathematical formulation. The inviscid tangential momentum equation, used in the decoupling of the three velocity components, has no possible compressible correction as the leading and first-order equations are identical. Since the compressible correction cannot influence the behavior at the boundaries, the boundary condition for the swirl velocity must be zero. For this particular set of circumstances, this results in the compressible swirl correction being reduced to zero as well.

7.1.2 Mantle Variation

One interesting feature of the compressible solution stems from its mantle gaining an axial dependence that cannot be accounted for by the incompressible study. At the leading order, the mantle maintains a constant radial position for all values of z at approximately $r = 0.627$. In the compressible case, the mantle location gains a z dependence that is clearly illustrated in Figure 7.4 for several representative Mach numbers and values of γ. Accordingly, the mantle is seen to shift outwardly to a value of 0.639 in the proximity of the headwall ($z = 0$). Then as the fluid travels towards the exit plane, the mantle continues to slide outwardly, almost linearly in z, until reaching 0.681 at $z = l$. Such behavior appears to be consistent with previous theoretical findings based on an entirely different compressible flow approach (Maicke and Majdalani, 2008a). At first glance, the linear character of the mantle translation away from the headwall may be viewed as somewhat perplexing because of the solution's explicit dependence on z^3. However, in this situation, the low aspect ratio of $l = 4/3$ may be responsible for the linear behavior up to the exit plane. In longer chambers, it is likely for the linear behavior to become superseded by a cubic dependence, especially in the presence of sufficiently large reference Mach numbers.

The CL mantle (see Figure 7.4c) has a different base location, owing to the sinusoidal nature of the incompressible solution. By analogy with the Bragg-Hawthorne solution, the polarity switch for the axial velocity remains invariant with length for the incompressible description and both compressible corrections indicate an outward shift. The striking difference between the frameworks lies in the nature of the axial dependence. The CL has a less appreciable shift and the direction is inverted with respect to the CBH. This behavior may be attributed to the dissimilar natures of the models, specifically in the boundary conditions. The axial velocity experiences a uniform amplification, which when coupled with the density function, requires a smaller shift in the mantle location for the same amount of mass to exit the chamber. The inversion of the profile shape may be attributed to the ad hoc method with

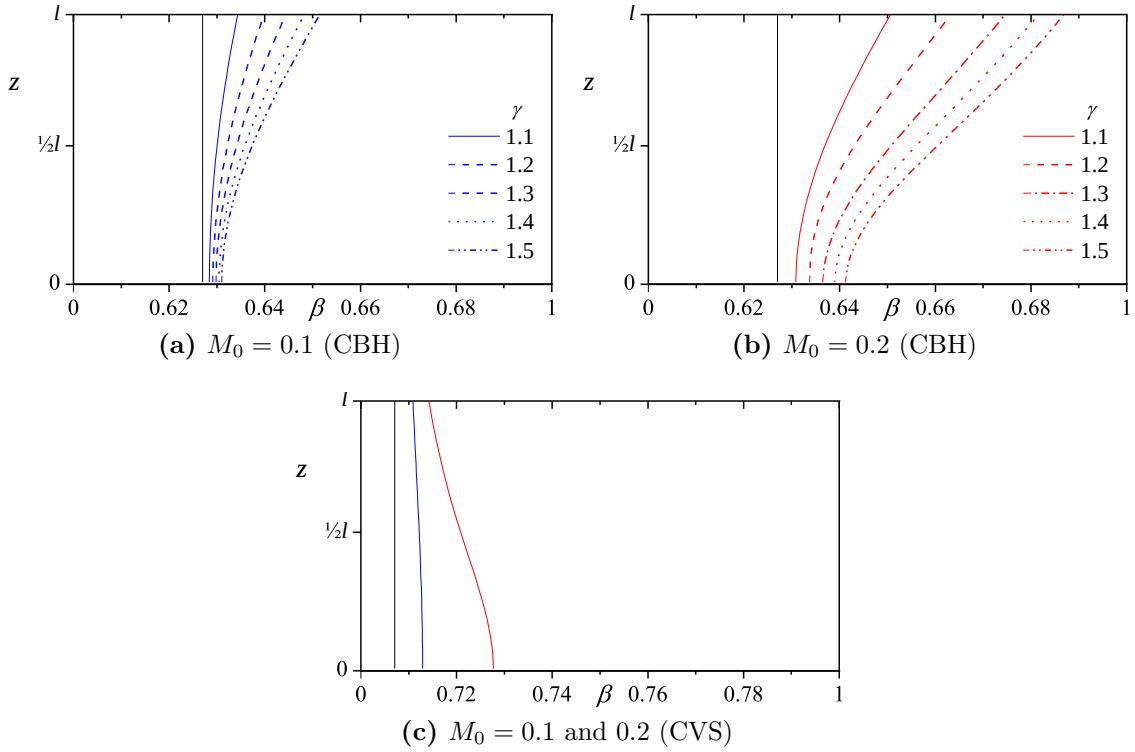

(a) $M_0 = 0.1$ (CBH)

(b) $M_0 = 0.2$ (CBH)

(c) $M_0 = 0.1$ and 0.2 (CVS)

Figure 7.4: The variation of the mantle location for the CBH at (a) $M_0 = 0.1$, (b) $M_0 = 0.2$, and (c) the CVS solutions.

which the swirl velocity is handled. The pressure and the density depend on the swirl profile, and since these models have disparate swirl velocities, their resulting density distributions, and by extension their compressible velocities, have differing characteristics as well. The reversal of the mantle profile shape is one such difference.

In what concerns experimental evidence, Smith (1962a,b) reports two antithetical outcomes, one in which the mantle slides inwardly, towards the centerline, as the distance from the headwall is increased, and one expanding outwardly, towards the sidewall. Like the compressible bidirectional vortex, Smith's experimental apparatus consists of a right circular cylinder with tangential injection near the base and an impervious headwall. Unlike the models presented here, Smith uses logarithmic-spiral blades to induce the swirl flow field, which also imparts an axial velocity component. He also has a submerged vortex finder at the base of the chamber, rather than the flat open fraction in the present model. Without further scrutiny, it may only be possible

to speculate over the factors leading to mantle variability. For example, it may be conceivable for viscous effects to compete with compressibility to the extent of one overpowering the other in a given configuration. It is more likely, however, that the geometric design of the inlet and outlet arrangements influence the stable position of the mantle interface between the inner and outer regions (Akiki and Majdalani, 2010, 2011). The presence of a protrusion into the flow, such as the submerged vortex finder appearing in Smith's experiments, may have an appreciable bearing on the final mantle location.

7.1.3 Thermodynamic Quantities

In the compressible Bragg-Hawthorne framework, all thermodynamic quantities may be restored from the density. In view of the isentropic relation used at the basis of the density-stream function formulation, the pressure and temperature may be straightforwardly deduced from the density. With this in mind, retrieving and characterizing the compressible density correction is paramount to the determination and analysis of the corresponding pressure and temperature fields. Both p_1 and T_1 differ from ρ_1 by a constant multiplier, namely,

$$p_1 = \gamma\rho_1 \quad \text{and} \quad T_1 = (\gamma - 1)\rho_1 \tag{7.1}$$

In Figure 7.5, density variations are shown in the exit plane for the two representative injection Mach numbers of $M_0 = 0.1$ and 0.2, using $\kappa = 1$ and a set of increasing values of $\gamma = 1.1, 1.2, ..., 1.5$. As it may be surmised from the graphs, the density appears to be sensitive to both variations in the Mach number and the specific heats ratio. However, the sensitivity to γ is amplified substantially when the Mach number is incremented from 0.1 to 0.2. This may be attributed to the former being closer to the leading-order benchmark than the latter. In any event, as the Mach number and γ are augmented, the normalized density undergoes successive decreases throughout the chamber, with the most significant depreciation occurring

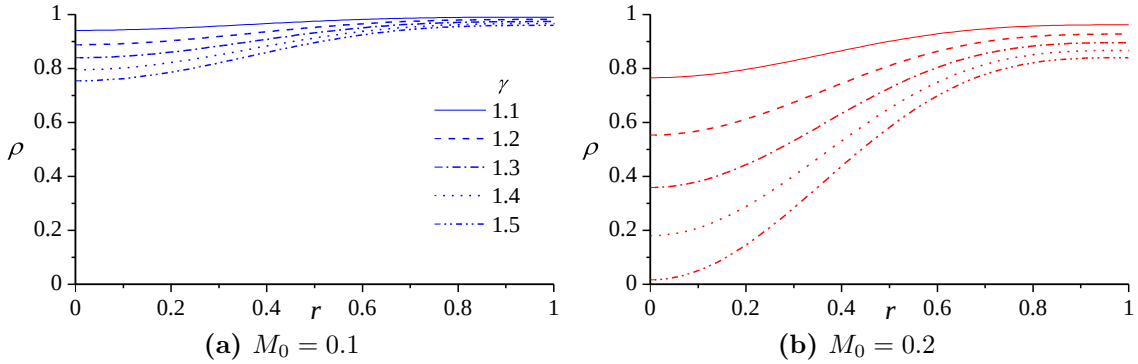

(a) $M_0 = 0.1$ **(b)** $M_0 = 0.2$

Figure 7.5: The density distribution at (a) $M_0 = 0.1$ and (b) $M_0 = 0.2$ for the CBH model.

along the centerline. It is this particular drop in density that drives, in part, the variation in the axial velocity correction at the first order through its contribution to the mass conservation requirement at $z = l$.

As for the pressure companion, similar trends are depicted in Figure 7.6, where the dimensionless pressure distribution is displayed for the same representative quantities used to analyze the density. Here too, the largest depreciation in the pressure is realized near the centerline, and this effect is accentuated at higher values of M_0 or γ. In the $M_0 = 0.2$ case, the compressible correction causes the pressure near the centerline to drop precipitously, leading to low suction conditions that become even more pronounced with successive increases in M_0 or γ. At this point, it may be useful to recall that, for the cyclonic motion to be stable, the upward streaming of the incoming fluid through a siphoning process is necessary to avoid premature short-circuiting or early spillage. It can hence be seen that suction conditions near the centerline can be beneficial to the proper and stable formation of a bidirectional vortex. In consequence, one may conclude that increasing the injection Mach number or the ratio of specific heats will enhance the suction level in the core region, a condition that can lead to a more stable cyclonic flow field.

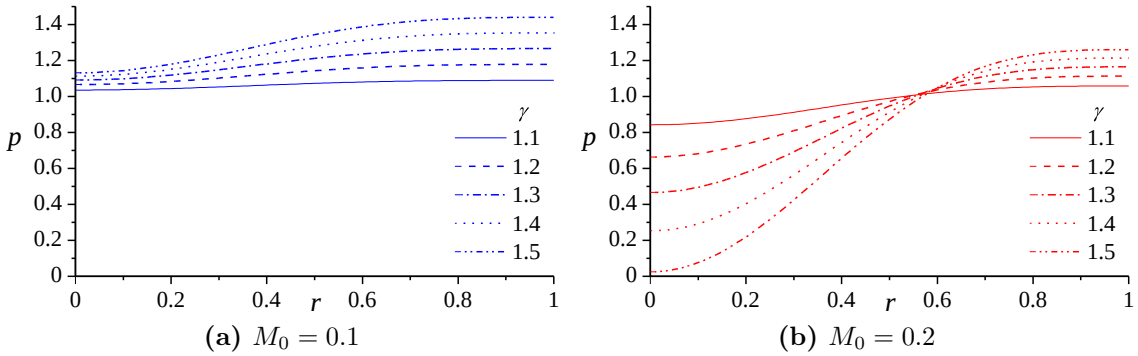

(a) $M_0 = 0.1$ **(b)** $M_0 = 0.2$

Figure 7.6: The pressure distribution at (a) $M_0 = 0.1$ and (b) $M_0 = 0.2$ for the CBH model.

7.1.4 Sensitivity to κ

Up to this point, the foregoing solutions have been evaluated for a unit κ. This convention has enabled us to amplify the effects of compressibility to the extent of better isolating and capturing the specific features associated with each variable of interest. Realistically speaking, it is possible for κ to take on smaller values, and these will lead to a reduction in the compressible axial and radial speeds alongside their compressible counterparts relative to the tangential velocity. From this perspective, the sensitivity of the compressible approximation to variations in κ can be essential to explore.

To study this sensitivity, the axial profile is re-examined at $z = l$, $\gamma = 1.4$, and both $M_0 = 0.1$ and 0.2. This is accomplished over a range of κ extending from 0.125 to 0.75 as depicted in Figure 7.7. It may be safely argued that the remaining dynamic and thermodynamic quantities will exhibit similar trends by virtue of their sensitivity to the swirl parameter κ being analogous to that of the axial velocity. As clearly illustrated on these graphs, decreasing κ leads to a corresponding drop in both compressible and incompressible axial velocities. The compressible contributions diminish even more rapidly, owing to their cubic dependence on κ, to the extent of approaching the incompressible approximation. Conversely, increasing the injection Mach number to 0.2 or higher stands to offset the effect of decreasing κ.

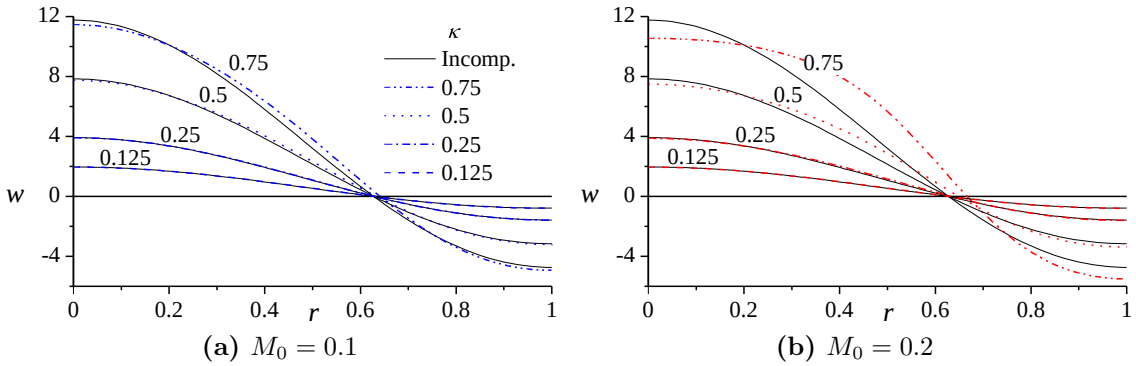

(a) $M_0 = 0.1$ **(b)** $M_0 = 0.2$

Figure 7.7: The sensitivity of the axial velocity to changes in κ at (a) $M_0 = 0.1$ and (b) $M_0 = 0.2$ for the CBH model.

At small κ, the axial and radial velocities, which can directly absorb the effects of compression in the absence of restrictions in the z and r directions, become overwhelmingly dominated by the tangential motion. Their overall magnitudes become small relative to v. The latter cannot experience compression in the tangential direction without violating the condition of axisymmetry. Its sensitivity to density variations can only be realized through its spatial dependence on the first-order stream function, and this association is commensurate with the size of both κ and M_0. Naturally, this coupling weakens at decreasing values of κ which, physically, implies the existence of higher levels of swirl and, therefore, stronger tendency to promote an axisymmetric distribution of flow field properties. So while higher orders of swirl increase the resistance to compression in the tangential direction, higher injection Mach numbers serve to counterbalance this effect, with the overall motion being controlled almost exclusively by these two contending factors. This behavior seems to support the tradition of relying on incompressible models for mean flow Mach numbers below 0.3, irrespective of the flow detail.

7.2 Constant Shear Stress Model

In Section 6.2, the constant shear stress model was correlated to the CL vortex of Majdalani and Chiaverini (2009). As a result of this initial correlation, a relationship linking the vortex Reynolds number and the matching radius was found, such that the peak velocities were matched. While useful as a proof of concept, a more practical use of the CSS model is to correlate the matching radius with experimental data. In what follows, the vortex Reynolds number relationship is modified to fit data published by Rom (2006). In the same vein, a modification to the laminar core model is also derived to facilitate comparison to experiment. Both of these adjustments employ an effective viscosity to adjust essentially laminar, non-turbulent, models to better agree with a turbulent experiment.

7.2.1 Experimentally Correlated Model

One of the chief attributes of the piecewise formulation stems from its display of a single degree of freedom that can be adjusted to minimize the error in its prediction. For example, knowing that the laminar boundary layer treatment can over-predict the velocity distribution near the core when the flow is turbulent, an empirically-based correction is necessary (e.g., when $V = 10^4$ the laminar model predicts $(u_\theta)_{\max} = 32$, an overestimated value). One avenue to evaluate this correction is through a least-squares analysis that enables us to determine the optimal matching radius that best fits the data. If a sufficient number of experiments are used, one could then deduce a relationship between the vortex Reynolds number and the matching location. Another possible approach is to introduce an effective vortex Reynolds number that can be correlated to its experimental counterpart. Given the increased turbulent viscosity observed in laboratory tests, the measured Reynolds number could thus be converted into a smaller effective equivalent that would be suitably retrofitted into the laminar solution. We explore both of these methods via the experimental data obtained by Rom (2006).

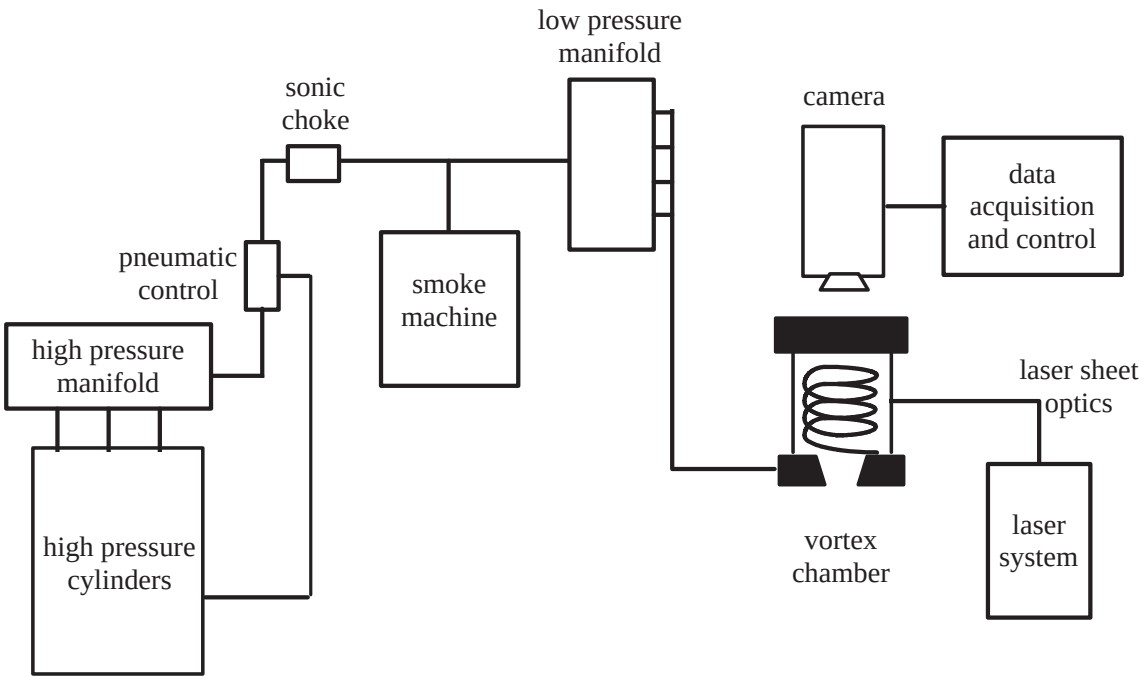

Figure 7.8: Schematic of experimental apparatus used by Rom (2006).

To set the stage, Rom's apparatus, shown in Figure 7.8, is equipped with particle image velocimetry (PIV) and a smoke generator that is capable of producing 0.2 mm seed particles. Particle images are captured by a LaVision Flowmaster 3 camera and cross-correlated to provide the swirl velocity at three axial locations in the cylindrical quartz chamber. To create different test environments, a modular chamber is used to alter the aspect ratio. Four tangentially located inlets in the base plate provide an injection method consistent with the boundary conditions outlined in (2.7). Given an operating pressure of 275 kPa for the chamber, variable inlets provide injection pressure drops that range from 10 to 30 percent of the chamber pressure. A summary of the conditions for each trial are provided in Table 7.1. While the constant shear model may be applicable to other experiments and numerical simulations, results available in the literature are seldom correlated with the vortex Reynolds number.

While the experimental study by Rom (2006) most closely matches the model derived here, the reported data would benefit from the introduction of uncertainty

Table 7.1: Available configurations for experimental trials.

(a) Geometric configurations

Length (cm)	Aspect Ratio	Axial Loc. (z/L)
3.56	2.80	0.5
6.10	4.80	0.2 0.5 0.7
8.64	6.80	0.2 0.5 0.7
11.2	8.82	0.2 0.5 0.7

(b) Injector configurations

Δp (% of p_c)	Port Dia. (cm)	Aggregate Inj. Area (cm^2)
10	0.605	2.299
20	0.500	1.571
30	0.442	1.228

quantification in the component measurements and in the PIV correlations. Such an accounting would improve the predictive capability of the present analysis. The methods presented here for correlating the analytical models to experiment retain their usefulness, and the addition of higher fidelity experimental data will enhance their attractiveness.

To help partially account for the lack of error quantification, an adjustment is made to V so that the resulting curve fits enclose rather than split the experimental data. The reason for such an adjustment lies with the increased drag on the particles in the core region, and the inherent separation mechanism that such a swirling flow provides. The actual fluid velocity in the core region should be universally greater than the experimentally determined velocity from the PIV measurements. Further details on this adjustment are presented in the following section.

7.2.2 Piecewise Least-Squares Regression

The piecewise least-squares code contains several distinct components. The first element is a rewrite of the standard least-squares technique in a manner to incorporate

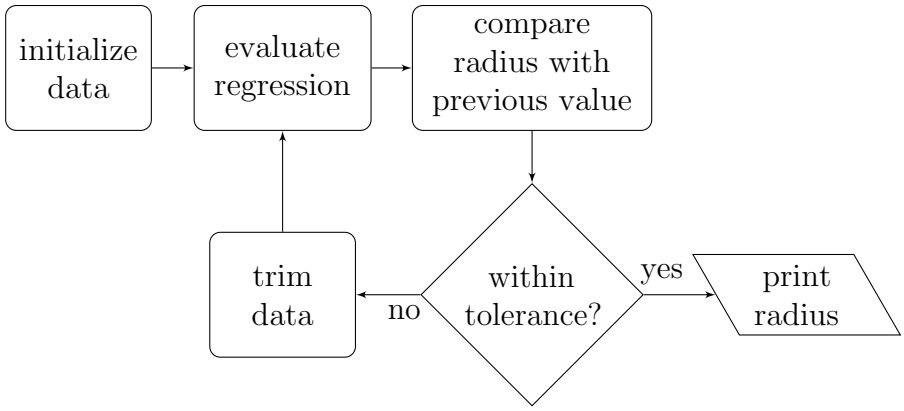

Figure 7.9: Flowchart of the piecewise least-squares algorithm.

the piecewise nature into the derivative calculations. The function returns the optimized parameter, in this case the matching radius, X. The second function is simply a truncation function that adjusts the data set to reflect the new optimization parameter. Finally, a control function loops over the data set, calling the least-squares function and comparing the new radius to the previous trial, X, until a satisfactory tolerance is reached, in this instance 0.0001. For the reader's convenience, a flow chart detailing the numerical procedure is provided in Figure 7.9.

This iterative procedure is necessary because of the nature of this particular piecewise solution. For most piecewise equations, a standard least-squares algorithm is sufficient. However, for the constant shear stress equation, the optimization parameter coincides with the matching radius that determines the boundary between the inner and outer solutions. As a result, the optimization space changes every time that a new radius is calculated. The iterative approach continues to calculate new values of X until the difference between successive radii falls below a user-specified tolerance. Since the data comprises a limited set of discrete points, convergence is rapid. The final radius is checked against neighboring values to ensure optimization.

Using a modified least-squares method similar to that employed by Vatistas (2006), one may analyze Rom's data and seek to determine the matching radius that minimizes the error between theory and experiment. Realizing that the radii calculated by this method vary with the vortex Reynolds number, the dependence on V is embedded

using a theoretically based relation similar in form to (6.15).

$$X = \frac{X_0}{\sqrt{V_t}} \tag{7.2}$$

where V_t is the turbulent vortex Reynolds number based on the molecular viscosity μ. In (7.2) the matching radius X is connected to the vortex Reynolds number through a yet to be determined constant. Because X only appears in the core region ($r < X$), the optimization procedure focuses on the points inside the matching radius, especially that the error outside of this region is invariant with respect to X. This permits the least-squares methodology to optimize the solution in the crucially important core region. Table 7.2 contains the available test cases, of which the first three are selected for the least-squares analysis. We also hold three trials in reserve, so that the validity of the relationship in (7.2) may be tested with independent data. While each set exhibits a slightly different matching radius, the values for X_0 appear to be in relatively good agreement (i.e. 50.7, 49.6 and 49.0 for turbulent vortex Reynolds numbers of $V_t = 23$, 29 and $41{\times}10^3$, respectively). This agreement lends support to the foregoing assumptions and enables us to seek a weighted average for X_0. We get

$$X = \frac{50}{\sqrt{V_t}} \tag{7.3}$$

By the way of confirmation, the same constant, $X_0 \simeq 50$, is obtained when the method of least-squares is applied to the entire collection of data, thus sweeping over the three sets simultaneously with the role of V_t being fully factored in.

We also compare a modified CL profile to both the data and to the CSS model. To this end, the CL profile is modified by an estimated turbulent eddy viscosity that reduces the experimental vortex Reynolds number to a value that conforms to the data. Following Faler and Leibovich (1978) or Escudier et al. (1980), one may

Table 7.2: Operational parameters for Rom's PIV experiments.

Parameter	Case 1	Case 2	Case 3	Case 4	Case 5	Case 6
$\Delta\bar{p}$ (kPa)	27.6	55.2	82.8	55.2	27.6	55.2
L	2.4	2.4	4.4	3.4	4.4	4.4
U (m/s)	68.73	77.72	89.61	88.78	74.81	88.31
$\sigma = a^2/A_i$	2.81	4.10	5.26	4.10	2.81	4.10
$\kappa = 1/(2\pi\sigma L)$	0.0239	0.0164	0.0069	0.0114	0.0129	0.0088
$V = \dot{m}_i/(L_0\mu)$	41000	29000	23000	25000	23000	18000

introduce the eddy viscosity ratio

$$\ell_t = \frac{\mu_t}{\mu} = \frac{\nu_t}{\nu} \tag{7.4}$$

This enables us to determine ℓ_t empirically from a standard least-squares analysis. As shown in Table 7.3, for each V_t a corresponding ℓ_t is found. Then based on the same three cases and 879 points, minimizing the least-squares error yields

$$\ell_t = 151.8 \;\text{ where }\; V = \frac{V_t}{\ell_t} = \frac{\bar{Q}_i}{L_0\nu_t} = \frac{\dot{m}_i}{L_0\mu_t} \tag{7.5}$$

It is reassuring to note, within experimental uncertainty, the constancy of the eddy viscosity ratio over the range of Reynolds numbers considered. Physically, the adjustment in (7.5) leads to a vortex Reynolds number calculation based on the turbulent viscosity. Substitution into (5.51) enables us to express the modified laminar core solution in the form

$$u_\theta = \frac{1}{r}\left[1 - \exp\left(-\frac{Vr^2}{4}\right)\right] \tag{7.6}$$

$$\nabla p = -\frac{1}{2r^2}\left\{1 + \frac{1}{2}\kappa^2\left[8\pi^2 r^2 z^2 + 1 - \cos(2\pi r^2)\right]\right.$$
$$\left. + e^{-\frac{1}{2}Vr^2} - 2e^{-\frac{1}{4}Vr^2} + \frac{1}{2}Vr^2\left[\mathrm{Ei}(-\frac{1}{2}Vr^2) - \mathrm{Ei}(-\frac{1}{4}Vr^2)\right]\right\} \tag{7.7}$$

Table 7.3: Least-squares parameters for laminar core and constant shear stress frameworks.

V_t	X_0	X	$50/\sqrt{V_t}$	ℓ_t
41000	49.04	0.243	0.230	150.3
29000	49.63	0.267	0.262	154.1
23000	50.67	0.314	0.288	151.0

Table 7.4: Statistical parameters for the regression of the laminar and constant shear stress models.

	V_t								
	41000			29000			23000		
	r_{cc}	σ_e	$\Delta E_t\%$	r_{cc}	σ_e	$\Delta E_t\%$	r_{cc}	σ_e	$\Delta E_t\%$
lam. core	0.887	0.592	4.91	0.962	0.276	1.47	0.870	0.391	3.45
CSS	0.900	0.558	4.36	0.968	0.253	1.23	0.880	0.376	3.19

To objectively compare the accuracy, several statistical parameters are calculated (see Table 7.4). By comparing correlation coefficients, r_{cc}, standard errors, σ_e and total relative errors, ΔE_t, the constant shear-based model seems to provide a slightly better fit to the data than the modified laminar distribution. The standard and total relative errors are calculated from

$$\sigma_e = \frac{1}{\sqrt{n-1}} \sqrt{\sum_{i=1}^{n} \left[\hat{u}_\theta(r_i) - u_\theta(r_i)\right]^2} \tag{7.8}$$

and

$$\Delta E_t = \sum_{i=1}^{n} \left[\hat{u}_\theta(r_i) - u_\theta(r_i)\right]^2 / \sum_{i=1}^{n} \hat{u}_\theta^2(r_i) \tag{7.9}$$

where n and $\hat{u}_\theta$ denote the number of data points and the measured velocity at r_i, the radius of the ith data point. The standard error of the estimate quantifies the spread of data about the regression line, much like the standard deviation that measures the spread about a mean value. As shown in Table 7.4, the total relative error falls under 3.19, 1.23, and 4.36 percent for the three cases associated with the constant

shear approach. The corresponding experimental correlation coefficients are 0.880, 0.968 and 0.900, respectively. When the modified laminar core technique is used, the relative errors slightly increase to 3.45, 1.47, and 4.91 percent, with an equally minute reduction in r_{cc}.

The least-squares fits are depicted graphically in Figure 7.10. The measurements collected in each trial correspond to the data acquired at three axial locations, specifically at $z = 0.2$, 0.5, and 0.7. The data agrees well in the outer vortex region, however in the core region the matching is less appreciable. It is clear that near the centerline, the velocity begins to deviate from the maximum theoretical values projected by the analytical models. Of equal concern is the scatter and scarcity of data in the core region. Contrary to the large number of closely packed data points in the outer region, fewer and more scattered data points appear near the core. This trend may be attributed to increased drag on seed particles in the peak-swirl region and to the natural tendency for separation of particles due to centrifugal entrainment. To adjust for this behavior, an adjustment is made to the calculation of the vortex Reynolds number such that the effective value of V is increased to provide a curve that is larger in magnitude which captures the anticipated fluid motion more closely. The values for V in cases 1-3 in Table 7.2 are increased from 41, 29, and 23×10^3 to 47, 36, and 30×10^3 respectively. These adjustments increase the peak velocity magnitude such that the analytical models enclose the majority of the data points. Using the adjustments to V as the basis for an error estimation, lumped errors of 15, 20, and 23 percent are calculated for the least-squares trials. In a similar manner, the values of V for cases 4-6 are raised from 25, 23, and 18×10^3 to 29, 28, and 22×10^3 with resultant errors of 14, 18, and 18 percent, respectively.

Using (7.3) and (7.5), a comparison is drawn in Figures 7.11 and 7.12 between the two empirical models and the experimental spread. On one hand, Figure 7.11 displays the collection of data that was used in the least-squares analysis leading to the determination of the eddy viscosity ratio and the empirically based matching radius X. On the other hand, Figure 7.12 compares the solutions to the reserve data-sets that

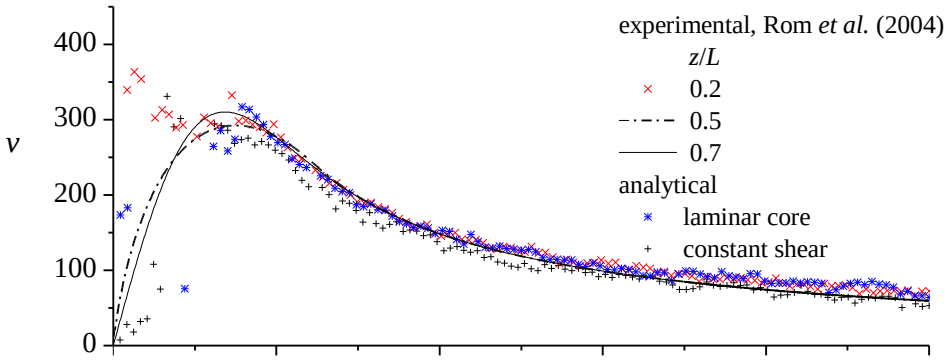

(a) $V = 41000$

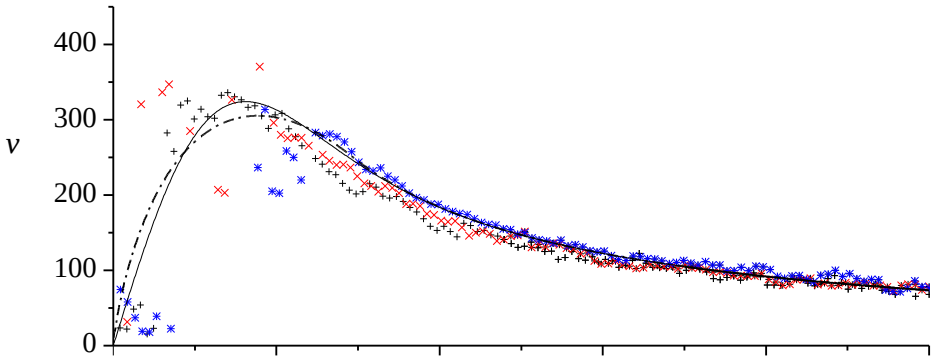

(b) $V = 29000$

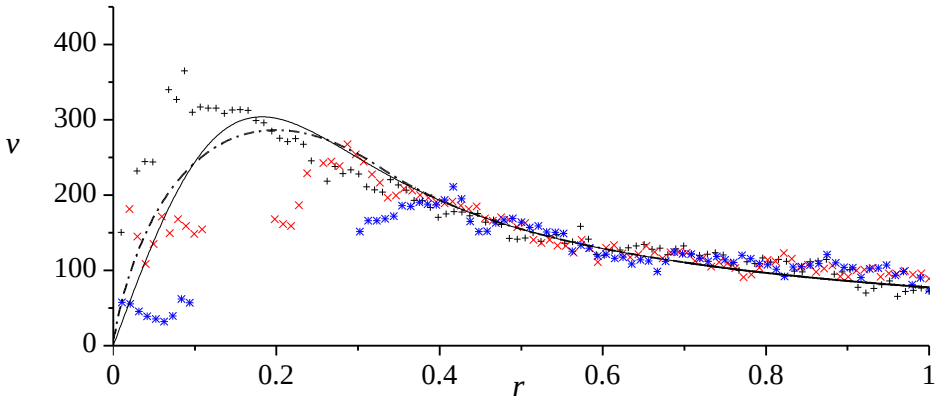

(c) $V = 23000$

Figure 7.10: The least-squares regression of the experimental data for (a) $V = 41000$, (b) $V = 29000$, and (c) $V = 23000$.

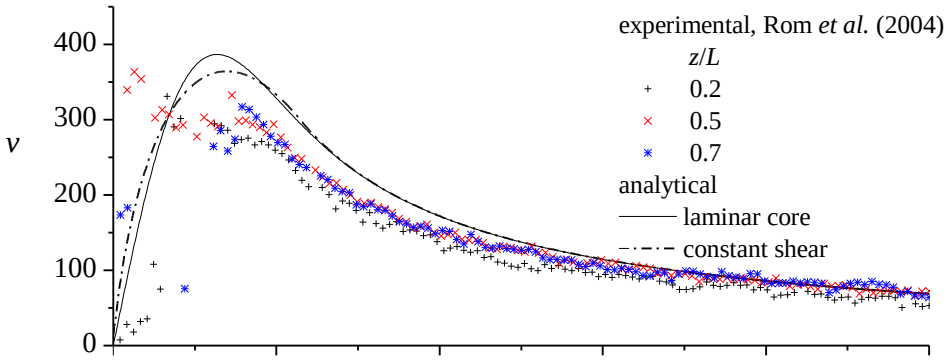

(a) $V = 47000$

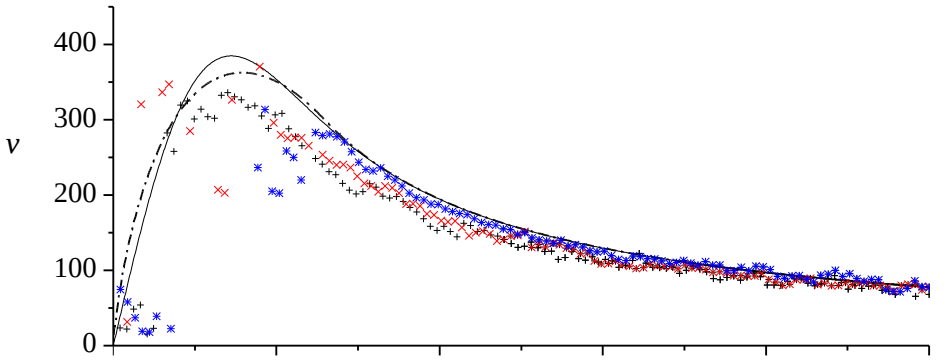

(b) $V = 36000$

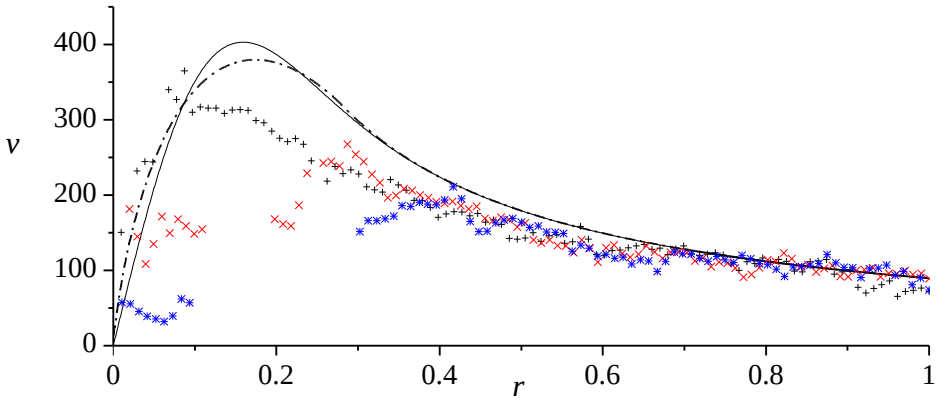

(c) $V = 30000$

Figure 7.11: Increased vortex Reynolds number fit with experimental data for (a) $V = 47000$, (b) $V = 36000$, and (c) $V = 30000$.

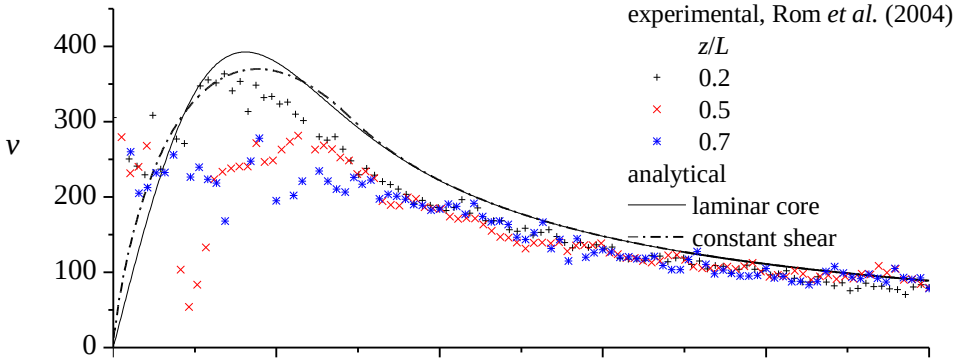

(a) $V = 29000$

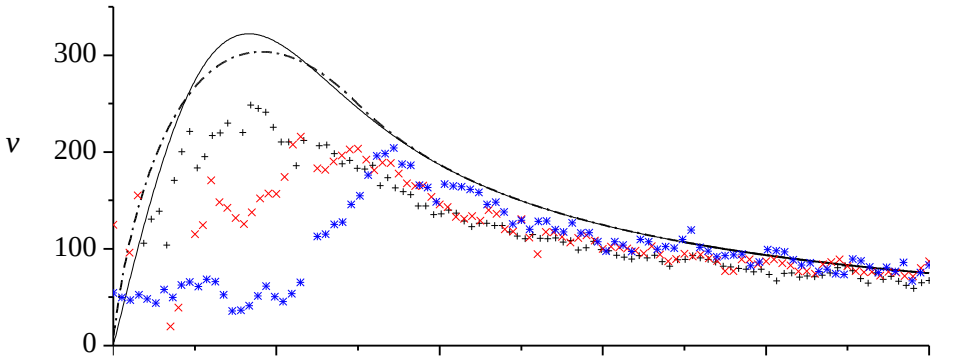

(b) $V = 27000$

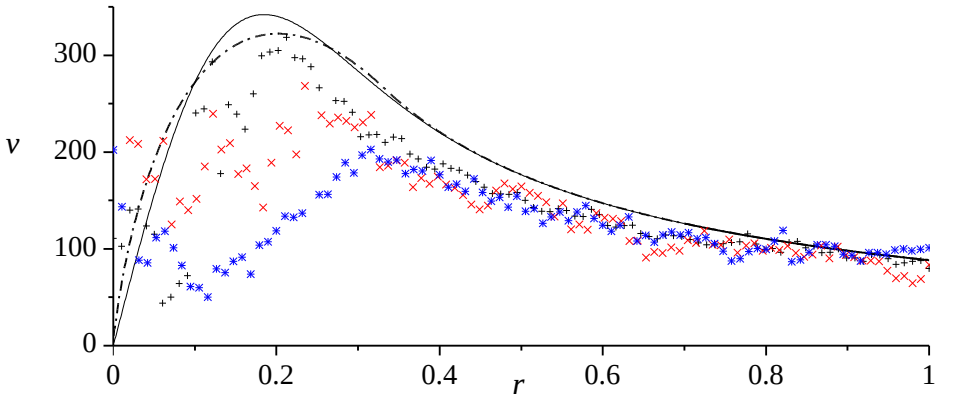

(c) $V = 22000$

Figure 7.12: Increased vortex Reynolds number fit with experimental data for (a) $V = 29000$, (b) $V = 27000$, and (c) $V = 22000$.

are not used in the calculations, but are rather saved for the sole purpose of testing the accuracy at various Reynolds numbers. While both frameworks capture the essential features, the constant shear-based model shows a broader bell-shaped contour than the narrower laminar profile. The adjusted fit behaves as anticipated, transforming the models to effective maxima for the slower, PIV velocity measurements. Ideally, a data set with increased fidelity and more consistent error quantification will make this post hoc adjustment unnecessary. Interestingly, the reduced fidelity in the core region is also depicted in the Reynolds shear-stress model data and laser Doppler velocimetry (LDV) measurements taken by Hu et al. (2005). Their LDV data acquisition system also deteriorates inwardly, past the point of maximum swirl.

7.2.3 Pressure Distribution

A comparison with the experimental pressure data is presented in Figure 7.13. The data are obtained using the apparatus described in the previous section and the first three cases defined in Table 7.2. Instead of seeding the flow for the purpose of PIV acquisition, a modified end cap is substituted with pressure taps located at non-dimensional radial intervals of 0.15, with the exception of two additional taps being placed near the wall at $r = 0.9$ and 0.967. For simplicity, the measurements are normalized by their values at the sidewall. As depicted in Figure 7.13, direct comparison with the CSS model reflects substantial agreement in the outer region leading to the sidewall. As the data approaches the centerline, the model continues to mimic the general shape of the experimental distribution, although the measurements are seen to fall below the theoretical prediction. This trend may be attributed, in part, to the incompressible character of the approximation.

In two recent investigations by Majdalani (2007a) and Maicke and Majdalani (2008b), accounting for compressibility effects was shown to reduce the pressure near the core with successive increases in flow speed. This behavior is further confirmed by Vatistas and Aboelkassem (2006) in a similar study of industrial cyclones.

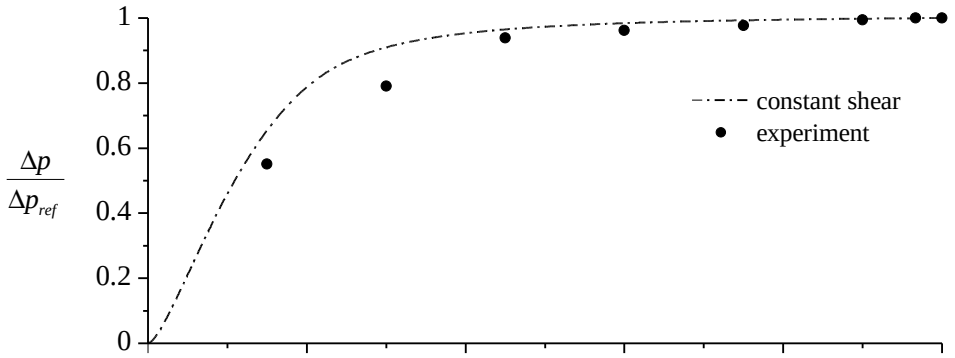

(a) $V = 47000$

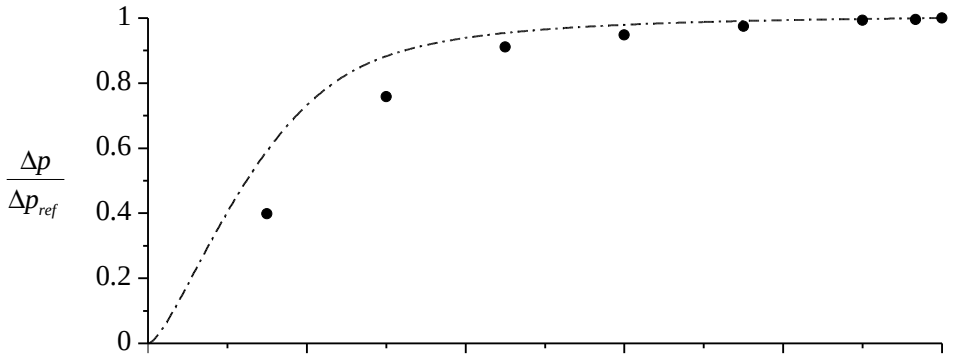

(b) $V = 36000$

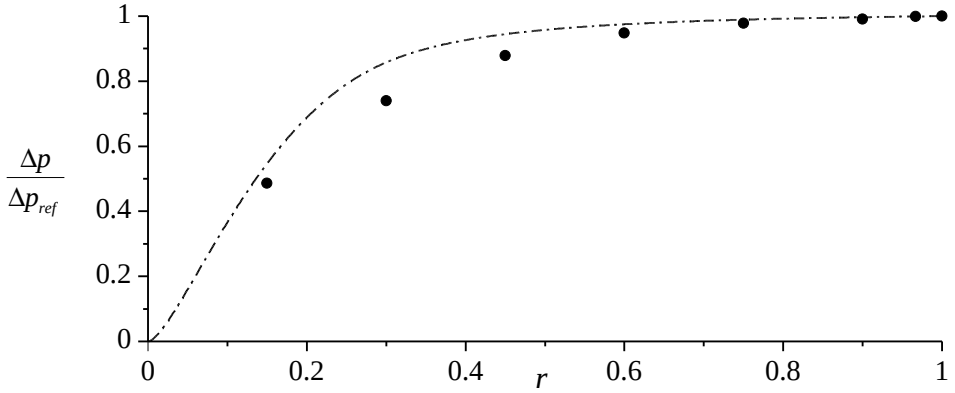

(c) $V = 30000$

Figure 7.13: The CSS model compared to the experimental pressure data for (a) $V = 47000$, (b) $V = 36000$, and (c) $V = 30000$ at the headwall.

7.2.4 Limitations

Clearly, the models presented here are not unique as other reconciliatory schemes may be derived. The CSS model swirl overshoot and location must be thoroughly interrogated for validity via comparisons with experimental and robust computational predictions. Another model that may be pursued consists of calculating the matching radius such that the integrated shear stress associated with the constant shear approximation can be made to match the corresponding value predicted by the laminar core solution. At the outset, the surface areas under the $\tau_{r\theta}$ curves in Figure 6.3 may be matched. Whether such a scheme could produce a more accurate approximation will remain a matter of conjecture until such time when the model is compared with a sufficiently large collection of measurements and numerical predictions that are focused on parametric variations in the vortex Reynolds numbers. In similar fashion, the pressure distribution could be taken to be the target function. As alluded to earlier, one may attempt to match pressure profiles such as those arising in Figure 6.2 to the observed patterns. In short, the matching radius could be adjusted in a variety of ways to best reproduce laboratory or numerical experiments.

Finally, it must be borne in mind that with the full onset of turbulence, the expressions presented here may retain their predictive capability albeit at the expense of some loss in accuracy. Despite the presence of a nearly laminar core flow, the outer, annular motion may no longer remain irrotational. Turbulence has the ability to attract the surrounding irrotational fluid through frictional effects, specifically through entrainment Kundu and Cohen (2002). While the source of entrainment may be attributed to viscous shear in laminar flows, it is mostly inertial in turbulent flows. In fact, the entrainment rate under turbulent conditions can far exceed any effects that are attributable to fluid friction. When the laminar core is affected by the turbulent outer flow, the resulting fluid is turbularized by the introduction of small viscous eddies that can be formed at the interface between the rotational and irrotational regions. In the bidirectional vortex chamber, the turbulent annulus can

therefore entrain the core fluid to the extent of causing further departures from the newly established solutions. When these turbulent effects occur, one may expect to see higher swirl velocities from the peak region to the wall.

Chapter 8

Summary

In this dissertation, three separate models are presented for the advancement of modeling high-speed flows in swirl combustors. First, an important though often overlooked framework in fluid mechanics is revisited, namely, a differential technique that is based on the Bragg-Hawthorne equation. Second, the vorticity-stream function approach, popular in propulsive circles, is extended to account for compressibility. Finally, a constant shear stress model is developed to correlate the theoretical swirl velocities that occur to experimental conditions.

8.1 Compressible Frameworks

This Bragg-Hawthorne technique was originally developed to facilitate the modeling of axisymmetric, bathtub-like vortices with intense rotation along their primary axes. The equation itself proceeds from a vorticity-stream function transformation of Euler's inviscid equations into a single, second-order PDE with two principal functions: B, the tangential angular momentum, and H, the stagnation enthalpy or pressure head. In past research, this equation has been explored in a multitude of physical settings, mainly in the treatment of helical structures exhibiting strong axisymmetries, such as those in cyclone separators or turbine compressors. However, these studies have been limited in scope to inviscid and incompressible conditions.

The vorticity-stream function approach was popularized in the study of solid rocket motor internal ballistics. A combination of the vorticity and vorticity transport equations relates the tangential vorticity to the stream function by means of a generalized function. Like the traditional Bragg-Hawthorne framework, this technique is usually limited to incompressible studies, though recent works by Majdalani (2007a) and Maicke and Majdalani (2008b) have extended it to compressible conditions.

This work is primarily motivated by a propulsion related study, namely, by the need to describe the internal gas dynamics within a self-cooled thrust chamber wherein the propellant is compelled to follow a cyclonic flow path. At the outset, the effort is split into two main areas, first, at developing viable mathematical frameworks and, second, at using these frameworks to obtain compressible, inviscid, steady-state approximations for a cylindrical cyclone. In the first part, the focus is on producing the compressible analog of the Bragg-Hawthorne and vorticity-stream function approaches by deriving, under isentropic flow conditions, the compressible form of the these equations. By making use of the isentropic pressure-density relation, the stagnation enthalpy expression (in the case of the CBH) and the momentum equation (for the CVS) are employed to achieve the desired closure and, as such, establish the foundation for a well-posed paradigm relating the stream function and density. This effort gives rise to a pair of general CBH frameworks in the form of a density-stream function formulation with the freedom to select B and H or, in the case of the CVS, a relationship satisfying vorticity transport, that allows the investigator to satisfy the requisite boundary conditions. Despite the ability to solve the resulting PDEs by computer, the equations are linearized and then solved asymptotically for the wide class of problems in which a reference Mach number, M_0, could be designated as a primary perturbation parameter. Thus, using the Rayleigh-Janzen perturbation technique, the compressible frameworks are expanded asymptotically and linearized into several coupled PDEs of increasing order in M_0^2. In theory, the expanded equations could be retrieved to any desired order, which grants this approach the ability to achieve an arbitrary level of precision. More importantly perhaps, the strategy provides a clear

roadmap for producing analytical approximations to a wide range of fluid motions in which density variations may be appreciable.

As the current model is a cold flow analysis, the isentropic assumption provides a sound basis for an initial compressible flow model. For the CBH model, the purely inviscid solution meshes well with the reversible conditions. Employing the isentropic form in the CVS must be handled with more care. While the bulk of the solution is inviscid, the compressible correction requires a viscous-type boundary layer for the swirl velocity. In this case, the isentropic solution presented here should be thought of as a first approximation, with subsequent studies supplementing the original effort with additional boundary layer calculations at the wall and headwall and relaxing the isentropic assumption to account for both these additions and potential hot flow analyses.

In this second part, the relatively untested framework is applied to a specific profile of the confined bidirectional vortex. For this purpose, the so-called linear Beltramian and complex-lamellar models are considered to approximate the cyclonic flow field arising in the context of a swirl-driven, VCCWC thrust chamber. These particular models have been shown to exhibit features that are appropriate of laboratory experiments and numerical simulations of the VCCWC prototype and of similarly configured cyclone separators. It has also been derived directly from the incompressible form of the Bragg-Hawthorne equation in cylindrical coordinates.

As may be characteristic of any new approach, the actual application is met by several obstacles that are systematically identified and then overcome. In this case, the proper specification of the auxiliary functions (B and H in the CBH and the vorticity in the CVS) proves to be essential in achieving a valid expansion. Furthermore, it must be realized that the choices leading to an incompressible solution cannot be employed in the compressible framework without judicious modification. Although the incompressible guess function may provide a suitable seed or leading-order start of an expansion, it must be carefully amended by terms that stem from the particular solutions of the non-homogeneous PDEs. Along similar lines, ensuring a non-singular

density profile along the centerline is found to be vital in securing a solvable set of equations. In the CBH framework this is directly attributable to the selection of B and H, while in the CVS, a viscous correction is added to the swirl velocity to provide a physically realistic compressible solution. The present work provides guidelines for choosing B, H, and Ω along with potentially useful series expansions in terms of the reference Mach number.

Thus given a well-balanced procedure, the next challenge stands in resolving the boundary conditions appropriately. This aspect is rather straightforward, especially that the conventional constraints associated with the bidirectional vortex appear (and are hence secured) at the leading order. In consequence, corrections of order one and higher inherit strictly homogeneous conditions. When these conditions are systematically used to supplement the linearized density-stream function PDEs at each asymptotic level, a perturbation approximation of increasing accuracy can be achieved by solving the resulting sets of equations in ascending order. The remaining effort is facilitated by taking into account the one-way coupling that exists between the principal PDEs at successive orders. This enables us to solve for one function exclusively before substituting its outcome into the other. The analysis is also simplified by lumping analytically intractable integrals into special functions that can be carried conveniently throughout the derivation. Isolating these integrals not only reduces the algebra involved, but also permits the direct evaluation of boundary conditions and, as such, the attainment of a closed-form approximation. Finally, in view of the size of M_0, a first-order correction is sufficient to capture the bulk effects of fluid dilatation.

The characterization of the compressible Beltramian motion leads to quite interesting and rich patterns. In summary, increasing either the injection Mach number or, to a lesser extent, the ratio of specific heats, will trigger a steepening effect with respect to the incompressible flow analog. This steepening mechanism is accompanied by a sharp density expansion near the axis of rotation and an outward shifting of the mantle interface which separates the outer and inner vortex regions. At the outset, the annular region through which the incoming stream is funneled into

the chamber undergoes a constriction in its cross-sectional area. This pinching of the outer vortex is akin to the behavior exhibited by the annular region of the Vortex Injection Hybrid Rocket Engine (VIHRE) as a reaction to increasing the burning rate along its sidewall (Knuth et al., 1996; Majdalani, 2007b). Despite the model being incompressible, augmenting the injection mass flow rate within the outer annulus (by virtue of distributed mass addition along the sidewall) forces the mantle to slide outwardly. This outward movement is needed to increase the radius of the inner vortex in such a way to permit more mass to exit the chamber. In the compressible case, a similar mechanism is observed and this may be attributed to the density stratification that is induced by fluid compression in conjunction with the presence of strong radial gradients; these give rise to a higher density fluid in the outer vortex and a markedly lower density within the chamber core. Clearly, increasing the fluid density in the annular region is somewhat equivalent to increasing the mass flux locally. Both actions lead to a widening of the outlet section, an outward shifting of the mantle, and a corresponding redistribution of the velocity profiles. While a similar steepening due to compressibility has been noted in SRM internal ballistics (see Balakrishnan et al., 1992; Majdalani, 2007a; Maicke and Majdalani, 2008b; Saad and Majdalani, 2010; Akiki and Majdalani, 2012), the flattening of the Beltramian core profile remains spatially restricted; it follows a redistribution that enables the motion to still satisfy the conservation condition imposed at the inflow-outflow boundary in the exit plane.

In addition to the steepening caused by successive increases in the Mach number, the present study shows that higher values of M_0 lead to lower pressures in the core region. These, in turn, can promote a stronger siphoning process through which a more effective flow streaming towards the headwall is promoted along with a more stable development of cyclonic motion. Finally, the sensitivity analysis seems to reveal a trade-off between the injection Mach number and the inflow swirl parameter κ. Due to the inability of an axisymmetric flow field to experience density variations in the θ direction, lower values of κ can suppress the effects of fluid compression by reducing

the relative contributions of the axial and radial velocities. This behavior appears to be inline with the findings of the CVS model, which requires an incompressible swirl velocity, and has its compressible effects further mitigated with the lowering of κ. Such would be the outcome unless κ is offset by a sufficiently large Mach number.

In closing, the study presented here is not meant to be a comprehensive investigation of the compressible Bragg-Hawthorne equations. Our framework seems to be viable for a wide range of problems encompassing both confined and unconfined vortex flows. In the case of the bidirectional vortex, other candidate functions for B and H may be chosen to the extent of producing alternate models for the VCCWC internal flow field. While the present analysis focuses on the spatially linear solution to the stream function equation, it can be suitably extended to the axially trigonometric, nonlinear Beltramian case.

8.2 Constant Shear Stress Swirl Velocity

The constant shear stress model developed here extracts the near core velocity before matching it to the outer, inviscid solution, which is mainly irrotational. The approximation exhibits one degree of freedom in the matching radius that may be used to anchor the solution to a given flow. The matching algorithm is enhanced through the introduction of V, the vortex Reynolds number, by way of the laminar core solution of Majdalani and Chiaverini (2009). To facilitate comparison to the experimental data, a modified least-squares algorithm is developed to account for the moving boundary during the CSS optimization process.

Both the constant shear stress model and the laminar core model make use of an effective eddy viscosity to accurately represent the experimental data provided by Rom (2006). The effective viscosity is determined by a least-squares fit of both models to the experimental data. In the case of the CSS model, the data may be used directly in determining the matching radius, whereas in the laminar core model, the effective vortex Reynolds number is calculated instead. Based on available data, a

correlation constant of $X_0 \simeq 50$ is obtained, which allows the CSS model to match the experimental results over a wide range of V. Similarly, an enhanced eddy viscosity ratio of $\ell_t \simeq 152$, leads to good agreement between the laminar core model and experimental data. Both of these values are found to be invariant over the values of V that are considered with errors in the range of 15-25 percent.

8.3 Future Work

The Bragg-Hawthorne framework developed in this dissertation remains general enough to be employed in a wide variety of both swirl and non-swirl driven applications. For example, it should be possible to use the present framework to redevelop a compressible flow model for a solid rocket motor in cylindrical coordinates reminiscent of the vorticity-stream function solution of Majdalani (2007a). Additionally, it may be possible to revisit some of the classical vortex models presented in Chapter 2 and extend the original works to account for compressibility. Also of interest are alternate means of specifying the B and H parameters in the model. While the approach outlined in this dissertation provides one means of achieving an analytically tractable model, an alternate specification of these terms may also lead to new analytical solutions. Of particular interest are new specifications for B, which would imply a different swirl velocity profile than the one presented here.

The bidirectional vortex flow field has a number of avenues for further investigation. The experimental data from Rom (2006) has proven instrumental in the formulation and validation of the models in this dissertation. However, the original experiment was carried out prior to a number of the advances in confined vortex modeling. Specifically, Rom's study did not actively pursue or correlate data to the vortex Reynolds number, as it was unavailable when the study occurred. A new experiment fully characterizing a wide range of V would be instrumental in validating both the general models and the effective viscosity correlations developed in Chapter 6.

Since Rom's study only focused on the swirl velocity profile, additional studies incorporating stereoscopic PIV that could capture the fully three-dimensional character of the flow field would be invaluable. Such a data set would provide both verification of the compressible frameworks in their entirety, but also help in guiding the analysis of specific features, such as the variability of the mantle location presented in Section 7.1.2. With a modular test bed, the open fraction could be varied in an update to Smith (1962a,b) that would help to isolate the processes that causes such a shift.

Numerical models of the bidirectional vortex flow field have also been relatively scarce in the literature. Future numerical examinations could center around two separate approaches. In the first, a fully three-dimensional model would be explored using either commercial or custom CFD software. This line of inquiry remains the most arduous, as the full solution requires a compromise between realistic model and mesh generation and a solvable result. The value of such a comprehensive model would be much the same as a revisiting of the classical vortex experiments, providing both validation and additional data for any empirical correlations. In the second, a numerical solution to the reduced-order models would also be of a significant benefit. While the asymptotic approximations, both the compressible corrections presented here and the viscous corrections by Majdalani and co-workers (see Majdalani and Chiaverini, 2009; Batterson and Majdalani, 2010a,b,c,d), are well-behaved and match the existing experimental and numerical data available, a numerical solution to these frameworks would be worthwhile. The pseudo-spectral method adopted by Batterson and Majdalani (2011a,b) in their investigation of the biglobal instability of the bidirectional vortex may be modified to solve the PDEs of each framework.

Bibliography

Bibliography

Ackeret, J. (1928). Über Luftkräfte bei sehr grossen Geschwindigkeiten insbesondere bei ebenen Strömungen. *Helvetica Physica Acta*, 1:301–322.

Afanas'ev, V. L. and Fridman, A. M. (1993). Vortex structure in the gaseous disk of the galaxy Mrk 1040. *Astronomy Letters*, 19(5):319–323.

Akiki, G. and Majdalani, J. (2010). On the bidirectional vortex with arbitrary endwall velocity. In *46th AIAA Joint Propulsion Conference*, Nashville, TN. AIAA Paper 2010-6652.

Akiki, G. and Majdalani, J. (2011). On the viscous bidirectional vortex with arbitrary endwall injection. In *47th AIAA Joint Propulsion Conference*, San Diego, CA. AIAA Paper 2011-5692.

Akiki, M. and Majdalani, J. (2012). Improved integral form of the compressible flowfield in thin channels with injection. *AIAA Journal*, 50(2):385–493.

Alekseenko, S. V., Kuibin, P. A., Okulov, V. L., and Shtork, S. I. (1999). Helical vortices in swirl flow. *Journal of Fluid Mechanics*, 382:195–243.

Anacleto, P. M., Fernandes, E. C., Heitor, M. V., and Shtork, S. I. (2003). Swirl flow structure and flame characteristics in a model lean pre-mixed combustor. *Combustion Science and Technology*, 175(8):1369–1388.

Balakrishnan, G., Liñán, A., and Williams, F. A. (1991). Compressible effects in thin channels with injection. *AIAA Journal*, 29(12):2149–2154.

Balakrishnan, G., Liñán, A., and Williams, F. A. (1992). Rotational inviscid flow in laterally burning solid propellant rocket motors. *Journal of Propulsion and Power*, 8(6):1167–1176.

Barber, T. A. and Majdalani, J. (2009). Exact Eulerian solution of the conical bidirectional vortex. In *45th AIAA Joint Propulsion Conference and Exhibit*, Denver, CO. AIAA Paper 2009-5306.

Barsony-Nagy, A., Er-El, J., and Yungster, S. (1987). Compressible flow past a contour and stationary vortices. *Journal of Fluid Mechanics*, 178:367–378.

Batterson, J. and Majdalani, J. (2010a). On the viscous bidirectional vortex. part 1: Linear beltramian motion. In *46th AIAA Joint Propulsion Conference*, Nashville, TN. AIAA Paper 2010-6763.

Batterson, J. and Majdalani, J. (2010b). On the viscous bidirectional vortex. part 2: Nonlinear beltramian motion. In *46th AIAA Joint Propulsion Conference*, Nashville, TN. AIAA Paper 2010-6764.

Batterson, J. and Majdalani, J. (2010c). On the viscous bidirectional vortex. Part 3: Multiple mantles. In *46th AIAA Joint Propulsion Conference*, Nashville, TN. AIAA Paper 2010-6765.

Batterson, J. and Majdalani, J. (2010d). Sidewall boundary layers of the bidirectional vortex. *Journal of Propulsion and Power*, 26(1):102–112.

Batterson, J. and Majdalani, J. (2011a). Biglobal instability of the bidirectional vortex. Part 1: Formulation. In *47th AIAA Joint Propulsion Conference and Exhibit*, San Diego, CA. AIAA Paper 2011-5648.

Batterson, J. and Majdalani, J. (2011b). Biglobal instability of the bidirectional vortex. Part 2: Complex lamellar and Beltramian motions. In *47th AIAA Joint Propulsion Conference and Exhibit*, San Diego, CA. AIAA Paper 2011-5649.

Bech, J., Gayà, M., Aran, M., Figuerola, F., Amaro, J., and Arús, J. (2009). Tornado damage analysis of a forest area using site survey observations, radar data and a simple analytical vortex model. *Atmospheric Research*, 93:118–130.

Beck, V. and Dotzek, N. (2010). Reconstruction of near-surface tornado win fields from forest damage. *Journal of Applied Meteorology and Climatology*, 49:1517–1537.

Bertato, M., Giaiotti, D. B., Mansato, A., and Stel, F. (2003). An interesting case of tornado in Friuli-northeastern Italy. *Atmospheric Research*, 67-68:3–21.

Bloor, M. I. G. and Ingham, D. B. (1973). Theoretical investigation of the flow in a conical hydrocyclone. *Transactions of the Institution of Chemical Engineers*, 51(1):36–41.

Bloor, M. I. G. and Ingham, D. B. (1987). The flow in industrial cyclones. *Journal of Fluid Mechanics*, 178:507–519.

Bragg, S. L. and Hawthorne, W. R. (1950). Some exact solutions of the flow through annular cascade actuator disks. *Journal of the Aeronautical Sciences*, 17(4):243–249.

Bruce, C. E. R. (1961). Spiral stellar nebulae and cosmic gas jets. *Journal of the Franklin Institute*, 271(1):1–11.

Burgers, J. M. (1948). A mathematical model illustrating the theory of turbulence. *Advances in Applied Mechanics*, 1:171–196.

Chiaverini, M. J., Malecki, M. J., Sauer, J. A., and Knuth, W. H. (2002). Vortex combustion chamber development for future liquid rocket engine applications. In *38th AIAA Joint Propulsion Conference and Exhibit*, Indianapolis, IN. AIAA Paper 2002-4149.

Cohen, M. J. (1984). High-lift airfoil design from the hodograph. *Journal of Aircraft*, 21(10):760–766.

Culick, F. E. C. (1966). Rotational axisymmetric mean flow and damping of acoustic waves in a solid propellant rocket. *AIAA Journal*, 4(8):1462–1464.

Depperman, C. E. (1947). Notes on the origin and structure of Philippine typhoons. *Bulletin of the American Meteorological Society*, 27:6–8.

Devenport, W. J., Rife, M. C., Liapis, S. I., and Follin, G. J. (1996). The structure and development of a wing-tip vortex. *Journal of Fluid Mechanics*, 312:67–106.

Devenport, W. J., Zsoldos, J. S., and Vogel, C. M. (1997). The structure and development of a counter-rotating wing-tip vortex pair. *Journal of Fluid Mechanics*, 332:71–104.

Emanuel, K. A. (1995). The behavior of a simple hurricane model using a convective scheme based on subcloud-layer entropy equilibrium. *Journal of the Atmospheric Sciences*, 52(22):3960–3968.

Escudier, M. P., Bornstein, J., and Zehnder, N. (1980). Observations and LDA measurements of confined turbulent vortex flow. *Journal of Fluid Mechanics*, 98:49–63.

Faler, J. H. and Leibovich, S. (1978). An experimental map of the internal structure of a vortex breakdown. *Journal of Fluid Mechanics*, 86(2):313–335.

Gerz, T., Holzäpfel, F., Bryant, W., Köpp, F., Frech, M., Tafferner, A., and Winckelmans, G. (2005). Research towards a wake-vortex advisory system for optimal aircraft spacing. *Comptes Rendus Physique*, 6(4-5):501–523.

Heaslet, M. A. (1944). Compressible potential flow with circulation about a circular cylinder. Technical Report 780, NACA.

Hoekstra, A. J., Derksen, J. J., and van den Akker, H. E. A. (1999). An experimental and numerical study of turbulent swirling flow in gas cyclones. *Chemical Engineering Science*, 54(13):2055–2065.

Hogsett, W. and Zhang, D.-L. (2009). Numerical simulation of Hurricane Bonnie (1998). Part III: Energetics. *Journal of Atmospheric Sciences*, 66(9):2678–2696.

Holland, A. P., Riordan, A. J., and Franklin, E. C. (2006). A simple model for simulating tornado damage in forests. *Journal of Applied Meteorology and Climatology*, 45(12):1597–1611.

Holland, G. J. (1980). An analytic model of the wind and pressure profiles in hurricanes. *Monthly Weather Review*, 108:1212–1218.

Hu, L. Y., Zhou, L. X., Zhang, J., and Shi, M. X. (2005). Studies of strongly swirling flows in the full space of a volute cyclone separator. *AIChE Journal*, 51(3):740–749.

Janzen, O. (1913). Beitrag zu Einer Theorie der Stationären Strömung Kompressibler Flüssigkeiten. *Physikalische Zeitschrift*, 14:639–643.

Kaplan, C. (1943). The flow of a compressible fluid past a curved surface. Technical Report 768, NACA.

Kaplan, C. (1944). The flow of a compressible fluid past a circular arc profile. Technical Report 994, NACA.

Kaplan, C. (1946). Effect of compressibility at high subsonic velocities on the lifting force acting on an elliptic cylinder. Technical Report 834, NACA.

Klein, R. I., Budil, K. S., Perry, T. S., and Bach, D. R. (2000). Interaction of supernova remnants with interstellar clouds: From the nova laser to the galaxy. *The Astrophysical Journal Supplement Series*, 127(2):379–383.

Knuth, W. H., Bemowski, P. A., Gramer, D. J., Majdalani, J., and Rothbauer, W. J. (1996). Gas-fed, vortex injection hybrid rocket engine. SBIR Phase I Final Technical Report NAS8-40679, NASA, Marshal Space Flight Center.

Königl, A. (1986). Stellar and galactic jets: Theoretical issues. *Canadian Journal of Physics*, 64(4):362–368.

Kundu, P. K. and Cohen, I. M. (2002). *Fluid Mechanics*. Academic Press, San Diego, CA, 2 edition.

Kuo, H. L. (1966). On the dynamics of convective atmospheric vortices. *Journal of the Atmospheric Sciences*, 23(1):25–42.

Lewellen, W. S. (1993). Tornado vortex theory. In Church, C., editor, *The Tornado: Its Structure, Dynamics, Prediction, and Hazards*, volume 79 of *Geophysical Monograph Series*, pages 19–39. American Geophysical Union, Washington, D. C.

Liepmann, H. W. and Roshko, A. (2001). *Elements of Gasdynamics*. Dover Publications, Inc.

Lin, J. C. (2002). Review of research on low-profile vortex generators to control boundary-layer separation. *Progress in Aerospace Sciences*, 38(4-5):389–420.

Lindemer, C. A., Plant, N. G., Puleo, J. A., Thompson, D. M., and Wamsley, T. V. (2010). Numerical simulation of a low-lying barrier island's morphological response to Hurricane Katrina. *Coastal Engineering*, 57:985–995.

Maicke, B. A. and Majdalani, J. (2008a). On the compressible bidirectional vortex. In *44th AIAA Joint Propulsion Conference*, Hartford, CT. AIAA Paper 2008-4834.

Maicke, B. A. and Majdalani, J. (2008b). On the rotational compressible Taylor flow in injection-driven porous chambers. *Journal of Fluid Mechanics*, 603:391–411.

Maicke, B. A., Saad, T., and Majdalani, J. (2010). On the compressible Hart-McClure mean flow motion in simulated rocket motors. In *46th AIAA Joint Propulsion Conference*, Nashville, TN. AIAA Paper 2010-7077.

Majdalani, J. (2007a). On steady rotational high speed flows: The compressible Taylor-Culick profile. *Proceedings of the Royal Society London A*, 463:131–162.

Majdalani, J. (2007b). Vortex injection hybrid rockets. In Kuo, K. and Chiaverini, M. J., editors, *Fundamentals of Hybrid Rocket Combustion and Propulsion*, Progress

in Astronautics and Aeronautics, chapter 6, pages 247–276. AIAA, Washington, D. C.

Majdalani, J. (2009). Exact Eulerian solutions of the cylindrical bidirectional vortex. In *45th AIAA Joint Propulsion Conference*, Denver, CO. AIAA Paper 2009-5307.

Majdalani, J. (2012). Flow-field structure of vortex combustors. In *International Symposium on Special Topics in Chemical Propulsion*, Quebec City, Canada. 9-ISICP.

Majdalani, J. and Chiaverini, M. J. (2009). On steady rotational cyclonic flows: The viscous bidirectional vortex. *Physics of Fluids*, 21:103603–15.

Makiya, S., Inasawa, A., and Masahito, A. (2010). Vortex shedding and noise radiation from a slat trailing edge. *AIAA Journal*, 48(2):502–509.

Mallen, K., Montgomery, M., and Wang, B. (2005). Reexamining the near-core radial structure of the tropical cyclone primary circulation: Implications for vortex resiliency. *Journal of the Atmospheric Sciences*, 62(2):408–425.

Meiron, D. I., Moore, D. W., and Pullin, D. I. (2000). On steady compressible flows with compact vorticity; the compressible Stuart vortex. *Journal of Fluid Mechanics*, 409:29–49.

Moore, D. W. and Pullin, D. I. (1991). The effect of heat addition on slightly compressible flow: The example of vortex pair motion. *Physics of Fluids A*, 3(8):1907–1914.

Moore, D. W. and Pullin, D. I. (1998). On steady compressible flows with compact vorticity; the compressible Hill's spherical vortex. *Journal of Fluid Mechanics*, 374:285–303.

Moscatello, A., Miglietta, M. M., and Rotunno, R. (2008). Numerical analysis of a mediterranean "hurricane" over southeastern Italy. *Monthly Weather Review*, 136:4373–4397.

Nolan, D. and Farrell, B. (1999). Generalized stability analyses of asymmetric disturbances in one- and two-celled vortices maintained by radial inflow. *Journal of the Atmospheric Sciences*, 56(10):1282–1307.

Ogawa, A. (1984). Estimation of the collection efficiencies of the three types of the cyclone dust collectors from the standpoint of the flow pattern in the cylindrical cyclone dust collectors. *Bulletin of the JSME*, 27(223):64–69.

Rankine, W. J. M. (1858). *A Manual of Applied Mechanics*. C. Griffin and Co., London, UK, 9th edition.

Rayleigh, L. (1916). On the flow of a compressible fluid past an obstacle. *Philosophical Magazine*, 32:1.

Reydon, R. F. and Gauvin, W. H. (1981). Theoretical and experimental studies of confined vortex flow. *The Canadian Journal of Chemical Engineering*, 59:14–23.

Rice, E. E., Chiaverini, M. J., J., M. M., St. Clair, C. P., Knuth, W. H., Gustafson, R. J., and Gramer, D. J. (2001). Status report on Mars ISRU CO/O2 hybrid engine development and testing. Technical Report CP-2001-210826, NASA.

Rietema, K. (1961). Performance and design of hydrocyclones-I General considerations. *Chemical Engineering Science*, 15:298–302.

Rom, C. J. (2006). Flow field and near nozzle fuel spray characterization for a cold flowing vortex engine. Master's thesis, University of Wisconsin-Madison.

Rott, N. (1958). On the viscous core of a line vortex. *Zeitschrift für Angewandte Mathematik und Physik*, 9:543–553.

Rusak, Z. and Lee, J. H. (2004). On the stability of a compressible axisymmetric rotating flow in a pipe. *Journal of Fluid Mechanics*, 501:25–42.

Rusak, Z., Wang, S., and Whiting, C. H. (1998). The evolution of a perturbed vortex in a pipe to axisymmetric vortex breakdown. *Journal of Fluid Mechanics*, 366(1):211–237.

Saad, T., Maicke, B. A., and Majdalani, J. (2011). Coordinate indepenedent forms of the compressible potential flow equations. In *47th AIAA Joint Propulsion Conference*, San Diego, CA. AIAA Paper 2011-5862.

Saad, T. and Majdalani, J. (2010). On the Lagrangian optimization of wall-injected flows: From the Hart-McClure potential to the Taylor-Culick rotational motion. *Proceedings of the Royal Society of London, Series A*, 466(2114):331–362.

Shapiro, A. H. (1953). *The Dynamics and Thermodynamics of Compressible Fluid Flow*, volume 1. The Ronald Press Company.

Smith, J. L. (1962a). An analysis of the vortex flow in the cyclone separator. *Journal of Basic Engineering*, 84(4):609–618.

Smith, J. L. (1962b). An experimental study of the vortex in the cyclone separator. *Journal of Basic Engineering*, 84(4):602–608.

Sousa, J. M. M. (2008). Steady vortex breakdown in swirling flow inside a closed container: Numerical simulations, PIV and LDV measurements. *Open Mechanical Engineering Journal*, 2:69–74.

Sullivan, R. D. (1959). A two-cell vortex solution to the Navier-Stokes equations. *Journal of the Aerospace Sciences*, 26(11):767–768.

Taylor, G. I. (1910). The conditions necessary for discontinuous motion in gases. *Proceedings of the Royal Society of London, Series A*, 84:371–377.

ter Linden, A. J. (1949). Investigations into cyclone dust collectors. *Proceedings of the Institution of Mechanical Engineers*, 160:233–251.

Trapp, R. J. (2000). A clarification of vortex breakdown and tornadogenesis. *Monthly Weather Review*, 128:888–895.

Tsien, H.-S. (1939). Two-dimensional subsonic flow of compressible fluids. *Journal of the Aeronautical Sciences*, 6(10):399–407.

Vatistas, G. H. (2006). Simple model for turbulent tip vortices. *Journal of Aircraft*, 43(5):1577–1578.

Vatistas, G. H. (2009). Vortices in Homer's odyssey - A scientific approach. In Paipetis, S. A., editor, *Science and Technology in Homeric Epics*, volume 6 of *History of Mechanism and Machine Science*, pages 67–75. Springer Netherlands.

Vatistas, G. H. and Aboelkassem, Y. (2006). Extension of the incompressible $n = 2$ vortex into compressible. *AIAA Journal*, 44(8):1912–1915.

Vatistas, G. H., Lin, S., and Kwok, C. K. (1986). Theoretical and experimental studies on vortex chamber flows. *AIAA Journal*, 24(4):635–642.

von Kármán, T. (1941). Compressiblity effects in aerodynamics. *Journal of the Aeronautical Sciences*, 8(9):337–356.

von Mises, R. (1950). On the thickness of a steady shock wave. *Journal of the Aeronautical Sciences*, 17:551–555.

Vyas, A. B. and Majdalani, J. (2006). Exact solution of the bidirectional vortex. *AIAA Journal*, 44(10):2208–2216.

Wendt, B. J. (2001). Initial circulation and peak vorticity behavior of vortices shed from airfoil vortex generators. Technical Report NASA/CR-2001-211144, NASA.

Wu, J. Z. (1986). Conical turbulent swirling vortex with variable eddy viscosity. *Proceedings of the Royal Society of London, Series A*, 403(1825):235–268.

Wu, M.-h., Wang, Y., Yang, V., and Yetter, R. A. (2007). Combustion in meso-scale vortex combustors. *Proceedings of the Combustion Institute*, 31(2):3235–3242.

Yan, L., Vatistas, G. H., and Lin, S. (2000). Experimental studies on turbulence kinetic energy in confined vortex flows. *Journal of Thermal Science*, 9(1):10–22.

Zhang, Z. and Hugo, R. J. (2006). Stereo particle image velocimetry applied to a vortex pipe flow. *Experiments in Fluids*, 40:333–346.

Appendix

Appendix A

Summary of Equations

A.1 Integral Definitions

The integrals in Table A.1 appear in Section 5.1.3 during the solution of the compressible correction to the Bragg-Hawthorne formulation of the bidirectional vortex.

Table A.1: Operational parameters for the PIV experiments.

I	Definition
$\mathcal{I}_1(r)$	$\int_1^r J_1(\lambda_0 r_1) Y_1(\lambda_0 r_1) \{-\lambda_0 r_1 [J_0^2(\lambda_0 r_1) + J_1^2(\lambda_0 r_1)] - J_0(\lambda_0 r_1) J_1(\lambda_0 r_1)\} \mathrm{d}r_1$
$\mathcal{I}_2(r)$	$\int_1^r r_1^3 J_1^3(\lambda_0 r_1) Y_1(\lambda_0 r_1) \mathrm{d}r_1$
$\mathcal{I}_3(r)$	$\int_1^r J_1^2(\lambda_0 r_2) \{J_0(\lambda_0 r_2) J_1(\lambda_0 r_2) + \lambda_0 r_2 [J_0^2(\lambda_0 r_2) + J_1^2(\lambda_0 r_2)]\} \mathrm{d}r_2$
$\mathcal{I}_4(r)$	$\int_1^r -r_2^3 J_1^4(\lambda_0 r_2) \mathrm{d}r_2$
$\mathcal{I}_5(r)$	$\int_1^r J_1(\lambda_0 r_1) Y_1(\lambda_0 r_1) \{2\lambda_0 r_1 J_0^2(\lambda_0 r_1) - J_0(\lambda_0 r_1) J_1(\lambda_0 r_1)\} \mathrm{d}r_1$
$\mathcal{I}_6(r)$	$\int_1^r r_1 J_1(\lambda_0 r_1) Y_1(\lambda_0 r_1) \mathrm{d}r_1$
$\mathcal{I}_7(r)$	$\int_1^r Y_1(\lambda_0 r_1) R_b(r_1) \mathrm{d}r_1$
$\mathcal{I}_8(r)$	$\int_1^r J_1^2(\lambda_0 r_2) \{J_0(\lambda_0 r_2) J_1(\lambda_0 r_2) - 2\lambda_0 r_2 J_0^2(\lambda_0 r_2)\} \mathrm{d}r_2$
$\mathcal{I}_9(r)$	$\int_1^r -r_2 J_1^2(\lambda_0 r_2) \mathrm{d}r_2$
$\mathcal{I}_{10}(r)$	$\int_1^r J_1(\lambda_0 r_2) R_b(r_2) \mathrm{d}r_2$

A.2 Summary of Derived Equations

A.2.1 Dimensional Governing Equations

Conservation of Mass: Original Citation (3.10)

$$\bar{\nabla} \cdot \left(\bar{\rho}\bar{\boldsymbol{U}}\right) = 0 \tag{A.1}$$

Conservation of Energy: Original Citation (3.13)

$$\nabla \cdot \left(\bar{\rho}\bar{H}\bar{\boldsymbol{U}}\right) = 0 \tag{A.2}$$

Conservation of Momentum: Original Citation (3.14)

$$\bar{\boldsymbol{U}} \cdot \nabla \bar{\boldsymbol{U}} = -\frac{\nabla \bar{p}}{\bar{\rho}} \tag{A.3}$$

Stagnation Enthalpy: Original Citation (3.18)

$$\bar{H} = \frac{1}{2}(\bar{\boldsymbol{U}} \cdot \bar{\boldsymbol{U}}) + \frac{\gamma}{\gamma - 1}\frac{\bar{p}}{\bar{\rho}} \tag{A.4}$$

A.2.2 Normalization Equations

Spatial Normalization: Original Citation (3.7)

$$z = \frac{\bar{z}}{a};\ r = \frac{\bar{r}}{a};\ \nabla = a\bar{\nabla};\ \beta = \frac{b}{a} \tag{A.5}$$

Velocity Normalization: Original Citation (3.8)

$$u = \frac{\bar{u}}{U};\ v = \frac{\bar{v}}{U};\ w = \frac{\bar{w}}{U};\ \boldsymbol{\Omega} = \frac{a\bar{\boldsymbol{\Omega}}}{U};\ \psi = \frac{\bar{\psi}}{\rho_0 U a^2};\ H = \frac{\bar{H}}{U^2} \tag{A.6}$$

Thermodynamic Normalization: Original Citation (3.9)

$$p = \frac{\bar{p}}{p_0};\ \rho = \frac{\bar{\rho}}{\rho_0};\ Q = \frac{\bar{Q}}{Ua^2} = \frac{A_i}{a^2};\ \dot{m} = \frac{\bar{\dot{m}}}{\rho_0 U a^2} \tag{A.7}$$

A.2.3 Normalized Governing Equations

Conservation of Mass: Original Citation (3.12)

$$\nabla \cdot (\rho \boldsymbol{U}) = 0 \tag{A.8}$$

Conservation of Energy: Original Citation (3.40)

$$\nabla \cdot (\rho H \boldsymbol{U}) = 0 \tag{A.9}$$

Conservation of Momentum: Original Citation (3.17)

$$\boldsymbol{U} \cdot \nabla \boldsymbol{U} = -\frac{\nabla p}{\gamma M^2 \rho} \tag{A.10}$$

Stagnation Enthalpy: Original Citation (3.39)

$$H = \frac{1}{2}(\boldsymbol{u} \cdot \boldsymbol{u}) + \frac{1}{M^2(\gamma - 1)}\frac{p}{\rho} \tag{A.11}$$

A.2.4 Vorticity-Stream Function General Form

Stream Function Equation: Original Citation (3.32)

$$\rho D^2 \psi + r\rho^2 \Omega_\theta = \nabla \rho \cdot \nabla \psi \tag{A.12}$$

Vorticity Transport Equation: Original Citation (3.34)

$$\nabla \times (\boldsymbol{U} \times \boldsymbol{\Omega}) = \frac{1}{\gamma M^2 \rho^2} \nabla \rho \cdot \nabla p \tag{A.13}$$

Radial Momentum Equation: Original Citation (3.35)

$$u\frac{\partial u}{\partial r} - \frac{v^2}{r} + w\frac{\partial u}{\partial z} = -\frac{1}{\gamma M^2 \rho}\frac{\partial p}{\partial r} \tag{A.14}$$

Axial Momentum Equation: Original Citation (3.36)

$$w\frac{\partial w}{\partial z} + u\frac{\partial w}{\partial r} = -\frac{1}{\gamma M^2 \rho}\frac{\partial p}{\partial z} \tag{A.15}$$

Isentropic Equations: Original Citations (3.37) and (3.38)

$$\rho = p^{1/\gamma} \tag{A.16}$$

$$T = p^{1-1/\gamma} \tag{A.17}$$

A.2.5 Bragg-Hawthorne General Form

Stream Function Equation: Original Citation (3.64)

$$D^2\psi + \rho^2 \left(\Gamma \frac{\partial \Gamma}{\partial \psi} - r^2 \frac{\partial H}{\partial \psi} \right) = \frac{1}{\rho} \nabla \rho \cdot \nabla \psi \tag{A.18}$$

Density Equation: Original Citation (3.66)

$$H - \frac{\Gamma^2}{r^2} = \frac{1}{2\rho^2 r^2} \left[\left(\frac{\partial \psi}{\partial z} \right)^2 + \left(\frac{\partial \psi}{\partial r} \right)^2 \right] + \frac{1}{M^2 (\gamma - 1)} \rho^{\gamma - 1} \tag{A.19}$$

A.2.6 Perturbed Vorticity-Stream Equations

Leading-Order Stream Function Equation: Original Citation (4.40)

$$\mathrm{D}^2 \psi_0 + r\Omega_0 = 0 \tag{A.20}$$

First-Order Stream Function Equation: Original Citation (4.41)

$$\mathrm{D}^2 \psi_1 + r\Omega_1 = \nabla \rho_1 \cdot \nabla \psi_0 - r\Omega_0 \rho_1 \tag{A.21}$$

Leading-Order Vorticity Transport Equation: Original Citation (4.37)

$$\nabla \times (\boldsymbol{U}_0 \times \boldsymbol{\Omega}_0) = 0 \tag{A.22}$$

First-Order Vorticity Transport Equation: Original Citation (4.38)

$$\nabla \times (\boldsymbol{U}_0 \times \boldsymbol{\Omega}_1) + \nabla \times (\boldsymbol{U}_1 \times \boldsymbol{\Omega}_0) = -\frac{\nabla \rho_1 \times \nabla p_1}{\gamma} \tag{A.23}$$

Leading-Order Radial Momentum Equation: Original Citation (4.43)

$$-\frac{1}{\gamma}\frac{\partial p_1}{\partial r} = u_0 \frac{\partial u_0}{\partial r} + w_0 \frac{\partial u_0}{\partial z} - \frac{v_0^2}{r} \tag{A.24}$$

First-Order Radial Momentum Equation: Original Citation (4.44)

$$-\frac{1}{\gamma}\frac{\partial p_2}{\partial r} = \rho_1 \left(u_0 \frac{\partial u_0}{\partial r} + w_0 \frac{\partial u_0}{\partial z} - \frac{v_0^2}{r} \right) + \frac{\partial (u_0 u_1)}{\partial r} + w_0 \frac{\partial u_1}{\partial z} + w_1 \frac{\partial u_0}{\partial z} \tag{A.25}$$

Leading-Order Axial Momentum Equation: Original Citation (4.45)

$$-\frac{1}{\gamma}\frac{\partial p_1}{\partial z} = w_0 \frac{\partial w_0}{\partial z} + u_0 \frac{\partial w_0}{\partial r} \tag{A.26}$$

First-Order Axial Momentum Equation: Original Citation (4.46)

$$-\frac{1}{\gamma}\frac{\partial p_2}{\partial z} = \rho_1 \left(w_0 \frac{\partial w_0}{\partial z} + u_0 \frac{\partial w_0}{\partial r} \right) + \frac{\partial (w_0 w_1)}{\partial z} + u_0 \frac{\partial w_1}{\partial r} + u_1 \frac{\partial w_0}{\partial r} \tag{A.27}$$

A.2.7 Perturbed Bragg-Hawthorne Equations

Leading-Order Stream Function Equation: Original Citation (4.17)

$$D^2 \psi_0 + B_0 \frac{\mathrm{d}B_0}{\mathrm{d}\psi} - r^2 \frac{\mathrm{d}H_0}{\mathrm{d}\psi} = 0 \tag{A.28}$$

First-Order Stream Function Equation: Original Citation (4.18)

$$\begin{aligned} D^2 \psi_1 + B_1 \frac{\mathrm{d}B_1}{\mathrm{d}\psi} - r^2 \frac{\mathrm{d}H_1}{\mathrm{d}\psi} = \frac{\partial \rho_1}{\partial z}\frac{\partial \psi_0}{\partial z} + \frac{\partial \rho_1}{\partial r}\frac{\partial \psi_0}{\partial r} \\ - \rho_1 \left[D^2 \psi_0 + 3 \left(B_0 \frac{\mathrm{d}B_0}{\mathrm{d}\psi} - r^2 \frac{\mathrm{d}H_0}{\mathrm{d}\psi} \right) \right] \end{aligned} \tag{A.29}$$

Leading-Order Density Equation: Original Citation (4.20)

$$H_0 - \frac{B_0^2}{2r^2} = \frac{1}{2r^2}\left[\left(\frac{\partial\psi_0}{\partial r}\right)^2 + \left(\frac{\partial\psi_0}{\partial z}\right)^2\right] + \frac{\gamma+1}{\gamma-1}\rho_1 \tag{A.30}$$

First-Order Density Equation: Original Citation (4.21)

$$2\rho_1\left(H_0 - \frac{B_0}{2r^2}\right) + H_1 - \frac{B_0 B_1}{2r^2} = \frac{1}{2r^2}\left[\frac{\partial\psi_0}{\partial r}\frac{\partial\psi_1}{\partial r} + \frac{\partial\psi_0}{\partial z}\frac{\partial\psi_1}{\partial z}\right] + \frac{\gamma+1}{\gamma-1}\left(\rho_2 + \gamma\rho_1^2\right) \tag{A.31}$$

Appendix B

Piecewise Least Squares Code

This first function calculates the matching radius using a least squares regression. The quantity in Sum[] is the derivative of the expression of interest. Findroot is used to solve the nonlinear equation and is given a starting value of 0.25 (an approximation of the matching radius). Here l is the data set being compared to the theory and ω is the injection swirl velocity. For normalized cases, this can be set to 1.

```
MatchCalc[l_, ω_] :=
 Module[{i, pos = Length[l]},
  FindRoot[
   Sum[((2 ω l[[i, 1]])/β^3 - ( 2 ω l[[i, 1]]
        (1 - 2 Log[l[[i, 1]]/β]))/β^3)
        ((ω l[[i, 1]] (1 - 2 Log[l[[i, 1]]/β]))/β^2 -
        l[[i, 2]]), {i, pos}] == 0, {β, 0.25}][[1, 2]]]
```

The next function calculates the truncated data set based on a matching radius found from the previous function. Here $n2$ is the newly truncated data set.

```
TruncList[ l_, ω_] :=
 Module[{i, tRad, n2},
  n2 = {};
  tRad = MatchCalc[l, ω];
```

```
For[i = 1, l[[i, 1]] < tRad, i++, AppendTo[n2, l[[i]]]];
n2]
```

Finally, PiecewiseLeastSquares is the function that combines the previous subroutines and contains the iteration and tolerance logic. The final output will be the matching radius for the piecewise function that conforms to the input tolerance. Here tol is the input tolerance used in the convergence calculation and val and val2 are placeholder lists used to hold the truncated data from this step and the previous step.

```
PiecewiseLeastSquares[l_, tol_, ω_] :=
 Module[{val, val2, tList},
  tList = TruncList[l, ω];
  val = MatchCalc[l, ω];
  val2 = MatchCalc[TruncList[l, ω], ω];
  While[val - val2 > tol,
   tList = TruncList[tList, ω]; {val = val2,
    val2 = MatchCalc[tList, ω]}];
  MatchCalc[tList, ω]]
```

Vita

Brian Allen Maicke was born on July 13, 1977 to Robert and Linda Maicke. He completed his undergraduate studies at Marquette University, earning a B.S. in Mechanical Engineering with an emphasis in machine design. After earning his degree, Brian worked at W. A. Whitney as a mechanical engineer and at American NTN Bearing Manufacturing as a manufacturing engineer before resuming his graduate studies at the University of Tennessee Space Institute. While studying under Dr. Joseph Majdalani, Brian earned his M.S in Aerospace Engineering for his thesis on the compressible flow in rocket motors. His doctorate is both a generalization and extension of that work to include swirling flows such as those found in the bidirectional vortex rocket engine.